

Microwave observations and modeling of the molecular coma in comets

Dissertation
zur Erlangung des Doktorgrades
der Mathematisch-Naturwissenschaftlichen Fakultäten
der Georg-August-Universität zu Göttingen

vorgelegt von
Michał Drahus
aus Kraków, Polen

Göttingen 2009

Bibliografische Information der Deutschen Nationalbibliothek

Die Deutsche Nationalbibliothek verzeichnet diese Publikation in der Deutschen Nationalbibliografie; detaillierte bibliografische Daten sind im Internet über <http://dnb.d-nb.de> abrufbar.

D7

Referent: Prof. Dr. Stefan Dreizler

Korreferent: Prof. Dr. Ulrich Christensen

Tag der mündlichen Prüfung: 23. Juni 2009

ISBN 978-3-942171-33-5

uni-edition GmbH 2010

<http://www.uni-edition.de>

© Michał Drahus



This work is distributed under a
Creative Commons Attribution 3.0 License

Printed in Germany

Contents

Summary	5
1 Introduction	7
1.1 Comets	7
1.2 Microwave spectroscopy	10
1.2.1 Antenna and beam	11
1.2.2 Heterodyne receiver	12
1.2.3 Microwave spectrum	14
1.2.4 Observing noise	15
1.3 Basic mathematical formulations	18
1.3.1 Constant isotropic emission	18
1.3.2 Propagation of microwave radiation through the coma	18
1.3.3 Integration within a Gaussian beam	21
1.3.4 Derivation of the line area	21
2 Comet 73P/Schwassmann-Wachmann 3	23
2.1 Introduction	23
2.2 Observations and data reduction	24
2.3 Line position in the night-averaged spectra	28
2.4 Production rate of the HCN molecule	32
2.4.1 Model and parameters	32
2.4.2 Individual production rates	33
2.4.3 Discussion	34
2.5 Rotation period of the nucleus	35
2.5.1 Basic concepts	35
2.5.2 Methods	36
2.5.3 Results	38
2.5.4 Discussion	42
2.6 Summary and conclusions	44
2.7 Supplementary discussion	45
2.7.1 Validation of the model and parameters	45
2.7.2 Validation of the heliocentric correction (contributed by Michael Küppers)	53
2.7.3 Validation of the periodicity analysis	55

3	Comet 17P/Holmes	61
3.1	Introduction	61
3.2	Observations and data reduction	63
3.3	Early evolution of the line shapes	67
3.4	Rotational temperature and expansion velocity	70
3.5	Other molecules	71
3.6	Late monitoring	72
3.7	Discussion	76
3.8	Summary and outlook	79
4	Comet 8P/Tuttle and a new model of the cometary microwave spectra	81
4.1	Introduction	81
4.2	Observations	83
4.3	Analysis	84
4.4	A new model of cometary microwave spectra	86
4.4.1	Coordinate systems	87
4.4.2	Sublimation potential and activation function	88
4.4.3	Distribution of molecules	89
4.4.4	Calculation of a spectral line profile	90
4.4.5	A spectral line profile at an offset position	90
4.5	Application to the spectra of comet Tuttle	91
4.5.1	Implementation and basic results	91
4.5.2	Further approaches	93
4.5.3	Discussion	94
4.6	Summary and conclusions	97
5	Prospects for <i>in-situ</i> observations of 67P/Churyumov-Gerasimenko	99
5.1	Introduction	99
5.2	Simulations	102
5.2.1	Models	102
5.2.2	Observing geometries	103
5.3	Results	103
5.4	Discussion and conclusions	106
6	Outlook	109
	Bibliography	115
	Publications	123
	Acknowledgements	125
	Curriculum Vitae	127

Summary

This thesis consists of the results from observations of comets 73P-C/Schwassmann-Wachmann 3, 17P/Holmes, and 8P/Tuttle, which I observed at millimeter wavelengths between May 2006 and March 2008, using the Submillimeter and the Kitt Peak telescopes of the Arizona Radio Observatory. I also investigated prospects for *in-situ* observations of comet 67P/Churyumov-Gerasimenko with the Microwave Instrument for the Rosetta Orbiter (MIRO).

Observations of the first comet, analyzed with a simple model, revealed that the nucleus rotation period might be unusually short. This tentatively suggests a *rotational break-up* of the parent body, and sets a meaningful upper limit on the bulk tensile strength of the nucleus.

Observations of the second comet provided a detailed portrait of the evolution of molecular environment during its spectacular outburst. I concluded that the gas cloud was anisotropic, and presumably resulted from several competing sources of activity. The explosion itself appears as a sudden, impulsive event, and only 1.5 months later the nucleus was back to (or close to) its expected non-explosive activity.

The last comet exhibited short-term variability of the HCN line profile, which I interpreted as being caused by jets emanating from a rotating nucleus. Therefore, I also developed a new model of molecular line emission in microwaves. The model is the first fully time-dependent anisotropic construction of that kind. Applied to the data of comet Tuttle, it provided the spin axis orientation, and the distribution of activity over the nucleus – the properties, which are normally very difficult to determine from ground.

The simulations of the MIRO observations of comet 67P/Churyumov-Gerasimenko were based on the most advanced models of the comet's coma available to date, and the radiative-transfer code that had been developed in house. They show that water vapor can already be detected at the arrival of *Rosetta*, and that the most favorable observing direction will be nadir, whereas zenith should be avoided. I also demonstrate that the lines will be optically thick, thus the full radiative transfer treatment is the only plausible approach.

Overall, my Ph.D. research provides characterization of three objects, supports the preparation for science with *Rosetta*, and contributes to the methodology of observational astrophysics of comets. It is also a baseline for future studies, an example of which is presented in the outlook.

1 Introduction

Since the dawn of civilization comets have been considered as the messengers announcing forthcoming disasters. Appearing unexpectedly, they have noticeably contrasted with the majesty and harmony of the skies. Although comets have always intrigued their observers, the first light on the secrets of their nature has been shed not before the end of the 16th century. It was Tycho Brahe who first realized cosmic distance to the Great Comet of 1577. The next milestone came a century later with Newton's method of determining parabolic orbits of comets. Consequently, it led Edmond Halley to postulate in 1705 that some trajectories may be closed, and hence the same object may appear periodically. In spite of great efforts (Fig. 1.1), the physical nature of comets has remained unclear until the middle of the 20th century.

For nearly 40 years now, radio astronomy – and especially its microwave domain – have played an important role in the process of learning what comets are, and how they actually work. The beginnings were not easy though: after a decade from the first tentative radio-detection of molecules in a comet¹, in his review Crovisier (1985) concluded: *Several years of effort with only marginal or controversial results show that radio observations of parent molecules in comets are not easy*. Indeed, the breakthrough was still to come with the approach of comet Halley in 1986, and a great triumph a decade later with the appearance of comet Hale-Bopp, which became perhaps the best investigated molecular environment in space.

In the introduction to my thesis I briefly present the basic concepts and terminology used for comets (Section 1.1), followed by the fundamentals of microwave spectroscopy (Section 1.2). In the last part (Section 1.3) I present basic mathematical concepts to describe observational data; they have been used and further developed in the following chapters.

1.1 Comets

Comets are icy remains of the Solar System formation from a protoplanetary disc. They fall into a number of different populations with sources in different parts of the disc. The Jupiter Family Comets come from the Kuiper Belt, and most likely formed in that region, while the Long Period and Halley Type Comets (now collectively known as Nearly Isotropic Comets – see Levison 1996) come from the Oort Cloud, but were formed in the region of the giant planets before being scattered out there (see Duncan et al. 2004, Dones et al. 2004). Finally, the comets recently identified in the Main Asteroid Belt, most

¹C/1973 E1 (Kohoutek)

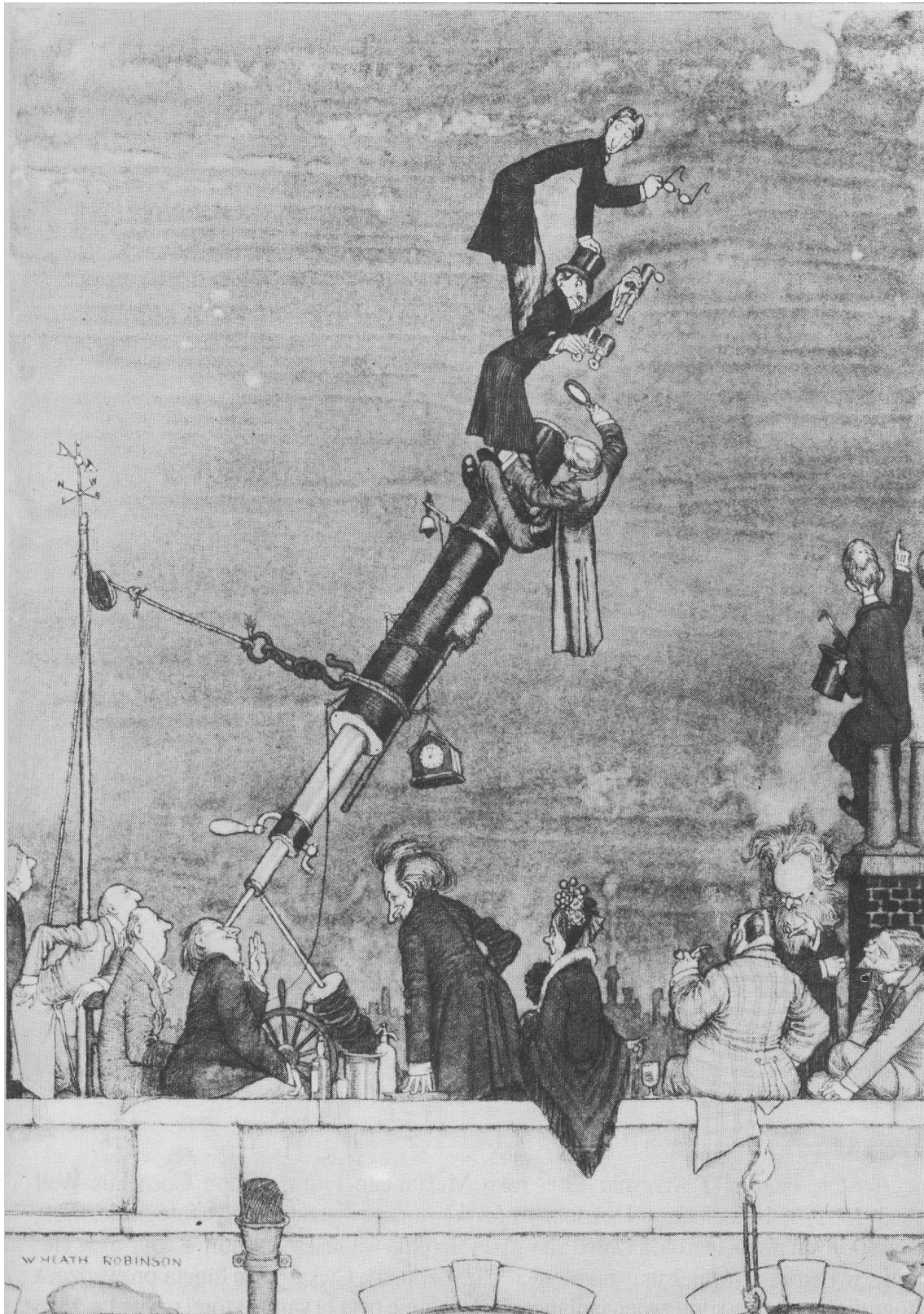


Figure 1.1: British caricature from 1909 by William Heath Robinson. It shows the astronomers from Greenwich Observatory doing neat tricks to better see comet Halley.

probably occupy their original formation region (Hsieh et al. 2006). Therefore comets are not only the “time capsules” containing the material from the protoplanetary nebula, but, in fact, well-preserved probes from various regions of the young Sun’s disc.

Cometary material is stored in a *nucleus*. It consists of a mixture of dust and ice, which is by far dominated by the water ice. The internal structure is presumably undifferentiated except for the outer-most layer, with large porosity and low tensile strength of the bulk material. The mean density of the nucleus is roughly half of that of water, and a typical size is of a few kilometers across.

While approaching the Sun the cometary ices start *sublimating*. The escaping gas naturally drags dust with it (originally frozen in the ice), and also carries icy grains which sublimate later on. This gives birth to the cometary atmosphere – the *coma*. Unlike a typical planetary atmosphere, the coma is not tied gravitationally to the nucleus: it is continually being produced and lost to space. Therefore its density evolves incessantly, reflecting an instantaneous activity of its source. To give the process some scale, note that at 1 AU from the Sun the gas moves away from the nucleus with a velocity of typically about 1 km s^{-1} , and this value is anticorrelated with the heliocentric distance. The main sublimating component is water ice, but only at the distance below about 3 AU. In spite of its dominant position as the nucleus’ constituent, at larger heliocentric distances the sublimation may be dominated by carbon monoxide. That is because CO sublimates efficiently also at very low temperatures, at which H_2O is only in a solid state. Whether the sublimation of CO can dominate that of H_2O depends, however, also on the abundance of this component. For example, some comets suffer from a severe depletion in CO, which is presumably of a cosmogonic origin.

Whereas the mixture which sublimates from the nucleus consists of neutral molecules, some of them being actually very complex, the cometary coma contains additionally a great inventory of simple radicals, atoms, and ions. These are created under the influence of the solar UV radiation and solar wind: the molecules which escaped from the nucleus into the coma (the so-called *parent molecules*) are being progressively fragmented into simpler elements (*daughter species*). Eventually, this gives the coma a hierarchic (multi-generational) compositional radial structure (see examples of some photochemical reactions in Fig 1.2). The process which dominates destruction of the molecules is *photodissociation*; its efficiency is normally much higher than the efficiencies of photoionization, and dissociation and ionization by the elements in the solar wind (mostly protons and electrons).

Characteristic lifetimes of the daughter generations are normally much longer than of their immediate parents. At 1 AU from the Sun we have for example: 27 h for H_2O vs. 49 h for OH. The lifetimes are proportional to the square of heliocentric distance; they also depend on the level of solar activity, and even on the relative velocity between the comet and the Sun – though the importance of the last two is very intrinsic to each element (in a collective sense), and is often relatively small.

At the far end of the photochemical tree we find ions: both atomic and molecular (e.g. the especially abundant H_2O^+ and CO^+). Each molecule – once ionized – is immediately accelerated into the *ion tail*. More precisely, formation of the tail is caused by the solar-wind magnetic field lines which are draped around the comet’s *ionosphere*. Worth noting is that due to this particular relation the cometary ion tails have been often used as the diagnostic tools for studying the conditions in solar-wind plasma.

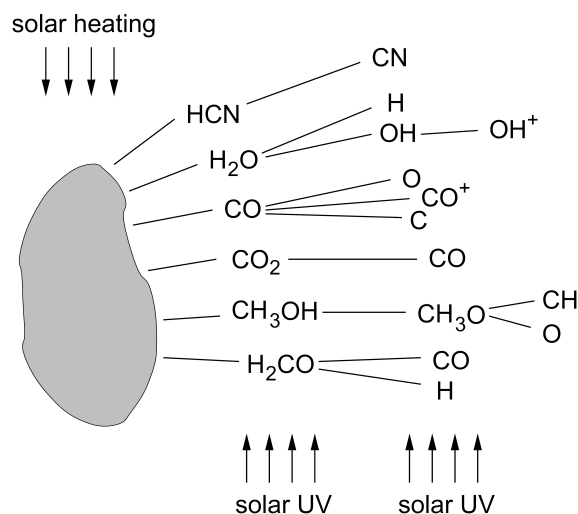


Figure 1.2: Examples of photochemical reactions which destroy the parent elements and simultaneously give birth to their daughters (prepared by Christopher Jarchow).

And what happens to the dust? In the inner-most coma its motion is controlled by the gas which drags it away from the nucleus. The velocities of dust grains are strongly anticorrelated with size, and are generally a factor of few lower comparing to the gas. Once decoupled from the latter, their trajectories become controlled by the balance between the attractive solar gravitation and the repulsive pressure of the solar radiation (both inversely proportional to the square of heliocentric distance). It has been established that the two forces are equal for the particles of roughly $1\text{-}\mu\text{m}$ diameter, and the repulsion-to-attraction ratio is inversely proportional to size; it also depends on particle's shape and density. Consequently, the sub-micron grains move generally away from the Sun, which eventually gives birth to a *dust tail*. The size distribution of dust spans over several orders of magnitude; it is well-approximated by a power law, and the exponent is typically between -3 and -4 .

1.2 Microwave spectroscopy

As the *microwaves* let us consider here the electromagnetic waves from the frequency range ν between 60 and 1000 GHz, or equivalently, from the wavelength range λ between 5 and 0.3 mm. Microwaves are hence comprised of the *millimeter* and *submillimeter* spectral regimes, and are located in the high-end of the *radio* frequencies. Except for their lowest frequencies, microwaves are commonly considered as lost for ground-based science due to atmospheric opacity. Though this is generally true at the sea level, selected high-altitude sites offer occasionally as much as 80–90% atmospheric transmission at about 300 GHz ($\lambda = 1\text{ mm}$). Examples of the model predictions for the high-end of the microwave frequencies are presented in Fig. 1.3.

Microwaves are the natural spectral region for observing the rotational transitions in molecules. Using the state-of-the-art receiver technologies, they can be detected with good sensitivity, and analyzed spectroscopically with an unprecedented resolution. Indeed, yielding often $\nu/\Delta\nu > 1$ million ($\Delta\nu_r < 0.3\text{ km s}^{-1}$), microwave spectroscopy pro-

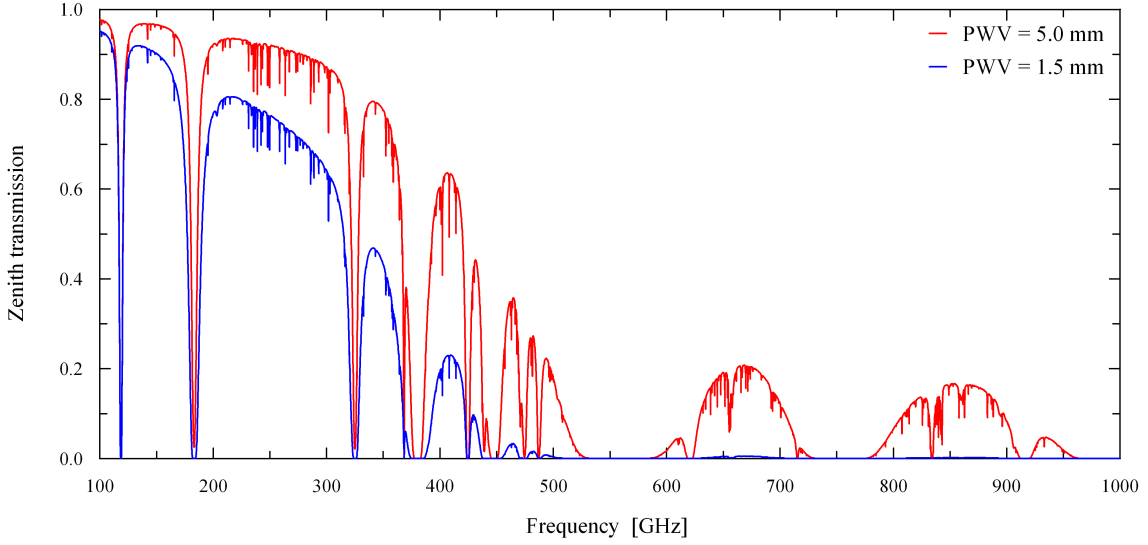


Figure 1.3: Theoretical zenith atmospheric transmission as a function of frequency for two different values of precipitable water vapor. Calculated with the ATM model by Juan Pardo available online at the APEX website. PWV of 5 mm (*red* line) corresponds to the typical conditions while observing comet 73P/Schwassmann-Wachmann 3 (Chapter 2), whereas PWV of 1.5 mm (*blue* line) to our observations of comet Tuttle (Chapter 4); while observing comet Holmes (Chapter 3) we encountered a variety of conditions.

vides velocity-resolved spectra for various molecular environments, including cometary comae. The extreme resolving power is hence the key feature which decides about its great potential, and which has opened new and exciting horizons in the research on comets.

1.2.1 Antenna and beam

Though microwave interferometers and recently also receiver arrays have opened possibilities for imaging at these wavelengths, single-pixel observing still remains the primary technique, and, as such, was used for all the research presented in this thesis. This “single pixel” is called the telescope’s *beam*. Its sensitivity profile is defined by the diffraction pattern of the *antenna*. It has a pronounced *main lobe* at the center, and associated *side lobes* whose sensitivity is generally very low and quickly decreases away from the beam’s center.

However, for several practical reasons, the beam is considered as a symmetric Gaussian, whose sensitivity profile $G(\rho, \phi)$ is given by:

$$G(\rho, \phi) = e^{-\frac{\rho^2}{\sigma^2}}, \quad (1.1)$$

where ρ and ϕ are the radial and azimuthal coordinates within the beam, and σ indicates the beam width. It is readily visible that the peak sensitivity is $G(0, \phi) = 1$, and that $\sigma = \sigma_{\frac{1}{2}} / \sqrt{\ln 2}$, where $\sigma_{\frac{1}{2}}$ is the beam radius at half-sensitivity. This radius can be estimated from the width of the antenna’s diffraction pattern:

$$\text{FWHM} = b \frac{\lambda}{D} = b \frac{c}{\nu D}, \quad (1.2)$$

which gives the width in radians, and where $c = 2.99792458 \times 10^8 \text{ m s}^{-1}$ is the speed of light, λ is the observed wavelength and ν frequency, D is the dish diameter, and b is a dimensionless factor which is intrinsic to every antenna (see next paragraph). Using now the above equation, and taking into account that it is convenient to consider $\sigma_{\frac{1}{2}}$ and ρ as real distances in the *observing plane*, that is, in a plane which crosses the observed object and is normal to the line of sight, we can write:

$$\sigma_{\frac{1}{2}} = \frac{1}{2} \Delta b \frac{c}{\nu D}, \quad (1.3)$$

where Δ is the comet–observer distance.

Since the Gaussian profile is introduced as an approximation of the main lobe, we call it the *main beam*. This suggests that b should be close to 0.89, which is a theoretical value that provides with Eq. (1.2) the FWHM of the main lobe in a perfect Airy profile. (This is not to be mistaken with $b = 1.22$, which yields – with the same formula – a distance to the first minimum.) In fact b is usually a bit larger, typically about 1.2, because of two reasons: (i) an approximation of the Airy pattern with the Gaussian profile is optimal when the FWHM of the latter is equal to the output of Eq. (1.2) with $b = 0.99$ (assuming that their peaks are equal); (ii) *edge tapering*, which suppresses the side-lobes, causes also broadening of the beam. Transformation of the observed signal into a signal which would be observed in the main beam is done conveniently through a single empirical scaling factor which is called the *main-beam efficiency* η_{mB} . Once transformed, the observations can be then analyzed in the framework of the main-beam concept.

1.2.2 Heterodyne receiver

Microwave spectroscopy utilize a *heterodyne receiver*. The receiver is the intermediate component between the *antenna* and *spectrometers*, which takes the output of the former and provides the input for the latter. Whereas the antenna collects signals with almost all frequencies, the receiver selects the wanted range and converts it to much lower frequencies. The signal is also amplified (after and/or before the conversion). This down-conversion is the principle characteristic of heterodyne receivers, which lets the original, high-frequency signals to be handled with standard low-frequency electronics, developed for traditional radio astronomy for decades.

The downconversion is realized by the mixer, which combines the original collection of signals with a signal from the *local oscillator* having a constant frequency ν_{LO} . As a result, a frequency ν is found at $\nu_{\text{new}} = |\nu - \nu_{\text{LO}}|$ (see e.g. Jarchow 1998, for a mathematical proof and graphical illustration). It is readily visible, that two frequencies: $\nu = \nu_{\text{LO}} - \nu_{\text{new}}$ and $\nu = \nu_{\text{LO}} + \nu_{\text{new}}$ are downconverted to the same new frequency ν_{new} . Consequently, two frequency ranges, located symmetrically around ν_{LO} (so called *sidebands*), are converted into one range at lower frequencies; obviously, the sidebands have equal *bandwidths*, and the downconverted bandwidth is also the same. Heterodyne receivers are therefore naturally *double-sideband*, where one is called *signal-* and the other *image-* sideband. Although somewhat confusing, the original frequency ν is called in literature as *radio frequency* or *RF*, and the downconverted frequency as *intermediate frequency* or *IF*.

Example. A double-sideband receiver provides IF = 4–8 GHz. This means, that the bandwidth is 4 GHz. However, tuning LO to e.g. 250 GHz will provide us with the

frequency ranges 242–246 GHz and 254–258 GHz, all in one spectrum (if only the spectrometer covers the entire IF). Therefore, a double-sideband receiver covers twice the IF bandwidth. On the other hand, confusion is introduced, as one cannot a-priori identify a spectral line through its observed frequency (i.e. it is impossible to say if it belongs to the signal- or image-bandwidth). In extreme situations, two different lines – each visible in a different sideband – may be observed as one.

Although in practice these effects rarely cause problems, technological progress made it possible to suppress one of the sidebands, giving birth to *single-sideband* receivers. Another milestone in mixer technology resulted in *sideband-separating* receivers, which combine the pros and eliminate cons of the single- and double-sideband predecessors, offering full bandwidth with no confusion.

The heterodyne nature of microwave receivers is directly responsible for their incredible spectral resolution. In our example, an input for the spectrometer is provided in the range 4–8 GHz; this range falls in the window of classical radio astronomy, and can be analyzed with its classical tools. Consider a digital autocorrelator with the resolution of 24 kHz. The middle frequency of 6 GHz is analyzed with the resolution $\nu/\Delta\nu = 250\,000$, which is high, yet still typical for radio, and reachable in IR and optical wavelengths. However, this middle frequency corresponds, in fact, to the sky frequencies of 244 and 256 GHz, so the true resolution is a factor of about 40 greater, i.e. it reaches ten million!

Heterodyne receivers naturally act as polarizers – they pick only the waves oscillating in a specific direction (i.e. with a specific linear or circular polarization). Since the radiation from rotational transitions in comets – the subject of study in this thesis – oscillates (and propagates) in all directions, heterodyne receivers record only half of the arriving radiation. Note, however, that every wave can be represented as a sum of two orthogonal oscillations with the same frequency and an arbitrary absolute orientation. Consequently, two receivers, sensitive to orthogonal polarizations, collect the total radiation. This simple fact has been used to construct *dual polarization* receivers, where each of the two *polarization channels* is in fact a separate receiver, though they are mounted in a single dewar and may share some electronics. Since the two polarization channels measure independent signals – which are equal for non-polarized radiation, though feature independent noise realizations – they can be averaged, providing a spectrum with reduced noise. Assuming that both channels perform with the same noise, the average spectrum has a factor of $\sqrt{2}$ reduced noise, which is the theoretical limit. This is normally satisfied only approximately, due to technical limitations. If, for example, one channel performs with noise a factor of $\sqrt{3}$ greater than the other, the average spectrum will feature the same noise level as the individual spectrum from the better channel; if the discrepancy is even larger, one should reject the “bad” channel, and use only the spectra from the “good” one. Moreover, the two channels are always slightly misaligned (i.e. they look at slightly different positions in the sky), and therefore they provide slightly different spectra of typical, non-uniform astronomical sources. For this reason, even if they performed with identical noise, they would likely measure different signal levels. Nevertheless, the typical misalignment considered as small is of about $2''$, and the corresponding difference in spectra, although depending on the beam size and source structure, is usually small or negligible compared to realistic observing noise.

1.2.3 Microwave spectrum

Likewise any other astronomical technique, also microwave spectroscopy has developed its own system of time-honored scales, units, and conventions. Let us hence recall the two of them, which define the axes in a microwave spectrum.

The wavelength λ is rarely used. Instead, the frequency ν is used routinely whenever an absolute scale is needed, that is, for example, to define instrumental properties, or to identify spectral lines. In addition, a relative scale of radial velocities v_r is used whenever a spectrum is to be interpreted in terms of gas kinematics. It is related to the frequency scale through the classical (i.e. non-relativistic) *Doppler law*:

$$v_r = c \left(1 - \frac{\nu_0}{\nu} \right), \quad (1.4)$$

where ν_0 is the transition frequency of the observed line. It is visible that $v_r = 0$ corresponds to $\nu = \nu_0$, and that the positive velocities are redshifted and negative blueshifted with respect to this frequency. Moreover, the velocity resolution Δv_r is given by:

$$\Delta v_r = c \frac{\Delta \nu}{\nu}. \quad (1.5)$$

Since the gas kinematics has been incessantly of interest in my Ph.D. research, this scale has defined the horizontal axis in the spectra throughout this thesis. Moreover, the Doppler shift due to the relative radial motion between the comet and the telescope has been consequently removed, hence v_r is the line-of-sight component of the physical velocity of gas measured with respect to the nucleus. For example, the molecules moving normally to the line of sight emit at $v_r = 0$, those approaching the observer along the line of sight at $v_r = -v_{\text{gas}}$, and those moving away along the line of sight at $v_r = v_{\text{gas}}$, where v_{gas} is the gas flow velocity relative to the nucleus.

Spectral intensity I_ν is traditionally replaced with the *brightness-temperature* T_B , where the *Rayleigh-Jeans approximation* is used for the conversion:

$$T_B(\nu) = \frac{c^2}{2k\nu^2} I_\nu, \quad (1.6)$$

where $k = 1.3806503 \times 10^{-23} \text{ J K}^{-1}$ is the Boltzmann constant. Brightness temperature features several interesting properties: (i) it is linearly related with the intensity, and – as long as the emission is optically thick and the Rayleigh-Jeans approximation holds² – (ii) it is independent of frequency ν , and (iii) is equal to the physical temperature of gas T .

What defines the vertical scale in the spectra is, however, the *main-beam brightness temperature* T_{mB} , which results from an integration of T_B over the main beam followed by an appropriate normalization:

$$T_{\text{mB}} = \frac{\int_0^{2\pi} \int_0^\infty T_B(\rho, \phi) G(\rho, \phi) \rho \, d\rho \, d\phi}{\int_0^{2\pi} \int_0^\infty G(\rho, \phi) \rho \, d\rho \, d\phi}. \quad (1.7)$$

It can be readily seen that T_{mB} is a measure of average brightness within the beam.

²That is when $h\nu \ll kT$.

1.2.4 Observing noise

Observing noise σ_T is given by the *radiometer formula*:

$$\sigma_T = \frac{T_{\text{sys}}}{\sqrt{t} \Delta\nu}, \quad (1.8)$$

where t is the integration time, and T_{sys} is the system temperature. Note, that T_{sys} defines the unit of σ_T , hence must be provided in the main-beam brightness temperature scale if one calculates the noise in a fully-calibrated spectrum. The above formula assumes a negligible noise contribution from the spectrometer; in practice, it is not always the case (cf. Chapter 2.2). Moreover, while some steps in the calibration process only scale the spectrum (preserving the S/N), some other actually add noise – which needs to be taken into account in the above formula. The complete calibration scheme aims at separating the signal from the observed source from the signals generated in the atmosphere, receiver, telescope itself, and coming from the cosmic background, and correcting it for the atmospheric attenuation. The routine has been described in depth by many authors (see e.g. Ulich & Haas 1976, Kutner & Ulich 1981, Wild 1999).

Important part of the calibration process is derivation of a factor which transforms the measured voltage into the temperature scale. This involves observation of the sky and artificial sources placed right in front of the receiver (*hot* and *cold loads*), and results in a single number with an error, which however does not increase the spectral noise (hence does not affect the real sensitivity), but only scales the spectra (hence affects the sensitivity inferred from the observations). Derivation of this factor, and application to the spectra, is normally done automatically. The observer only decides how often it should be re-measured, or even this is hardcoded in the telescope's control system.

Another important operation is switching between the observed source (*ON* position) and sky background (*OFF* position); a resulting spectrum is a difference between the two. Consequently, if half of the time t is spent at ON and half at OFF positions, the noise resulting from Eq. (1.8) needs to be multiplied by $x_1 = \sqrt{2}$; moreover, since the resulting spectrum is a difference between the two, the noise is increased by the additional factor of $x_2 = \sqrt{2}$, thus it is effectively twice as large. In practice, it is another factor of $x_3 \approx \sqrt{2}$ larger, as the *duty cycle* is typically 50%, i.e. only about half of the time is spent for actual ON or OFF integrations, whereas the rest is lost for switching and calibrations. The actual overhead for switching depends on a switching mode and angular separation. *Position switching* is the simplest implementation, where the whole antenna moves between ON and OFF; although quite slow, it has no limit for the maximum offset, which is essential for very extended sources. *Beam switching* combines infrequent (and slow) switches of the antenna position with very frequent (and fast) switches of the sub-reflector position. The antenna is pointed half-way between ON and OFF, and the actual switch is performed by the sub-reflector; however, this mode utilizes in fact two OFF positions, located symmetrically with respect to the source, and therefore also the antenna switches between the two pointings. The maximum offset is equal to the maximum *sub-reflector throw*, which is typically limited to a few arcminutes. This is the preferred observing mode, provided the source is small compared to the sub-reflector throw. To minimize the influence of different atmospheric conditions at the ON and OFF positions, the offset is normally defined in azimuth, securing comparable *airmasses*. However, absolute coordinates (e.g. RA, Dec) of the OFF position are sometimes used when observing fragments

of large molecular complexes, where the reference position needs to be carefully selected, and kept the same over the observing period.

A different philosophy is used in *frequency switching*, where the target source is observed at two slightly different³ tunings. The resulting spectrum is again a difference between the two, but of course, the whole idea works only when we consider signals corresponding to the same spectral channels (not frequencies!). Therefore, care must be taken to ensure that the same channels are not occupied by different lines in the two tunings. Experience shows, that this mode gives worse results compared to the other two, but it features some very interesting properties. First of all, the target source is observed continuously – only the line is placed in different parts of the spectral bin array. Since the resulting spectrum is a difference between the two, the observed line is visible in two “copies”: one in emission and one in absorption. Consequently, the number of bins containing signal from the line is twice as large as in the previous two modes, which makes the effective observing noise a factor of $\sqrt{2}$ lower; in other words, the original noise formula in Eq. (1.8) is not multiplied by $x_1 = \sqrt{2}$, though it still is by $x_2 = \sqrt{2}$. (Note, that the actual reduction of noise is easy to achieve explicitly, if needed: cut the resulting spectrum between the two lines, flip vertically the “absorption piece”, then realign both pieces at the actual line frequency, and finally average them.) The overhead for switching is also lower compared to the beam- and especially position-switching mode, which makes the overall duty cycle higher ($x_3 < \sqrt{2}$) and thus noise even lower. However, the main problem of this mode are poor baselines, which normally surpasses the excellent noise characteristic. Nevertheless, it is the only option for observing extremely large sources (OFF position too far), or when high mechanical robustness is needed (switching is realized by electronics, hence no moving parts). All these properties made it the only mode implemented in MIRO – the instrument that will observe comet 67P/Churyumov-Gerasimenko from inside its own coma (see Chapter 5.1).

The key decisions to be made when observing in any of these modes are: how often to switch and how far to go? The faster we switch – the closer the observing conditions are in the two spectra; but at the same time – the less signal we collect in a single integration, and the more time we loose for switching. The further we go – the smaller the contribution of the source to the reference spectrum; but simultaneously – the larger the difference in the observing conditions, and again, the more time we lose for switching. An example calculation of the source contribution at the offset pointing (relevant for the position- and beam-switching modes) is presented in Fig. 2.3 (Chapter 2). It shows, that if the offset is much smaller than the characteristic photodissociation scalelength, the signal loss at the offset position depends only on the size ratio of the offset to beam, i.e. is independent of their individual values for a given ratio. Furthermore, for offsets much larger than the beam, the measured signal becomes inversely proportional to the offset (or equivalently – directly proportional to the beam size). That is because the coma becomes uniform within the beam, and therefore we reconstruct the model coma profile (further introduced in Section 1.3.1); in other words, we sample the coma with an infinitely small beam – so called *pencil beam*. If the offset is comparable to the photodissociation scalelength, the signal falls down with the offset much faster. That is because at large distances from the nucleus r , volume density ϱ_v is controlled by the photodissociative destruction of the

³Their difference must be greater than the full line-width at the baseline level.

molecules ($\rho_v \propto e^{-r}$) rather than by the free expansion ($\rho_v \propto r^{-2}$), the latter dominating at smaller r . Consequently, the dependence presented in Fig. 2.3 should be considered as the upper limit, especially when considering offsets comparable to (or greater than) the photodissociation scalelength.

In order to use the radiometer formula from Eq. (1.8), we still need to define the system temperature T_{sys} . In the main-beam brightness temperature scale it is given by the equation (e.g. Jewell & Mangum 1999, Pety 2009):

$$T_{\text{sys}} = \frac{(1 + G_{\text{im}}) e^{-\tau_s A}}{\eta_{\text{mB}}} [\eta_{\text{fwd}} T_{\text{atm}} (1 - e^{-\tau_s A}) + (1 - \eta_{\text{fwd}}) T_{\text{cab}} + T_{\text{rec}}], \quad (1.9)$$

where G_{im} is the *gain* of the image sideband compared to the signal sideband ($G_{\text{im}} = 1$ for an ideal dual-sideband receiver, $G_{\text{im}} = 0$ for an ideal single-sideband receiver), η_{fwd} is the telescope forward efficiency, A is the airmass ($A \approx 1/\cos(z)$ for zenith angles $z \lesssim 70^\circ$), τ_s is the *atmospheric opacity* in the signal band, T_{atm} the mean physical atmospheric temperature, T_{cab} is the ambient temperature in the receiver cabin, and T_{rec} is the noise equivalent temperature of the receiver and the optics. All those parameters are easily measured, except for τ_s , which depends on the amount of water vapor in the atmosphere and which is estimated by complex atmospheric models. Note, that reduction of the image gain $G_{\text{im}} = 1 \rightarrow 0$, which has been the key idea behind single-sideband receivers, does not imply reduction of T_{sys} by a factor of two; every change of G_{im} modifies T_{rec} , and hence the answer whether reduction of the image gain improves the noise performance is not straightforward, and depends on the relative noise contributions from the atmosphere and instrument (see Jewell & Mangum 1999, for a detailed discussion).

The basic conclusion from this formula is that noise, given by Eq. (1.8), does not depend on the source brightness, which is not the case in e.g. optical imaging, where (Poisson) noise increases with the square-root of signal. In microwave astronomy, however, even the brightest sources generate only small signal excess on top of the signal generated by the atmosphere, telescope, and receiver, and therefore are incapable of increasing T_{sys} by a measurable amount. For this reason, the source term is not present in Eq. (1.9), and we can safely assume, that noise at the peak of a spectral line is the same as in its vicinity⁴, which is easy to measure.

Example. Consider observations around 562 GHz with a single-polarization double-sideband receiver of MIRO ($T_{\text{rec}} = 3600$ K, $G_{\text{im}} = 1$). The instrument is in space (hence $\tau_s = 0$, $A = 0$), and the receiver cabin is very cold $T_{\text{cab}} \ll T_{\text{rec}}$. Assume $\eta_{\text{mB}} = 0.95$. From Eq. (1.9) we have $T_{\text{sys}} = 7579$ K. The Chirp-Transform Spectrometer (CTS) onboard MIRO has 44-kHz spectral channels. Assume a 300-sec integration, 100% duty cycle, and noiseless performance of the CTS. The radiometer formula (Eq. 1.8) yields $\sigma_{T_{\text{mB}}} = 2.1$ K. However, MIRO will observe in a frequency-switching mode, therefore 300 sec of integration will provide only $\sigma_{T_{\text{mB}}} = 4.2$ K in a fully calibrated spectrum. Such a spectrum will show the same line twice; a recombined spectrum will thus provide $\sigma_{T_{\text{mB}}} = 2.95$ K, which yields the actual 3σ detection limit equal to $T_{\text{mB}} = 3 \sigma_{T_{\text{mB}}} = 8.85$ K. See Chapter 5 for more information about possible science with MIRO.

⁴Note, that most of the parameters in Eq. (1.9) depend on the observed frequency, and therefore noise can be considered as constant only in a limited spectral range.

1.3 Basic mathematical formulations

1.3.1 Constant isotropic emission

Consider a spherical nucleus which emits molecules isotropically at a constant rate Q . Let us also assume that these molecules have an infinite lifetime, and that they move radially outwards with a constant velocity v_{gas} . Now let us derive the volume number density ϱ_v of the molecules.

Think of a thin shell surrounding the nucleus at a distance r , the thickness of which is dr , and which contains dn molecules. The number of molecules entering the shell in the time interval dt is $dn_{\text{in}} = Q dt$. Simultaneously, the number of molecules leaving the shell is $dn_{\text{out}} = dn v_{\text{gas}} dt/dr$. Now, assuming a steady state, that is $dn_{\text{out}} = dn_{\text{in}}$, we obtain $dn = Q/v_{\text{gas}} dr$, and dividing both sides by the volume of the shell, which is $dV = 4\pi r^2 dr$, we end up with:

$$\varrho_v(r) \equiv \frac{dn}{dV} = \frac{Q}{4\pi r^2 v_{\text{gas}}}. \quad (1.10)$$

By integrating this equation along the line of sight, the position on which is given by s , we obtain the column density of the molecules ϱ_c :

$$\varrho_c(\rho) \equiv \int_{-\infty}^{+\infty} \varrho_v(s, \rho) ds = \frac{Q}{4\rho v_{\text{gas}}}, \quad (1.11)$$

where $\rho = \sqrt{r^2 - s^2}$ is the distance between the nucleus and the considered line of sight in the observing plane.

1.3.2 Propagation of microwave radiation through the coma

Propagation of microwave radiation along a linear path is governed by the *radiative transfer* equation:

$$\frac{dI_\nu(s)}{ds} = j_\nu(s) - \alpha_\nu(s)I_\nu(s), \quad (1.12)$$

where I_ν [$\text{J s}^{-1} \text{ m}^{-2} \text{ sr}^{-1} \text{ Hz}^{-1}$] is the *spectral intensity*, j_ν [$\text{J s}^{-1} \text{ m}^{-3} \text{ sr}^{-1} \text{ Hz}^{-1}$] is the volume *spectral emissivity*, and α_ν [m^{-1}] is the linear *absorption coefficient* (note that [$\text{s}^{-1} \text{ Hz}^{-1}$] formally cancels out). Within a medium, this equation balances the gains due to emission (the first term on the right-hand side) with the losses due to self-absorption (the second term). Spectral emissivity j_ν is defined as:

$$j_\nu \equiv \frac{\varrho_v}{4\pi} f_u A_{ul} h\nu_0 \psi(\nu, \nu_0), \quad (1.13)$$

and absorption coefficient α_ν as:

$$\alpha_\nu \equiv \frac{\varrho_v}{4\pi} (f_l B_{lu} - f_u B_{ul}) h\nu_0 \psi(\nu, \nu_0), \quad (1.14)$$

where f_u and f_l are the fractions of molecules occupying the upper and lower energy levels respectively; A_{ul} [$\text{s}^{-1} \text{ molec}^{-1}$], B_{ul} and B_{lu} [$\text{J}^{-1} \text{ s}^{-1} \text{ m}^2 \text{ sr molec}^{-1}$] are the three *Einstein coefficients*: for *spontaneous emission*, *forced emission* and *absorption*, respectively; $h =$

$6.626068 \times 10^{-34} \text{ J Hz}^{-1}$ is the Planck constant, ν_0 is the transition frequency [Hz], and $\psi [\text{Hz}^{-1}]$ is the normalized line profile, such that $\int_0^\infty \psi(\nu, \nu_0) d\nu \equiv 1$. Moreover, $B_{lu}/B_{ul} = g_u/g_l$ and $A_{ul} = (2h\nu^3/c^2) B_{ul}$, where g_u and g_l are the levels' statistical weights.

Equation (1.12) greatly simplifies for the *optically-thin* emission, where the absorption is negligible compared to the emission. Since it is generally the case for the cometary lines accessible from ground, this will be a standard assumption from now on throughout this thesis (the only exception is made in Chapter 5 where full radiative transfer treatment has been applied). In such case we obtain:

$$\frac{dI_\nu(s)}{ds} = j_\nu(s), \quad (1.15)$$

which can be readily integrated to provide the total spectral intensity I_ν generated along the considered path:

$$I_\nu = \int_{-\infty}^{+\infty} j_\nu(s) ds, \quad (1.16)$$

or, after substituting Eq. (1.13),

$$I_\nu = \frac{1}{4\pi} A_{ul} h\nu_0 \psi(\nu, \nu_0) \int_{-\infty}^{+\infty} f_u(s) \varrho_\nu(s) ds, \quad (1.17)$$

which is the most general formulation of I_ν in the optically-thin limit.

Equation (1.16) can be rewritten in terms of the absorption coefficient and *source function* $S_\nu \equiv j_\nu/\alpha_\nu$:

$$I_\nu = \int_{-\infty}^{+\infty} \alpha_\nu(s) S_\nu(s) ds, \quad (1.18)$$

which shows, that although in the considered optically-thin case α_ν is assumed to cause a negligible self-absorption, one would simply blunder concluding $\alpha_\nu \equiv 0$; in fact there would be no emission at all in such case (that is, $I_\nu \equiv 0$), which is not the assumption of the optically-thin approximation! Note, that substituting Eq. (1.13) and Eq. (1.14) with the corresponding relations into the above definition of S_ν , we obtain:

$$S_\nu = \frac{2h\nu^3}{c^2} \frac{1}{\frac{g_u f_l}{g_l f_u} - 1}. \quad (1.19)$$

Whereas a general solution for the energy-levels distribution requires detailed time-dependent *statistical-equilibrium* calculations, it is very convenient to assume *thermal equilibrium*, which is the case for inner comae of active comets. Under this condition, the fractional occupancy of energy level i is given by the *Boltzmann distribution*:

$$f_i = \frac{g_i e^{-E_i/kT}}{Z(T)}, \quad (1.20)$$

where E_i is the energy of considered level, and $Z(T) = \sum_i g_i e^{-E_i/kT}$ is the *partition function*.

It is trivial to show, that the Boltzmann distribution implies that the source function is given by the *Planck's law*:

$$S_\nu(T) = \frac{2h\nu^3}{c^2} \frac{1}{e^{\frac{h\nu}{kT}} - 1}. \quad (1.21)$$

Note that the Planck's spectrum is a continuum. A question arises then, how this is possible that such profile is relevant for the molecular emissions, which are observed as discrete lines? The answer is simple: the absorption coefficient peaks sharply at a line-specific frequency, and otherwise is practically equal to zero. It therefore picks up some intensity from the Planck function, and zeroes the spectrum otherwise.

The absorption coefficient can be conveniently determined (practically for any interesting transition) from several spectral line catalogs. For example, taking the *integrated line intensity* $I(\nu, T)$ [$\text{m}^2 \text{Hz}^{-1} \text{molec}^{-1}$] from the JPL spectral line catalog⁵ (Pickett et al. 1998), we obtain the absorption coefficient as:

$$\alpha_\nu(T) = \varrho_\nu I(\nu_0, T) \frac{\nu}{\nu_0} \psi(\nu, \nu_0). \quad (1.22)$$

Let us assume now that the gas temperature T is constant along the path. Since $S_\nu(s) = \text{const}$ in such case, and substituting Eq. (1.22) into Eq. (1.19), we obtain:

$$I_\nu = I(\nu_0, T) \frac{\nu}{\nu_0} \psi(\nu, \nu_0) S_\nu(T) \int_{-\infty}^{+\infty} \varrho_\nu(s) ds, \quad (1.23)$$

which, for a steady-state coma described by Eq. (1.11), leads to:

$$I_\nu = I(\nu_0, T) \frac{\nu}{\nu_0} \psi(\nu, \nu_0) S_\nu(T) \frac{Q}{4\rho v_{\text{gas}}}. \quad (1.24)$$

Finally, reformulating the above equation in terms of the brightness temperature (see Eq. 1.6), we obtain:

$$T_B = \frac{c^2}{2k\nu^2} I(\nu_0, T) \frac{\nu}{\nu_0} \psi(\nu, \nu_0) S_\nu(T) \frac{Q}{4\rho v_{\text{gas}}}. \quad (1.25)$$

Note, that an alternative formulation, which also assumes thermal equilibrium (Eq. 1.20) with $T = \text{const}$ and isotropic coma (Eq. 1.11), but does not involve the catalog integrated line intensity I , can be derived directly from Eq. (1.17):

$$T_B = \frac{c^2}{2k\nu^2} \frac{1}{4\pi} A_{ul} h\nu_0 \psi(\nu, \nu_0) \frac{g_u e^{-E_u/kT}}{Z(T)} \frac{Q}{4\rho v_{\text{gas}}}, \quad (1.26)$$

however, we will continue our derivations based on the former one (Eq. 1.25).

⁵Available at <http://spec.jpl.nasa.gov>. Note that the integrated line intensity is provided for $T = 300 \text{ K}$, hence requires an adequate scaling to a lower temperature if a realistic cometary gas is considered.

1.3.3 Integration within a Gaussian beam

Substituting now Eq. (1.25) and Eq. (1.1) into the definition of main-beam brightness temperature in Eq. (1.7), we obtain:

$$T_{\text{mB}}(\nu) = \frac{c^2}{2k\nu^2} \mathcal{I}(\nu_0, T) \frac{\nu}{\nu_0} \psi(\nu, \nu_0) S_\nu(T) \frac{Q}{4\nu_{\text{gas}}} \frac{\int_0^{2\pi} \int_0^\infty e^{-\frac{\rho^2}{\sigma^2}} d\rho d\phi}{\int_0^{2\pi} \int_0^\infty \rho e^{-\frac{\rho^2}{\sigma^2}} d\rho d\phi}. \quad (1.27)$$

It can be shown that:

$$\begin{aligned} \int_0^{2\pi} \int_0^\infty e^{-\frac{\rho^2}{\sigma^2}} d\rho d\phi &= \frac{1}{2} \sigma \sqrt{\pi}, \\ \int_0^{2\pi} \int_0^\infty \rho e^{-\frac{\rho^2}{\sigma^2}} d\rho d\phi &= \frac{1}{2} \sigma^2, \end{aligned} \quad (1.28)$$

hence we obtain:

$$T_{\text{mB}}(\nu) = \frac{c^2}{2k\nu^2} \mathcal{I}(\nu_0, T) \frac{\nu}{\nu_0} \psi(\nu, \nu_0) S_\nu(T) \frac{Q}{4\nu_{\text{gas}}} \frac{\sqrt{\pi}}{\sigma}. \quad (1.29)$$

Substituting now Eq. (1.21), and Eq. (1.3) with $\sigma_{\frac{1}{2}} = \sqrt{\ln 2} \sigma$, we obtain:

$$T_{\text{mB}}(\nu) = \frac{\sqrt{\pi \ln 2}}{2} \frac{h}{kc} \mathcal{I}(\nu_0, T) \frac{\nu^3}{\nu_0} \psi(\nu, \nu_0) (e^{h\nu/kT} - 1) \frac{D}{b\Delta} \frac{Q}{\nu_{\text{gas}}}, \quad (1.30)$$

which provides the link between the observed microwave spectrum and the basic physical properties of the comet.

1.3.4 Derivation of the line area

We can now integrate Eq. (1.30) over all frequencies in order to determine the *line area*:

$$\int_0^\infty T_{\text{mB}}(\nu) d\nu = \frac{\sqrt{\pi \ln 2}}{2} \frac{h}{kc} \mathcal{I}(\nu_0, T) \frac{1}{\nu_0} \frac{D}{b\Delta} \frac{Q}{\nu_{\text{gas}}} \int_0^\infty \nu^3 \psi(\nu, \nu_0) (e^{h\nu/kT} - 1) d\nu. \quad (1.31)$$

We note that $\psi(\nu, \nu_0)$ is different from zero only for $\nu \approx \nu_0$, and that $\int_0^\infty \psi(\nu, \nu_0) d\nu \equiv 1$, which greatly simplifies the integration:

$$\int_0^\infty \nu^3 \psi(\nu, \nu_0) (e^{h\nu/kT} - 1) d\nu = \nu_0^3 (e^{h\nu_0/kT} - 1), \quad (1.32)$$

and leads to:

$$\int_0^\infty T_{\text{mB}}(\nu) d\nu = \frac{\sqrt{\pi \ln 2}}{2} \frac{h}{kc} \mathcal{I}(\nu_0, T) \nu_0^2 (e^{h\nu_0/kT} - 1) \frac{D}{b\Delta} \frac{Q}{\nu_{\text{gas}}}. \quad (1.33)$$

Note that the line area resulting from the above equation is given in [K Hz]. It is, however, convenient to determine it in the commonly used radial-velocity scale in [K m s⁻¹]. Changing hence the domain of integration $d\nu \rightarrow dv_r$ with Eq. (1.5), we obtain:

$$\int_{-\infty}^{+\infty} T_{\text{mB}}(v_r) dv_r = \frac{\sqrt{\pi \ln 2} h}{2} \frac{I(\nu_0, T)}{k} \nu_0 (e^{h\nu_0/kT} - 1) \frac{D}{b\Delta} \frac{Q}{\nu_{\text{gas}}}. \quad (1.34)$$

An alternative formulation, derived from Eq. (1.26), is

$$\int_{-\infty}^{+\infty} T_{\text{mB}}(v_r) dv_r = \frac{\sqrt{\pi \ln 2} hc^2}{16\pi} \frac{g_u A_{ul}}{k} \frac{e^{-E_u/kT}}{\nu_0} \frac{D}{Z(T)} \frac{Q}{b\Delta \nu_{\text{gas}}}, \quad (1.35)$$

which immediately implies

$$-E_u/T = \ln \left(\frac{\nu_0}{g_u A_{ul}} \int_{-\infty}^{+\infty} T_{\text{mB}}(v_r) dv_r \right) + \text{const} \quad (1.36)$$

for different lines of the same molecule. It provides a convenient way of determining T , and is called the *rotational diagram* technique. Note that ν_0^p has a different power-index p if a different observable is provided; i.e. $p = 0$ for $\int_0^{+\infty} T_{\text{mB}}(\nu) d\nu$, $p = 1$ for $\int_0^{+\infty} T_{\text{B}}(\nu) d\nu$, and p is increased by 1 when we change the integration domain for dv_r .

The line area $\int_{-\infty}^{+\infty} T_{\text{mB}}(v_r) dv_r$, though used permanently in microwave spectroscopy, has not been assigned its own symbol yet. It is often written in an abbreviated integral form as $\int T_{\text{mB}} d\nu$, which has been also used throughout this thesis.

2 Comet

73P/Schwassmann-Wachmann 3

2.1 Introduction

More than 40 comets are known to have split, producing several hundred fragments (Boehnhardt 2004). However, except for rare cases of cometary disruption by tidal forces due to close approaches to the Sun or to Jupiter, the causes of cometary splitting are still unknown. One candidate mechanism is rotational break-up, when the centrifugal force surpasses the nucleus self gravity and tensile strength (cf. e.g. Davidsson 1999, 2001).

The hypothesis of rotational splitting is testable: a rotation period of a main fragment, which is close to the disruption threshold shortly after the break-up, would be suggestive of rotational splitting. On the other hand, a long rotation period after break-up does not necessarily exclude rotational splitting, because cometary nuclei may change their spin state very rapidly, especially those highly active and of a small size (cf. e.g. Samarasinha et al. 1986, Jewitt 1999, Gutiérrez et al. 2002).

Comet 73P/Schwassmann-Wachmann 3 (hereafter SW3) was discovered in 1930 by Arnold Schwassmann and Arno Arthur Wachmann (Hamburg Observatory, Germany), around the perigee of its orbit at only 0.06 AU from the Earth. It is a short-period Jupiter Family Comet, with an orbital period of 5.36 years. The comet broke up into at least four pieces in 1995 (Boehnhardt & Kauf 1995, Scotti et al. 1996), and the splitting was accompanied by an outburst (Crovisier et al. 1995, Hale et al. 1995, Morris et al. 1995). Three of the components were re-detected during their next perihelion passage in 2000/2001 (Kadota et al. 2000). While the geometry of the apparition of SW3 in 2000/2001 was unfavorable, the comet approached the Earth to less than 0.1 AU in May 2006, displaying over 60 fragments (Weaver 2006, also see Fig. 2.1). Of all of them, fragment C is the largest, about 0.5 km in radius (Toth et al. 2005, 2006, Nolan et al. 2006).

The exceptionally close approach of comet SW3 was a good opportunity to search for variability in the emission of parent molecules, stimulated by the nucleus rotation. Using a typical (sub-) millimeter facility, the telescope beam radius was of the order of 1000 km at the comet, ensuring that most of the observed emission originated from the inner coma, so that most of the material left the nucleus within less than an hour before the observation. Therefore periodicities with a period longer than one hour might have been detected.

We undertook such study using the HCN molecule, because it is believed to sublimate directly from the nucleus surface, and it offers the brightest emission lines for ground-based (sub-) millimeter observations. This makes it ideal for investigating rotation of

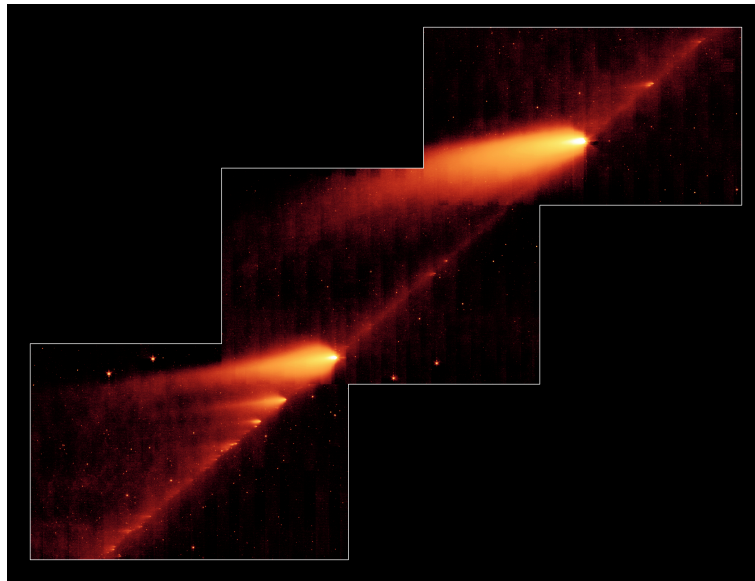


Figure 2.1: Comet SW3 observed by the Spitzer Space Telescope at $24\ \mu\text{m}$ (thermal radiation of dust) between May 4 and 6, 2006.

a cometary nucleus. According to Huebner et al. (1992), 97% of the molecules photodissociate into H and CN, with a lifetime of 22 h at 1 AU from the (quiet) Sun. This corresponds to a scale-length of 60 000 km, assuming a typical gas expansion velocity at this heliocentric distance. Furthermore, CN is one of the brightest radicals observed in cometary spectra in the visible range, thus the HCN–CN connection is the best studied parent–daughter relation in cometary comae. However, it is still not clear if HCN is the only important parent of CN (see e.g. Bockelée-Morvan & Crovisier 1985, Fray et al. 2005). The production rate of HCN is of the order of 0.1% relative to water, and this ratio is remarkably constant over large range of heliocentric distances and very similar for many comets (cf. Biver et al. 2002b, Bockelée-Morvan et al. 2004a).

In this chapter we show selected results from our observations of comet SW3 at (sub-) millimeter wavelengths in May 2006. They have been published already by Drahus et al. (2009) in the same form. In Section 2.2 we present our data and outline the reduction steps. Section 2.3 shows an evolution of the line position with phase angle. In Section 2.4 we determine and discuss the production rates of HCN, and in Section 2.5 we use them to investigate the rotation of the nucleus. Finally, Section 2.6 summarizes this work, and presents our conclusions for future studies. In Section 2.7 we additionally present a supplementary discussion which justifies our assumptions from Sections 2.4 and 2.5.

2.2 Observations and data reduction

We monitored comet SW3 at (sub-) millimeter wavelengths between May 1 and 22, 2006, searching for different molecules in the two brightest fragments (designated as C and B). However, in this thesis we focus only on the results of our observations of the HCN emission from fragment C (hereafter SW3-C).

We used the 10.0-m Heinrich-Hertz Submillimeter Telescope (Baars & Martin 1996,

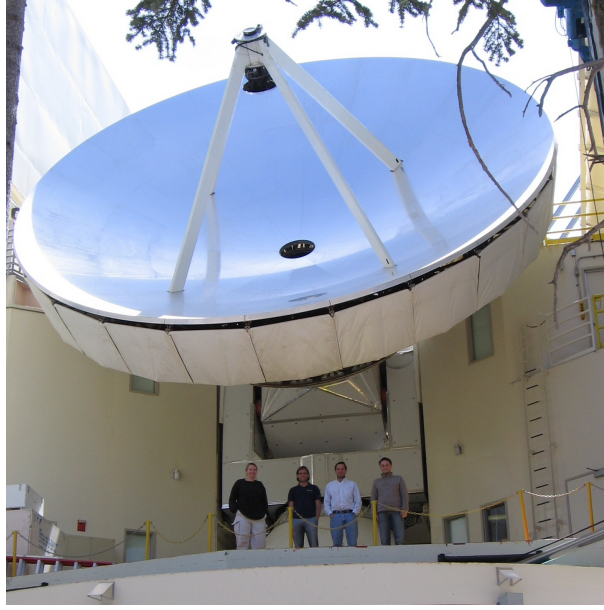


Figure 2.2: The 10-m Submillimeter Telescope on Mt. Graham (Arizona).

Baars et al. 1999) at Mt. Graham International Observatory in Arizona (hereafter SMT; see Fig. 2.2). Depending on atmospheric transmission we either used the 1.3-mm JT single-sideband SIS receiver or the 345-GHz double-sideband SIS receiver, to observe HCN through the $J(3-2)$ or $J(4-3)$ rotational transitions. Both receivers are dual channel.

Spectral analysis was performed using the facility Acousto-Optical Spectrometers AOS-A and AOS-B with a total bandwidth of 1 GHz and 2048 nominal channels each; however, the real resolution of the spectrometers is 934 kHz for AOS-A and 913 kHz for AOS-B, so the linear CCD elements oversample the spectra by about a factor of two. These two spectrometers were always connected to the two channels of the receivers, allowing us to improve the S/N by averaging results from the horizontal and vertical polarizations. Co-adding spectra taken at different polarizations was problematic due to the different arrangement and slightly different width of the spectral channels in each spectrometer.

For all derivations we approximate the beam as a symmetric Gaussian, whose FWHM is given (in radians) by:

$$\text{FWHM} = \frac{c b}{\nu D}, \quad (2.1)$$

where c is the speed of light, ν is observed frequency, D is dish diameter, equal to 10 m for the SMT, and b is a dimensionless factor, intrinsic to every dish, which is equal to 1.25 for the SMT (cf. Eq. 1.2 in Chapter 1.3.4). The half-power angular radius of the beam was therefore 14.5'' at the lower frequency and 11'' at the higher one.

The position of the comet was continually calculated from the orbital elements provided by the JPL HORIZONS system¹ for the epoch of our observations. The pointing was calibrated on Jupiter, Saturn, and most frequently on the protoplanetary nebula CRL2688 that was close to the comet. From the stability of these observations we concluded that the pointing error was at worst of the order of half the beam radius at half-

¹<http://ssd.jpl.nasa.gov/?horizons>

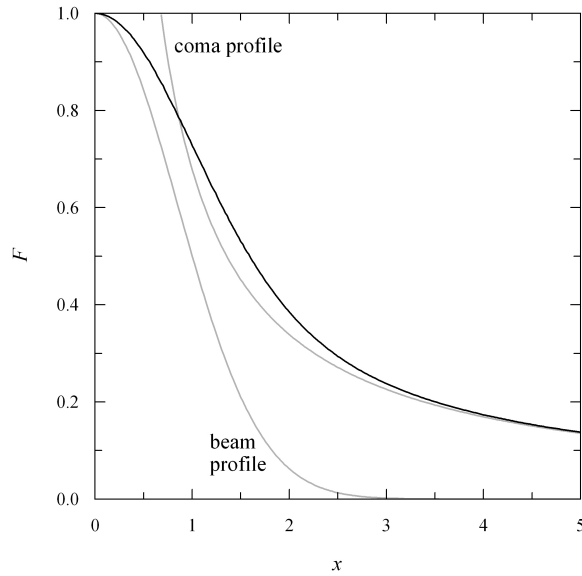


Figure 2.3: Loss of the normalized flux F due to a relative pointing offset x (measured in units of the beam radius at half-power). The dependence was derived for our model coma (further described in Section 2.4.1) and for the assumed beam pattern (see Eq. 2.1), both profiles being shown for comparison.

power (7'' or 5'' depending on the observed frequency) for the observations accepted for analysis (see further in this section). Such precision is an order of magnitude worse than that guaranteed by the ephemeris but it still ensures that the flux loss is below 10% (see Fig. 2.3).

The spectra were taken in a position switching mode, using a 0.5° offset in azimuth where the coma contamination is negligible. We used a 15 sec integration time for the ON and also a 15 sec integration time for the OFF position, and each spectrum was composed of 8 or 10 ON–OFF pairs, thus giving us a fundamental time resolution of 4 or 5 min (hereafter exposure).

The moments of observations were not corrected for the travel time of light as the correction was negligible (see the geocentric distances in Table 2.1). They are approximately mid-points of the exposures, but not exactly: we added halves of the exposures to the initialization moments of the spectra, but neglected the time taken by the initial calibrations, switching time, time losses when the telescope was blown off the position, etc.

The absolute temperature scale was calibrated using the chopper wheel method (see e.g. Ulich & Haas 1976, Kutner & Ulich 1981), which automatically corrects for absorption in the Earth's atmosphere, resistive antenna losses, and rearward spillover and scattering terminated at ambient temperature (see e.g. Kutner & Ulich 1981). Furthermore, we corrected the temperature scale for the main beam efficiency η_{mB} , which we found to be equal to 0.60 ± 0.04 (at both monitored frequencies) using our observations of continuum in Venus, Mars, Jupiter, and Saturn.

Because a typical edge tapering of 12 dB reduces the maximum power level of the first sidelobe to less than 0.3% of the power level of the main beam, the sidelobes do not contribute significantly to the convolution result of the antenna pattern with planetary discs or coma brightness distribution. Furthermore, as long as the main beam pattern

is similar to the assumed Gaussian profile (which is the case for e.g. an edge tapered Airy profile), the influence of a small error in the assumed beam width on cometary observations will be largely compensated for by the main beam efficiency factor (affected similarly if calculated using the same assumed beam).

The frequency scale was converted to the radial-velocity scale (negative velocities indicate blueshift), and corrected for the radial velocity of the comet with respect to the telescope. We used 265.88643392 GHz as the central rest frequency of the $J(3-2)$ transition, and 354.50548084 GHz for the $J(4-3)$ one. These frequencies are the optocenters of the complete hyperfine structures as listed in the Cologne Database for Molecular Spectroscopy² (Müller et al. 2005).

For each single spectrum the line area $\int T_{\text{mB}} dv$ was determined from a velocity interval between -3 and $+3$ km s⁻¹, and two symmetric intervals from -10 to -3 km s⁻¹ and from $+3$ to $+10$ km s⁻¹ were used to estimate the background level. The background was subtracted upon fitting a linear baseline with a 3σ iterative rejection of “bad” spectral channels. Additionally, information about noise in the background was used to estimate a statistical error of the line area, assuming that both the line and the background have identical noise levels. After this procedure was applied separately to the spectra from AOS-A and AOS-B, the resulting line areas were averaged (with the same statistical weights), and the effective errors were calculated. Figure 2.4 shows an example of such individual spectra for both the $J(3-2)$ and the $J(4-3)$ transitions. Since the effect of oversampling is not clearly visible, possibly due to an additional source of noise which partly removed the correlation between neighboring channels, for simplicity, we analyzed the spectra as their channels were completely independent.

To ensure consistency of the absolute calibration and stability of the instrumentation, we periodically (about each 90 min) monitored standard calibration sources on the sky, namely CRL2688, W51D, DR21, and W3(OH). Within one night and for a fixed instrumental setup we found intensity drops of up to 50%, which we believe to be caused directly or indirectly (via pointing calibration) by anomalous refraction (Altenhoff et al. 1987). To ensure a consistent and properly calibrated time series of cometary HCN intensity, we restricted our observations in the following way:

- (i) we rejected the nights suffering from an insufficient monitoring of the calibration sources,
- (ii) we rejected the nights during which we encountered instabilities of the calibration sources larger than 20%,
- (iii) post-factum we restricted the time series to the measurements with the production rate errors below 1.2×10^{25} molec s⁻¹ (calculation of the production rates is further described in Section 2.4.1) and hence rejected 7 observations; additionally, we rejected the last 3 observations from May 10, 2006, whose errors are significantly higher than those of the earlier data that night.

²Available at <http://www.astro.uni-koeln.de/site/vorhersagen/>. Note that the main database does not resolve the hyperfine components of the HCN lines. The resolved hyperfine structure of the first five rotational transitions is available separately, at http://www.astro.uni-koeln.de/cdms/daten/HCN/HCN/c027501_hfs.cat. The frequency of the $J(4-3)$ transition in the main database corresponds to one of the hyperfine components, and it slightly differs from the optocenter of the whole structure.

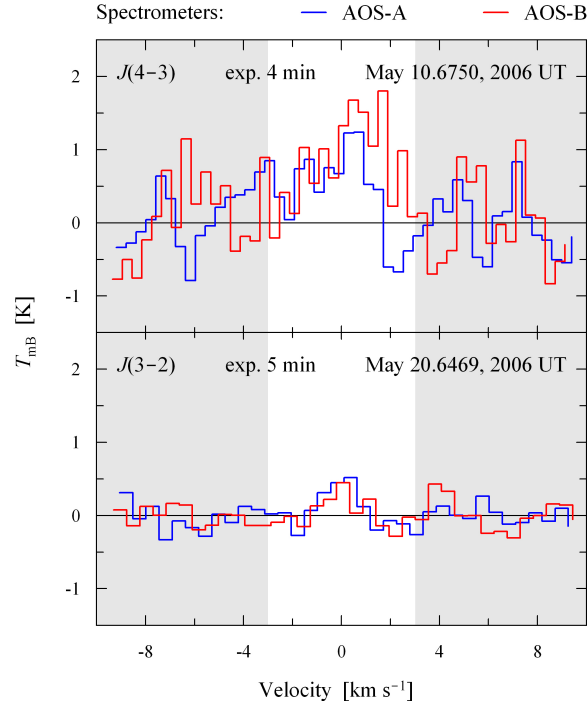


Figure 2.4: Examples of individual calibrated spectra. The panels show the spectra with maximum (upper) and minimum (lower) mean value of $\int T_{\text{mB}} d\nu$ from both AOS spectrometers. The white region shows the range used for calculating the line area, and the gray regions show the ranges used for fitting the background.

Finally, collected over 5 days (Table 2.1) were 124 individual measurements of the line area $\int T_{\text{mB}} d\nu$ (Table 2.2), which we used for further analysis. The errors on the line area include only the statistical component, since the other error sources, discussed in this section, are of a different nature (systematic and/or maximum) and are often negligibly small. Visual inspection of Table 2.2 shows, that occasionally a difference between neighboring measurements exceeds very significantly an acceptable range indicated by the errors. Although we cannot explain this effect, we assume it has a negligible influence on our analysis due to its rareness and apparently stochastic nature. Additionally, in Fig. 2.5 we present the weighted-mean spectra, obtained upon averaging the selected observations separately for each night, where the weights were inversely proportional to the square of the background noise.

2.3 Line position in the night-averaged spectra

Using the night-averaged spectra (illustrated in Fig. 2.5) we calculated positions of the lines (on a common velocity scale), defined as points splitting line area into halves. An error of the position was estimated using the Monte Carlo approach: on each spectrum we superimposed 1000 noise realizations, and in each individual simulation we determined the line position. The scatter of the obtained values is a very good measure of the investigated uncertainty, therefore, as the error we adopted the standard deviation calculated with respect to the original line position. While simulating noise we assumed a Gaussian noise

Table 2.1: Journal of the observations.

Date UT ^a (May 2006)	Line	\mathcal{N} ^b	Tot. exp. ^c [min]	r ^d [AU]	Δ ^e [AU]	ϕ ^f [°]	λ ^g [°]	β ^h [°]	Beam ⁱ [km]
10.4979	$J(4-3)$	44	176	1.0214	0.0803	79.445	310.247	49.912	635
11.6885	$J(3-2)$	13	65	1.0148	0.0789	84.287	319.050	45.545	831
12.5524	$J(3-2)$	15	75	1.0101	0.0786	87.816	324.738	41.924	829
20.6222	$J(3-2)$	41	205	0.9732	0.1054	108.715	354.173	9.206	1112
22.4882	$J(3-2)$	11	55	0.9664	0.1167	110.039	357.585	4.196	1231

^aMiddle moment of an individual observing run.

^bNumber of observations.

^cTotal exposure. Individual exposures were consequently 4 min (first night) and 5 min (other nights).

^dHeliocentric distance.

^eGeocentric distance.

^fPhase angle.

^gEcliptic longitude.

^hEcliptic latitude.

ⁱBeam radius at half-power at comet's distance.

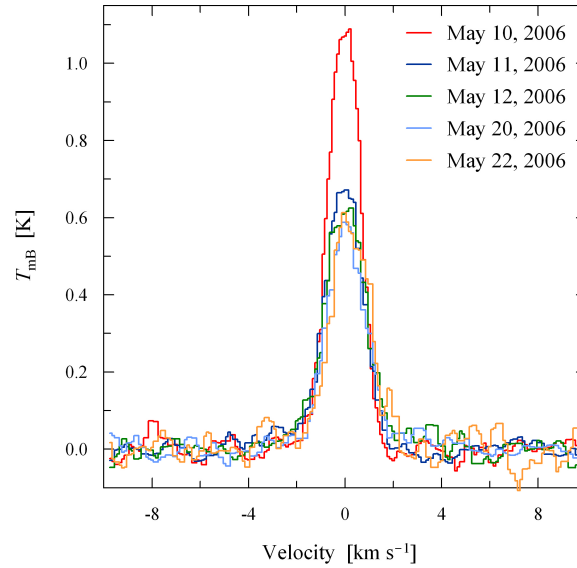


Figure 2.5: Night-averaged calibrated spectra. The line for May 10, 2006 (red line) is more intense than the others because it results from a different transition (cf. discussion in Section 2.7.1.6). The total exposure for each night is listed in Table 2.1. The constituent spectra were re-binned to a common arrangement of channels, each 0.1 km s^{-1} wide, which made it possible to average the spectra from AOS-A and AOS-B. Note that these new channels are not independent.

Table 2.2: Observations of the HCN molecule with the AOS spectrometers.

Date UT (May 2006)	$\int T_{\text{mB}} d\nu$ [K km s ⁻¹]	Date UT (May 2006)	$\int T_{\text{mB}} d\nu$ [K km s ⁻¹]	Date UT (May 2006)	$\int T_{\text{mB}} d\nu$ [K km s ⁻¹]
10.3167	1.29 ± 0.36	10.6750	3.71 ± 0.65	20.5781	1.30 ± 0.23
10.3201	2.08 ± 0.38	10.6792	2.41 ± 0.55	20.5830	1.27 ± 0.23
10.3243	2.43 ± 0.34	11.6646	1.42 ± 0.16	20.5885	0.88 ± 0.22
10.3278	2.01 ± 0.34	11.6687	1.61 ± 0.17	20.5934	1.56 ± 0.22
10.3320	1.94 ± 0.50	11.6729	1.33 ± 0.18	20.5983	0.82 ± 0.25
10.3361	1.25 ± 0.31	11.6764	1.33 ± 0.23	20.6031	1.14 ± 0.33
10.3396	1.36 ± 0.32	11.6806	1.54 ± 0.17	20.6087	1.19 ± 0.27
10.3438	1.68 ± 0.32	11.6847	1.33 ± 0.17	20.6135	1.39 ± 0.26
10.3472	1.95 ± 0.42	11.6882	1.35 ± 0.19	20.6372	1.17 ± 0.30
10.3514	1.53 ± 0.38	11.6924	1.29 ± 0.18	20.6420	1.23 ± 0.31
10.3555	2.31 ± 0.30	11.6958	1.27 ± 0.18	20.6469	0.26 ± 0.26
10.3590	1.42 ± 0.34	11.7000	1.06 ± 0.21	20.6517	1.11 ± 0.25
10.3632	2.16 ± 0.29	11.7049	0.61 ± 0.18	20.6573	0.61 ± 0.18
10.3674	0.82 ± 0.33	11.7083	1.34 ± 0.23	20.6622	0.94 ± 0.21
10.3715	2.40 ± 0.28	11.7125	1.08 ± 0.19	20.6670	1.05 ± 0.21
10.4361	1.61 ± 0.39	12.3788	1.78 ± 0.21	20.6719	1.42 ± 0.28
10.4403	1.88 ± 0.25	12.3837	1.03 ± 0.26	20.6767	1.03 ± 0.27
10.4445	1.71 ± 0.30	12.6441	1.74 ± 0.18	20.6823	1.51 ± 0.25
10.4486	1.03 ± 0.32	12.6489	1.52 ± 0.21	20.6872	0.64 ± 0.29
10.4535	1.37 ± 0.23	12.6538	1.44 ± 0.21	20.6920	1.12 ± 0.22
10.4576	2.15 ± 0.23	12.6587	1.61 ± 0.17	20.7260	1.06 ± 0.39
10.4618	2.01 ± 0.20	12.6635	1.88 ± 0.19	20.7309	0.73 ± 0.35
10.4667	0.98 ± 0.35	12.6691	1.14 ± 0.18	20.7358	1.48 ± 0.35
10.4708	1.08 ± 0.26	12.6739	1.16 ± 0.23	20.7406	1.75 ± 0.28
10.4757	1.82 ± 0.27	12.6788	1.34 ± 0.32	20.7455	1.71 ± 0.35
10.4805	1.45 ± 0.28	12.6837	1.53 ± 0.19	20.7497	0.98 ± 0.23
10.4854	1.08 ± 0.31	12.6885	1.14 ± 0.21	20.7545	0.76 ± 0.31
10.5903	2.12 ± 0.32	12.7163	1.18 ± 0.26	20.7594	0.94 ± 0.35
10.5945	2.37 ± 0.31	12.7212	1.49 ± 0.24	20.7691	0.55 ± 0.36
10.5986	2.51 ± 0.31	12.7260	1.17 ± 0.25	20.7739	0.82 ± 0.27
10.6021	1.80 ± 0.27	20.4705	2.14 ± 0.33	22.4642	1.19 ± 0.23
10.6063	1.96 ± 0.28	20.4795	1.45 ± 0.41	22.4684	2.35 ± 0.36
10.6104	1.64 ± 0.33	20.4844	1.46 ± 0.37	22.4733	1.06 ± 0.31
10.6146	0.76 ± 0.32	20.4892	1.56 ± 0.33	22.4781	0.62 ± 0.20
10.6188	1.76 ± 0.35	20.4941	0.62 ± 0.36	22.4830	0.59 ± 0.30
10.6222	2.14 ± 0.43	20.4989	2.09 ± 0.26	22.4879	1.02 ± 0.32
10.6264	2.72 ± 0.35	20.5038	1.34 ± 0.24	22.4927	1.02 ± 0.30
10.6305	2.02 ± 0.49	20.5580	1.36 ± 0.25	22.4976	1.59 ± 0.24
10.6347	3.06 ± 0.32	20.5635	1.51 ± 0.29	22.5024	1.38 ± 0.21
10.6382	1.91 ± 0.43	20.5684	1.91 ± 0.32	22.5073	0.58 ± 0.35
10.6424	2.17 ± 0.49	20.5733	1.94 ± 0.20	22.5122	1.65 ± 0.22
10.6465	2.91 ± 0.40				

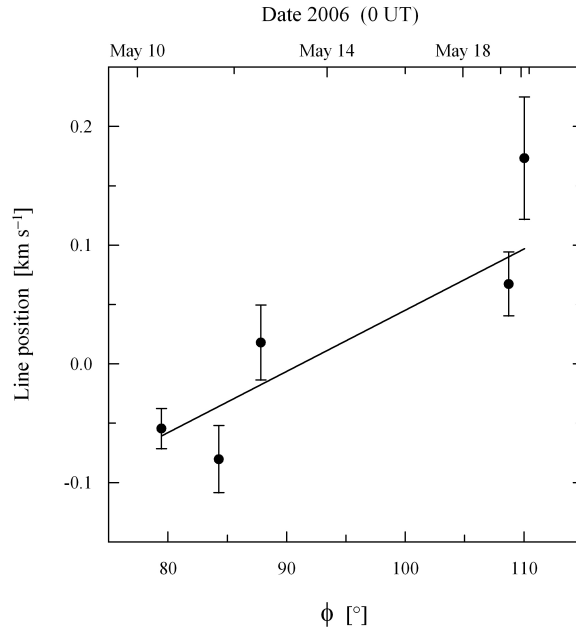


Figure 2.6: Evolution of the line position in the night-averaged spectra (illustrated in Fig. 2.5) with phase angle ϕ . The solid line shows a weighted linear fit to guide the eye.

distribution, with a variance determined from the background noise (see Section 2.2) – thus identical for all the channels within one spectrum. Although as the references for the simulations we ideally should have used noiseless representations of the real data, in this specific case Gaussian fits featured noticeably shifted centers, thus we used the investigated spectra themselves. We followed these procedures separately for the night-averaged spectra from AOS-A and AOS-B, hence preserving the original arrangement of their channels. Finally we determined the mean positions from both spectrometers, which are presented versus phase angle ϕ in Fig. 2.6.

It is clearly visible that the lines became redder with the increasing phase angle ϕ . This effect is expected for outgassing stimulated by the Sun, whose position controls the temperature, and hence the sublimation rate, over the nucleus. Moreover, the line position equal to nearly zero at $\phi = 90^\circ$ indicates that at that moment the distribution of the outgassing rate was symmetric with respect to some direction perpendicular to the line of sight (reaching a maximum in this direction), which might have been exactly Sunward. The scatter of the line positions about the global trend well corresponds to their errors estimated from the background noise (which would be even slightly underestimated if the spectral channels were partly correlated – see Section 2.2). Clearly, the observed trend contains a lot more information about the activity of this comet, however, in order to retrieve them we would have to model the complete line profiles in the individual (i.e. not night-averaged) spectra, which is impossible due to the too large noise. Note that this effect should be accompanied by an evolution of the line area $\int T_{\text{mB}} dv$ with phase angle ϕ , as we model it in Section 2.7.1.5, but we did not investigate our data in this respect due to its small magnitude and because it partly overlaps with the heliocentric trend (see Section 2.4.2).

2.4 Production rate of the HCN molecule

2.4.1 Model and parameters

In order to retrieve a production rate Q (that is the global outgassing rate of a given molecule) from a measurement of the line area $\int T_{\text{mB}} dv$, a model involving kinematics, chemistry, and excitation of the molecules, along with light propagation properties, must be used. For the purpose of our derivation we assume that:

- (i) the coma is optically thin at the observed frequencies,
- (ii) LTE conditions are present throughout the coma,
- (iii) the volume density of the molecules is inversely proportional to the square of the nucleocentric distance, i.e. the photodissociation process is neglected,
- (iv) the molecules are isotropically ejected from the nucleus,
- (v) the production rate Q is constant in time,
- (vi) the expansion velocity v_{exp} and the temperature T of the molecules are constant in space and time; under LTE, the excitation temperature is equal to the kinetic temperature, therefore we simply refer to the gas temperature.

Under these assumptions the production rate Q depends linearly on the line area $\int T_{\text{mB}} dv$ (cf. Eq. 1.34 in Chapter 1):

$$Q = \frac{2}{\sqrt{\pi \ln 2}} \frac{k}{h} \frac{b \Delta v_{\text{exp}}}{D I(T) \nu} (e^{h\nu/kT} - 1) \int T_{\text{mB}} dv, \quad (2.2)$$

where k and h are the Boltzmann and the Planck constants respectively, Δ is the geocentric distance, and $I(T)$ is the integrated line intensity (at temperature T) as defined in the JPL spectral line catalog³ (Pickett et al. 1998). In this equation the same approximation of the beam is used as given by Eq. (2.1). Note that in order to calculate Q in molecules per second, $\int T_{\text{mB}} dv$ must be provided in the commonly used unit of K m s^{-1} .

Unfortunately, we could not observe several HCN lines simultaneously, which would have enabled us to derive the gas temperature T (by e.g. solving Eq. 2.2 simultaneously for the production rate and the temperature itself, or equivalently, by applying the rotational diagram technique – see Chapter 1.3.4). Instead, we adopted $T = 80 \text{ K}$.

Supplying our model with this temperature, we determined the HCN expansion velocity v_{exp} , using the line widths determined from the night-averaged spectra (Fig. 2.5). We found $v_{\text{exp}} = 0.8 \pm 0.1 \text{ km s}^{-1}$, which is a mean value from the results obtained individually for each single night, and its error is the standard deviation among the constituent measurements.

A detailed justification of the assumptions of our model and of the input parameters is presented in Section 2.7.1.

³Available online at <http://spec.jpl.nasa.gov/>. Note that the integrated line intensity is provided for $T = 300 \text{ K}$, hence requires an adequate scaling to a lower temperature if a realistic cometary gas is considered.

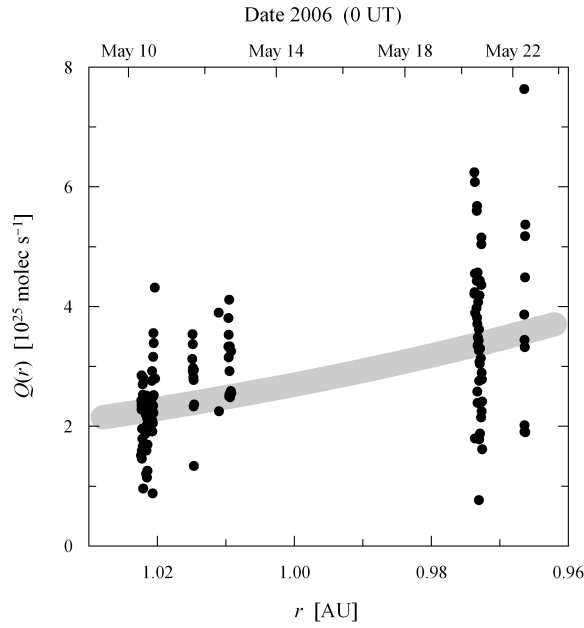


Figure 2.7: Evolution of the HCN production rate Q with heliocentric distance r . The gray line shows the best power-law fit.

2.4.2 Individual production rates

Using the simple model (Section 2.4.1) we converted each individual measurement of the line area $\int T_{\text{mB}} d\nu$ (see Table 2.2) into the corresponding HCN production rate Q , and analyzed how they change with the heliocentric distance r of the comet (see Fig. 2.7). An unweighted power-law fit to this dependence yields the power index of -8.2 ± 1.4 and the mean production rate $\langle Q_0 \rangle = (2.70 \pm 0.09) \times 10^{25} \text{ molec s}^{-1}$ at $r = 1 \text{ AU}$ (indicated by index “zero”), corresponding to $1.22 \pm 0.04 \text{ kg s}^{-1}$. Since heliocentric evolution of the HCN production rate typically follows power laws with indices between 2 and 5 (see e.g. Biver et al. 1999, 2002a), the obtained dependence should be considered as unusually steep. The likely reason for this difference is the very limited range of heliocentric distances covered by our observations, thus the obtained evolution shows only an instantaneous behavior of this comet.

Nevertheless, the ultimate goal of obtaining this dependence was to remove this instantaneous heliocentric trend from the production rate in order to search for its cyclic changes that might have been driven by the nucleus rotation. As further shown in Section 2.5, this effect may be responsible for the large scatter of the measurements about the fit. Thus, the presented snapshot of the heliocentric dependence concerns, strictly speaking, the mean diurnal production rate, provided that the rotation phase was sampled fairly uniformly. This is discussed in more detail in Section 2.7.2.

This also means that the derived errors of the fit parameters – resulting purely from the scatter of the measurements – are artificially boosted by the short-term variability of the production rate about its mean-diurnal value. On the other hand, they do not account (at least not directly) for the simplifications of our model and the uncertainties of its input parameters (Section 2.4.1), the instrumental effects and the individual errors resulting from the noise statistics (Section 2.2), and sampling of the nucleus rotation phases (Sec-

tion 2.7.2).

Using the determined trend we reduced all the individual measurements to $r = 1$ AU, and denoted them as Q_0 . Their errors are the statistical uncertainties on the line area $\int T_{\text{mB}} dv$ (see Section 2.2) converted with Eq. (2.2) and reduced with the same trend. Hence they neither account for the several effects discussed in Section 2.2, nor for the simplifications of our model (Section 2.4.1) or the uncertainty on the heliocentric trend derived in this section. The reason is that all these effects are of a different nature (systematic and/or maximum), whereas it is the relative uncertainty between the individual Q_0 , not the absolute one, which matters for the periodicity analysis.

2.4.3 Discussion

The determined expansion velocity is typical for a comet at this heliocentric distance (cf. e.g. Biver et al. 1999, 2002a), and is consistent with theoretical models (see e.g. Bockelée-Morvan & Crovisier 1987).

The mean diurnal HCN production rate at $r = 1$ AU is generally consistent with other corresponding determinations, published by Milam et al. (2006), Villanueva et al. (2006), and Dello Russo et al. (2007), though discrepancies up to a factor of 3 exist. They can be explained by different heliocentric distances and observing geometries of the comet (the latter being further discussed in Section 2.7.1.4), along with modulation induced by the nucleus rotation (further discussed in Section 2.5). Inconsistencies between the different techniques also cannot be excluded (cf. e.g. Magee-Sauer et al. 1999, Fray et al. 2005).

Furthermore, we compared our result with the corresponding values for eight other comets. Whenever necessary we normalized their production rates using a power-law heliocentric dependence with an exponent of -4 . This is between the values of -4.5 and -3.4 , obtained from the long-term pre- and post-perihelion evolution of the HCN production rate in comet Hale-Bopp (Biver et al. 2002a), though the slope was noticeably flatter for comet Hyakutake (Biver et al. 1999). The correction was significant only for comet Tempel 1 (observed at $r = 1.62$ AU), and moderate for comet Borrelly (observed at $r = 1.36$ AU). The comparison is presented in Fig. 2.8, where the production rates Q_0 are plotted vs. the nuclei radii R , along with the best fit of a square function (calculated in logarithmic space); that is because the total nucleus area is the main parameter controlling the global sublimation. The dependence shows that the HCN production rate in SW3-C was unusually high. Since the abundance of this molecule was found to be typical (Villanueva et al. 2006), only an exceptionally high surface volatility – that is a large active fraction – can explain this. The conclusion is on one hand not surprising, bearing in mind the former break-up which excavated much fresh and highly volatile material; on the other hand, the comet has been continually losing its excessive activity since then (Boehnhardt 2004), and though it was unusually active a decade later. The dependence also shows that at $r = 1$ AU a typical nucleus with the radius of $R = 1$ km produces HCN at the rate of $1.5^{+8.7}_{-1.3} \times 10^{25}$ molec s^{-1} (corresponding to $0.7^{+3.9}_{-0.6}$ kg s^{-1}). Covering nearly 4 orders of the nucleus area, the analysis is fairly insensitive to the errors on individual data points, introduced by observing noise, particular models, normalizations, etc. Therefore, the scatter of the points is most likely dominated by diversity among the surface volatilities, with some contamination from differences in composition and shape.

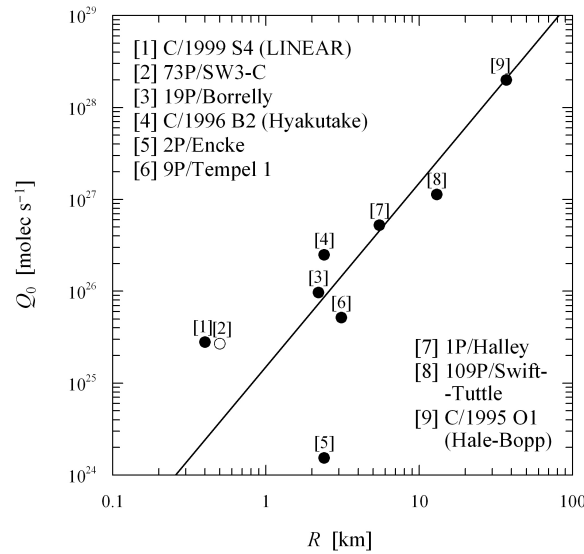


Figure 2.8: Compilation of the HCN production rates Q_0 (normalized to $r = 1$ AU) for comets with known nucleus radius R . The solid line shows the fit of a square function. Except for SW3-C (see ref. in Section 2.1), the radii were taken from Lamy et al. (2004), and the production rates from: [1] Bockelée-Morvan et al. (2001), [2] this work (see Section 2.4.2), [3] Bockelée-Morvan et al. (2004b), [4] Biver et al. (1999), [5] Woodney et al. (2003), [6] Biver et al. (2007), [7] Schloerb et al. (1986), [8] Bockelée-Morvan et al. (1994b), and [9] Biver et al. (2002a).

2.5 Rotation period of the nucleus

2.5.1 Basic concepts

An active cometary nucleus may manifest its rotation by stimulating a periodic variation of the global outgassing rate, induced by diurnal changes of the insolation over the active region(s). Also a uniformly volatile nucleus may produce such variability provided that its shape is irregular – hence the effective sublimation area varies as the insolation changes during the rotation cycle. In principle, for both scenarios the observed rotation phase profile of the production rate may be noticeably different from the one which is intrinsic to the nucleus; they should be, however, quite similar in our case (see Section 2.7.1.5).

Rotation periods have been determined for many cometary nuclei, both active and inactive, using several different techniques (see e.g. Jorda & Gutiérrez 2000, Samarasinha et al. 2004). However, periodic variability of the parent molecule production rate, stimulated by the nucleus rotation, has been detected only very recently, by Biver et al. (2007) for HCN in comet 9P/Tempel 1 (the Deep Impact target). Although the rotation period they found is consistent with the determination from optical photometry of the bare nucleus (see Lamy et al. 2007) – thus providing a double-peak phasing of the light curve – the phase profile for HCN features only one peak. Moreover, this profile is well correlated with periodic oscillations of the line position, which were also detected by Biver et al. (2007). This demonstrates that the phase profiles for HCN and for the optical light curve are indeed controlled by different underlying mechanisms.

A clear advantage of using a time series of parent molecule production rate to inves-

tigate the rotation of active comets is high probability of detecting a phase profile with a large amplitude A (which we define as a ratio of maximum to minimum of the phase profile). This will be the case if the sublimation is indeed restricted to a limited number of isolated sources, and the observations closely reflect an intrinsic activity pattern of the surface, satisfying the conditions discussed in Section 2.7.1.5. This contrasts with low amplitudes of the phase profiles for daughter species and for dust. The former one is damped by the significant excess velocities (in random directions) gained during their photodissociative creation, and also due to the exponential nature and long time scale of this process, both effects making the spacetime distribution of daughter species more uniform. The latter is damped because of low and simultaneously size-dependent velocities of dust grains; it was also postulated that dust ejection may be driven more by sublimation of the most volatile ices (CO , CO_2) than by water ice (Feaga et al. 2007), which is weakly sensitive to the diurnal changes of the insolation conditions. Moreover, if a large field of view or long exposures are used, then the rotation-driven variability of any coma component (i.e., daughter species, dust, or parent molecules) is additionally damped (cf. Section 2.7.1.5). An example of these effects are observations of comet Tempel 1: compare the HCN phase profile ($A = 2.3$) reported by Biver et al. (2007) – although it is expected to differ noticeably from the intrinsic one (thus they call it *apparent*) – with the CN and dust phase profiles ($A = 1.5$ and $A < 1.5$ respectively) inferred by Manfroid et al. (2007).

Another approach is to investigate a (diurnal) variability of the outgassing direction instead of (or along with) variations of the production rates. Such an effect stimulates the variability of the line position and shape over the rotation cycle. Requiring spectral resolutions of at least one million, this approach is feasible only for radio techniques. The rotation-driven variability of the line shape and/or position was first identified for comet Hale-Bopp (Henry et al. 2002, Boissier et al. 2007), and later found for Tempel 1 (Biver et al. 2007).

Unfortunately, investigating periodicity in the line position in our individual spectra of SW3-C we found only random noise. Although an evolution with the phase angle is evident in the night-averaged spectra (see Section 2.3), there is no hint of the rotation-driven variability also there, though it might have manifested itself by producing an excess scatter in the trend (if different rotation phases of the nucleus were sampled on different nights). A possible explanation for this non-detection is simply an insufficient S/N of the individual spectra, causing too large an uncertainty on the line position. Alternatively, a specific combination of the spin axis orientation and the nucleus activity pattern might have kept the line position and shape fairly constant over the rotation cycle. Therefore, we limit our further discussion to the variability of the production rate, which is independent of the line position variability.

2.5.2 Methods

Performing the periodicity analysis we generally followed the *classical* approach of Drahus & Waniak (2006), where a constant frequency f of the periodicity in the input data is being determined. Although they also introduced a *dynamical* approach, where an evolution of the frequency with time df/dt is simultaneously searched for, we did not apply it to our data.

It has been well established, both in theory (e.g. Samarasinha et al. 1986, Jewitt 1999, Gutiérrez et al. 2002) and through observations (e.g. Belton & Drahus 2007, Drahus & Waniak 2006, and references therein), that the cometary nuclei, especially those that are small and active, can substantially change their rotation periods on a time scale of a single perihelion passage. Using the simple model of Drahus & Waniak (2006) we estimated that the expected change of the rotation frequency of SW3-C during our campaign, regardless of the frequency itself, is about 0.04 h^{-1} (Section 2.7.3.2). In the rotation phase profile for the middle frequency this corresponds to the shift of the first and last data point of more than a full rotation cycle, making the *classical* periodicity analysis completely irrelevant. At the same time their *dynamical* approach, naturally accounting for this effect, would be ideal.

Nevertheless, we have decided to limit our investigation to the *classical* analysis only – although it seems incorrect at the moment – due to the insufficient quality of our data for the *dynamical* approach. Drahus & Waniak (2006) have successfully tested the routine using simulations with a S/N of about 3, i.e. comparable with their best observing results (where S/N is defined as half of the difference between maximum and minimum of the phase profile over the standard deviation of the points about their smooth representation), and using 128 synthetic data points, i.e. the same number as observed. On the other hand, the additional parameter may lead to failure of this approach when the S/N is worse and/or the number of input data points is smaller (Waniak & Drahus, in preparation). In our case the number of measurements is very similar, but the S/N, being below 2 for half of the considered period solutions (further discussed in Section 2.5.3, particularly in Fig. 2.10), does not guarantee sufficient reliability of the *dynamical* investigation. Nevertheless, we show in Section 2.7.3.2 that – in contrast to our expectations – the analysis done within the frame of a constant (and simple) periodicity approximation is probably justifiable in our case.

We performed the periodicity analysis using two different methods: the Phase Dispersion Minimization, originally proposed by Stellingwerf (1978), and generalized by Drahus & Waniak (2006) in order to take statistical weights of individual data points into account (hereafter WPDM, where “W” indicates weighting), and the χ^2 minimization using a sum of harmonics fitted to the data that also accounts for the statistical weights of the individual measurements (hereafter HF, which stands for *harmonics fit*). Both methods return a variance ratio Θ which measures the quality of a phase profile at given frequency f . Generally, the lower the value of Θ is, the better the profile it indicates. The working parameters of WPDM are the number of bins and the number of covers (denoted as N_b and N_c respectively) and the only parameter of HF is the number of frequencies used for fitting (denoted as N_f).

The error on the frequency f of a given periodicity solution was estimated using the Monte Carlo approach, in a similar way as the error on line position (see Section 2.3). As the reference for a simulation we used a smooth counterpart of the original phase profile, which we calculated using the HF method. (Note that we used HF for two different reasons: as an independent periodicity-search routine, and in order to obtain a noiseless representation of a given phase profile.) The smooth profile was then disturbed with a large number of noise realizations, which we produced assuming a Gaussian noise distribution with variance given by the square of the data point error. The simulated noisy phase profiles were analyzed with the same method and setting which originally had re-

turned the solution whose error was under study. As the investigated error we adopted a standard deviation of the values from the simulations, calculated with respect to the actual frequency of the investigated solution. Note that such an approach naturally converts an uncertainty on the input data into a standard error of periodicity (Drahus & Waniak 2006).

Moreover, we also retrieved the probabilities that any phase profile – characterized by a certain value of Θ_0 – does not result entirely from noise. Such confidence levels were derived also using the Monte Carlo method. Again, we simulated a number of noise realizations, taking however a constant reference curve this time. Then, they were analyzed using both methods with given settings, yet only global minima of Θ were retrieved. This made it possible to constrain individual statistics $N(\Theta < \Theta_0)$ for each method and setting, which provided the confidence levels for Θ_0 .

2.5.3 Results

Both methods were used to investigate our production rates Q_0 , normalized to $r = 1$ AU using the best-fit heliocentric dependence (see Section 2.4.2). We scrutinized the range of frequencies f from 0.02 to 0.8 h^{-1} (corresponding to the periods P from 1.25 to 50 h), with a step size of 0.00002 h^{-1} . As the statistical weights of the individual measurements we used the inverse squares of their errors. The WPDM algorithm was run with N_b ranging from 15 to 35, and $N_c = 5$, whereas the HF method was used with N_f ranging from 3 to 7. The most relevant periodograms were found for $N_b = 25$ (corresponding to 5 measurements per bin on average) and $N_f = 5$. This is because when working with noticeably lower values of these parameters, the methods do not return the whole set of existing solutions, whereas when using much higher values they do not provide any additional solutions and are less stable due to the limited number of input measurements. For both methods we retrieved the confidence levels of detection using a simulation with 1000 realizations of noise. The optimal periodograms are displayed in Fig. 2.9, along with the ones calculated for $N_b = 15$ and $N_f = 3$, as well as for $N_b = 35$ and $N_f = 7$, which we show for comparison.

The figure shows a good consistence of the results from different methods and parameters. Although a number of solutions are present, only few of them are significant in a statistical sense. We selected eight most likely solutions, which were found in the following way: first we identified all the solutions characterized in at least one periodogram by the Θ value not higher than 5% above the minimum value in the considered periodogram. Next, we rejected all the solutions at $f < 0.07 \text{ h}^{-1}$ ($P > 14.3 \text{ h}$) as they suffer from an insufficient phase coverage with our data. For each of the accepted solutions we retrieved the Monte Carlo error, considering separately the two positions from the two methods with the optimum settings (representing the same solution). As the reference profiles for the simulations we used smooth fits from the HF method with $N_f = 5$ for the solutions at $f < 0.1 \text{ h}^{-1}$ and $N_f = 3$ for those at $f > 0.1 \text{ h}^{-1}$, which provide the most realistic representations of the data. Onto each of them we superimposed 1000 noise realizations. As the final solutions we adopted the combined results from both methods. The positions of the selected solutions are listed in Table 2.3, and the phase profiles are displayed in Fig. 2.10.

Half of these solutions, i.e. A, D, E, and F, form a system of period multiples which starts with solution F (see Table 2.4). Some further multiples are also visible in the pe-

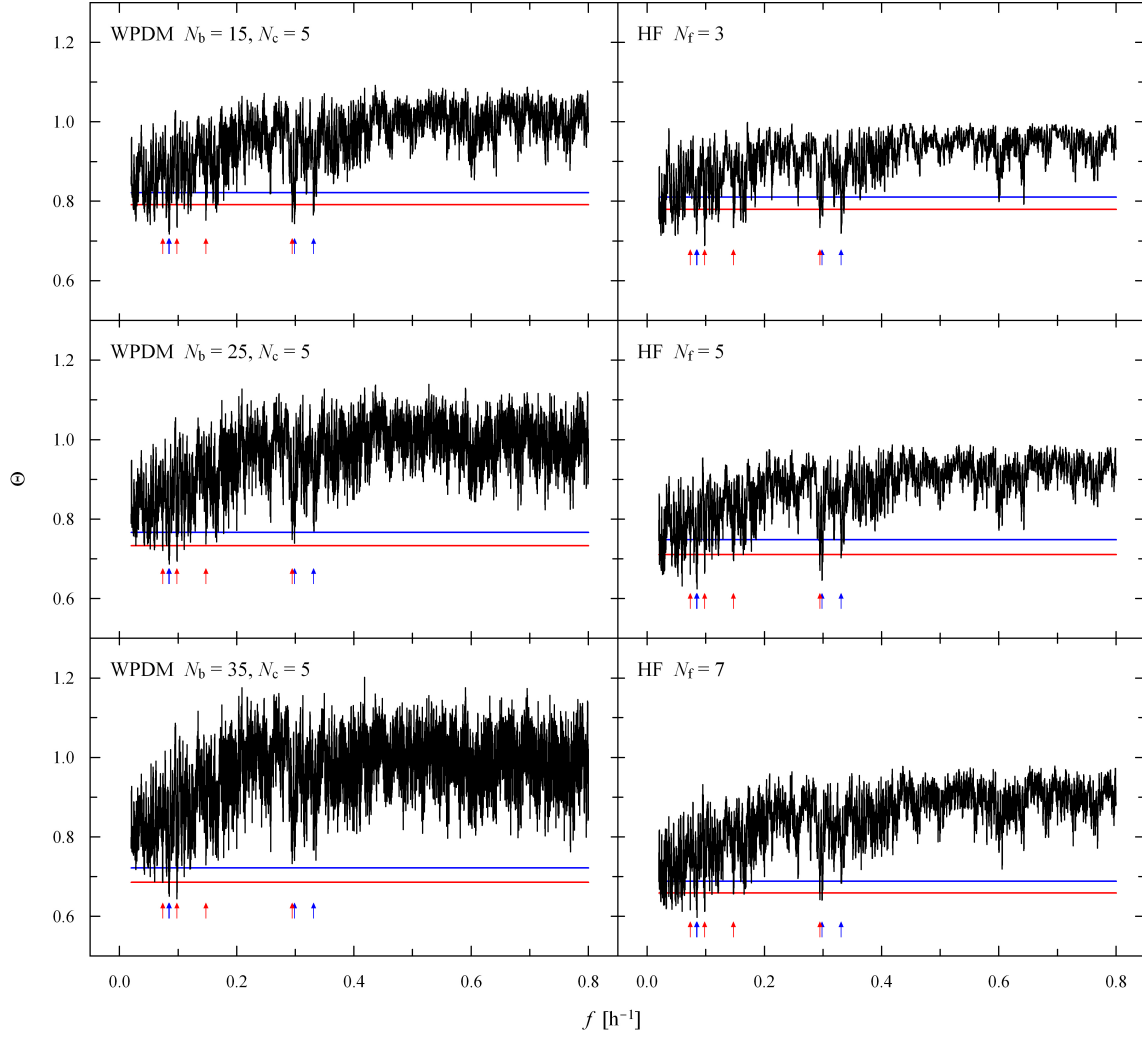


Figure 2.9: Selected results from the search for periodicity in the normalized HCN production rates Q_0 . The left panels show the periodograms obtained with the WPDM algorithm and the right ones with the HF method. The horizontal lines indicate the confidence levels of 75% (blue) and 95% (red). Positions of the eight best solutions (Table 2.3) are indicated by the arrows: red for those from the system and blue for the others. Solutions B and C are barely resolved in this figure.

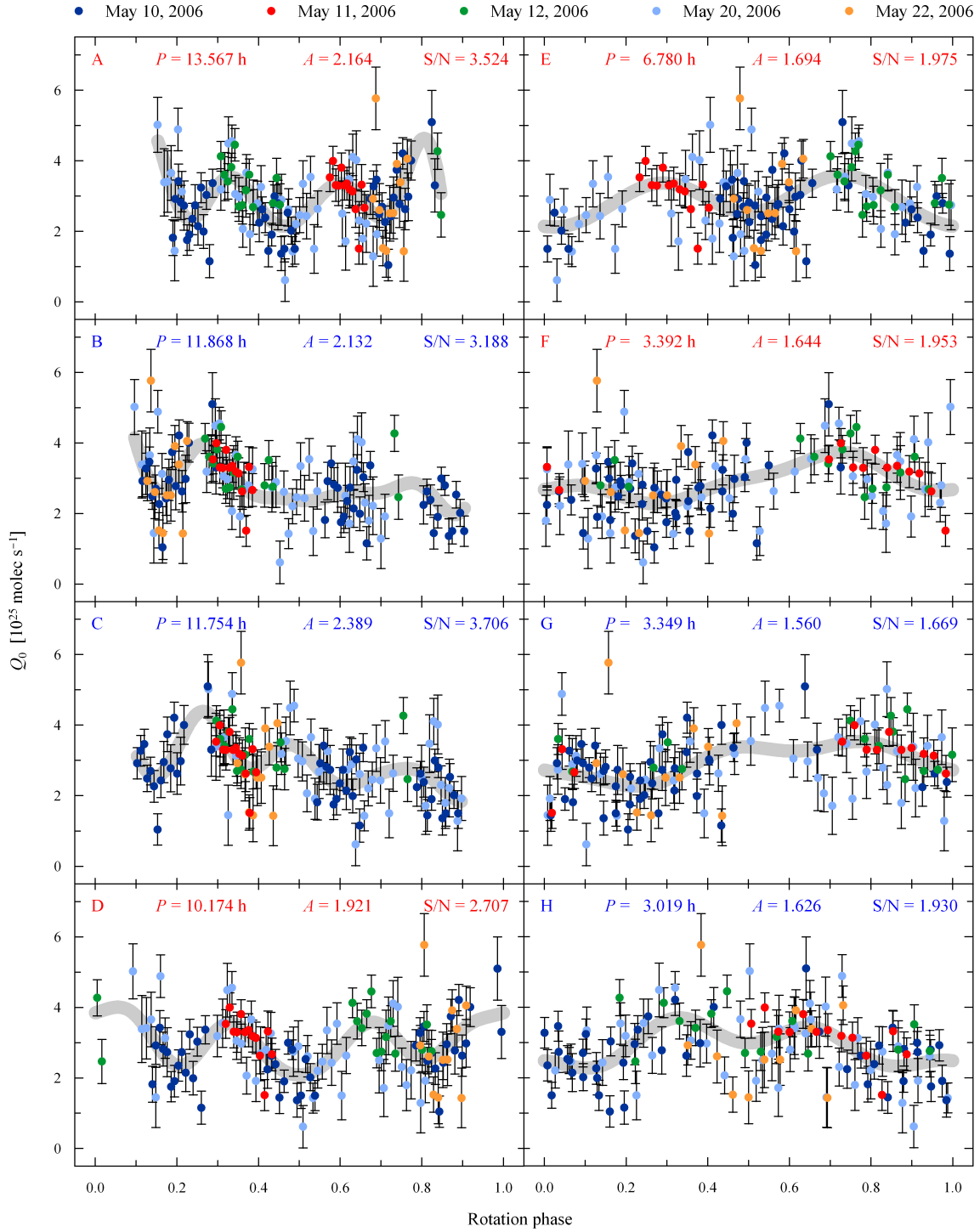


Figure 2.10: Phasings of the normalized HCN production rates Q_0 according to the eight best solutions (see Table 2.3) with periods P . The red and blue fonts are used for easy distinction between the system and the other solutions respectively. The smooth fits (gray lines) were used as the reference profiles to calculate the errors of the discussed solutions. They also provide us with the amplitudes A and enable calculation of the S/N.

Table 2.3: Possible solutions for periodicity.

Solution ^a	f_{WPDM}^b [h ⁻¹]	f_{HF}^c [h ⁻¹]	f^d [h ⁻¹]	P^e [h]
A	0.07372 ± 0.00004	0.07370 ± 0.00003	0.07371 ± 0.00004	13.567 ± 0.007
B	0.08428 ± 0.00008	0.08424 ± 0.00004	0.08426 ± 0.00006	11.868 ± 0.009
C	0.08512 ± 0.00008	0.08504 ± 0.00005	0.08508 ± 0.00007	11.754 ± 0.009
D	0.09832 ± 0.00007	0.09826 ± 0.00005	0.09829 ± 0.00006	10.174 ± 0.006
E	0.14742 ± 0.00016	0.14758 ± 0.00012	0.14750 ± 0.00014	6.780 ± 0.006
F	0.29474 ± 0.00024	0.29480 ± 0.00019	0.29477 ± 0.00021	3.392 ± 0.002
G	0.29862 ± 0.00022	0.29860 ± 0.00020	0.29861 ± 0.00021	3.349 ± 0.002
H	0.33128 ± 0.00015	0.33112 ± 0.00012	0.33120 ± 0.00014	3.019 ± 0.001

^aID of the system solutions (red) and of the other solutions (blue).

^b $N_b = 25$, $N_c = 5$.

^c $N_f = 5$.

^dUnweighted-mean result from both methods with an effective error.

^eCorresponding period with an error.

riodograms, although they do not satisfy our aforementioned requirements for a “good” solution. The system is so precise that all its constituents are found within a fraction of their errors from the expected frequencies. The reason that our periodograms are dominated by this structure is the very simple shape of the phase profile for its base frequency (solution F), which is nearly sinusoidal and features only one peak (what actually defines this solution as a base of the system). Therefore, it can be easily decomposed into the associated multiples, with slowly increasing complexity – each succeeding solution in the system features one additional peak in its phase profile, where all the peaks are images of the phase profile for the base frequency. Since the complexity of the profiles rises slowly, the system can be traced up to high period multiples (i.e. low frequencies), but of course at some point the profiles become overly complex, and the number of data points too low, thus the system vanishes. On the other hand we cannot exclude the possibility, that some multi-peak solution from this system is actually the correct one, which – just because of an unusually high symmetry – created the whole structure. However, in such a case, multiple, equiproductive, and equidistant (in the nucleocentric longitude) active sources are required, or an irregular nucleus with fairly uniform surface volatility must be assumed (if a double-peak solution E is considered) – but both scenarios are very specific, thus improbable in our opinion. At the same time, all the independent solutions, unrelated to the system, are physically very plausible. The requirements of symmetry are not relevant to them, being violated (otherwise the solutions would not be independent, being multiples of simpler periodicities). Therefore, the phase profiles are irregular, often featuring asymmetric multiple peaks (typically characterized by uneven amplitudes and/or unequidistant positions). Although these solutions are bases, they do not produce sharp systems of their multiples, due to rapid growth of the complexity (although in some cases first multiples are weakly visible).

Summarizing, we found a periodic oscillation of the reduced production rate Q_0 with the amplitude factor of 1.6–2.4 and S/N of 1.7–3.7, depending on phasing. The most likely explanation of this effect is a variation of activity over the nucleus rotation cycle, but our observations alone are insufficient to unambiguously point at the correct rotation period.

Table 2.4: Properties of the periodicity solutions.

Solution ^a	f ^b [h ⁻¹]	M ^c	f_{fit} ^d [h ⁻¹]	σ ^e	A ^f	S/N ^g
A	0.07371 ± 0.00004	4	0.07372	0.19	2.164	3.524
B	0.08426 ± 0.00006				2.132	3.188
C	0.08508 ± 0.00007				2.389	3.706
D	0.09829 ± 0.00006	3	0.09829	0.01	1.921	2.707
E	0.14750 ± 0.00014	2	0.14743	0.48	1.694	1.975
F	0.29477 ± 0.00021	1	0.29487	0.46	1.644	1.953
G	0.29861 ± 0.00021				1.560	1.669
H	0.33120 ± 0.00014				1.626	1.930

^aID of the system solutions (red) and of the other solutions (blue).

^bDetermined frequency of periodicity.

^cMultiplicity number for the system. $M = 1$ indicates the base of the system.

^dFrequency expected for an ideal system, given by an unweighted linear fit to the dependence of f on M .

^eDeviation of frequency f_{fit} from f , given as a fraction of the error on f .

^fAmplitude; see Section 2.5.1 and Fig. 2.10.

^gSignal-to-Noise ratio; see Section 2.5.2 and Fig. 2.10.

Possible problems which might have affected our analysis are discussed in Section 2.7.3.

2.5.4 Discussion

In Section 2.5.3 we concluded, that solutions A, E, and D (see Table 2.4), which are multiples of solution F, require a very symmetric distribution of the sublimation sources or a uniformly volatile nucleus surface (in the case of solution E), both scenarios being specific thus unlikely in our opinion. This is supported by observations of the rotation phase profiles of coma in other comets, which are either simple one-peak sinusoids (cf. e.g. Schleicher & Osip 2002, Biver et al. 2007) or irregular (cf. e.g. Drahus & Waniak 2006, Manfroid et al. 2007). Although sometimes it is difficult to choose between a single-peak phase profile or its double-peak multiple (e.g. Schleicher et al. 1991, Schleicher & Osip 2002), to our knowledge a symmetric multi-peak shape has never been unambiguously claimed.

However, an argument supporting the multi-peak phase profiles may also be raised. Sekanina (2005) shows, that on September 6, 1995 two fragments (i.e. B and E) broke-up from SW3-C, and then on November 2, 1995 fragment F additionally disconnected. Provided that SW3-C did not experience further splitting, one may expect on its surface one major active region related to fragment B, and two weaker – associated with the smaller fragments E and F, interfering with the original activity pattern on the rest of the surface. It is not clear however, if the break-up induced active sources, created a decade before, survived until our campaign in 2006: although the comet was still exceptionally active (see Section 2.4.3), it has been continually loosing its excessive productivity since it broke up (Boehnhardt 2004). Moreover, one should bear in mind that the real activity pattern does not necessarily well correspond to the observed phase profile (see Section 2.7.1.5).

An important argument regarding the true rotation period comes from the analysis of two additional data sets, presented in Section 2.7.3.4. The analysis clearly supports the shortest-period solutions, which are the most stable against distortions of the original

Table 2.5: Other determinations of the rotation period P of SW3-C.

Mid time (UT)	P [h]	Method	Reference
May 2, 2000	2.8 3.2 5.1	R-band photometry of the inner coma	Farnham (2001), Farnham (priv. comm.) ^a
April 3, 2006	≥ 3.8	R-band photometry of the inner coma	Waniak (priv. comm.) ^b
April 10, 2006	3.2 ± 0.2	HST bare-nucleus equivalent photometry	Toth et al. (2006), Toth et al. (priv. comm.) ^c
May 7, 2006	8.8 ± 0.3 13.2 ± 0.3 27.2 ± 0.3	Dust and CN coma morphology	Storm et al. (2006)
May 12, 2006	> 7	Doppler broadening of radar signal	Nolan et al. (2006), Nolan et al. (priv. comm.)

^aSingle-peak solutions; amplitude of 0.3 mag; aperture radius of $3''$.

^bAmplitude of 0.03 mag; aperture radius of $6''$.

^cDouble-peak solution; amplitude of 0.6 mag.

data set. On the other hand, in Section 2.7.3.3 we show, that the noise-induced solutions occur preferentially at the highest frequencies, which is an argument supporting the longer rotation periods.

It is clear that we cannot choose the correct rotation period based on our observations alone. So far, a wide range of rotation periods was proposed for SW3-C, which we list in Table 2.5. We note, that the middle value from Storm et al. (2006), which is 13.2 ± 0.3 h, is similar to our solution A. However, it is the fourth multiple in the system, so we consider this solution as unlikely, for the reasons given earlier in this section.

Furthermore, the rotation period of 3.2 ± 0.2 h, originally inferred by Toth et al. (2006) yet later refined by Toth et al. (priv. comm.), is consistent with our three shortest-period solutions (i.e. F, G, and H – see Table 2.3). These solutions are plausible, and they are supported by several other arguments presented in the previous paragraphs. Assuming that the rotation period by Toth et al. (priv. comm.) and any of the three shortest-period solutions were indeed correct at their epochs, we derive in Section 2.7.3.2 additional interesting properties of SW3-C. We show there, that the fraction of the total outgassing, which was effectively accelerating or decelerating the rotation, was below 0.23%. This is much lower comparing to comet Tempel 1, which we attribute to the exceptionally large active fraction of the nucleus of SW3-C (see Section 2.4.3). Moreover, we estimated, that the rotation frequency did not change during our campaign by more than 0.0063 h^{-1} , which validates our approximation of the constant rotation period for the three shortest-period solutions, and excludes the other ones from our list.

Overall, despite the disagreement with some period estimations, we suggest that the rotation period of comet SW3-C during our campaign was between 3.0 and 3.4 h, and that it was fairly constant. That means that SW3-C is most probably the fastest rotator among the cometary nuclei identified to date (cf. e.g. Samarasinha et al. 2004). We

cannot, however, choose between $P = 3.392$ h, 3.349 h, and 3.019 h (solutions F, G, and H respectively) as we find them equally likely.

The arguments supporting fast and firm rotation of SW3-C cautiously suggest that originally the comet had been fragmented due to large centrifugal force. Furthermore, it is entirely possible that the mother comet had been rotating even faster shortly before the splitting than did SW3-C during our campaign. That is because a fraction of the total angular momentum was taken away by the smaller fragments during the break-up, and it is likely that SW3-C is slowly spinning down since then (otherwise it should have broken-up again), which is, however, unimportant in the time scales comparable to the duration of our campaign. The hypothesis of a slow spin-down may be additionally supported if the shortest period from those found by Farnham (priv. comm.) for the half-way epoch, $P = 2.8$ h, is the correct one, and if the intermediate period by Storm et al. (2006) can be explained as a fourth multiple of the real period. In such a case, our solution F (base of the system), which we found at $P = 3.392$ h, being the one consistent with most of the other determinations, should be considered as the most likely at our epoch. But at the moment this is nothing but our speculation, since we cannot be sure about the rotation period of the mother comet 10 years before, and we have no information about its properties, such as bulk tensile strength and density, and shape, which would enable us to calculate the critical rotation period for such body (Davidsson 1999, 2001).

On the other hand, the fact that SW3-C was stable against the rotational disruption is very informative concerning its properties. Using the model of Davidsson (2001), and taking the suggested effective radius of 0.5 km (see Section 2.1) and the bulk density of 600 kg m^{-3} (as found for comet Tempel 1; cf. A'Hearn et al. 2005) along with the rotation period of 3.392 h (solution F) and the minimum axis ratio of 1.8 (Toth et al. 2006) as one extreme, we calculated that the bulk tensile strength of SW3-C must be of at least 14 Pa. On the other extreme, taking the rotation period of 3.019 h (solution H) and the actual axis ratio of 3 , tentatively suggested by Toth et al. (2006), we obtained the required bulk tensile strength of at least 45 Pa. Both results are in agreement with the value of 50 Pa, which was found by Belton et al. (2005) as likely for a cometary nucleus upon surveying studies of tidally disrupted comets, those which are stable against rotational disruption, and theoretical calculations.

2.6 Summary and conclusions

Comet SW3 was observed from the SMT between May 1 and 22, 2006. Here we focus on the observations of HCN from five nights with good observing conditions.

Using the night-averaged spectra we found clear evolution of the line position with phase angle, which is characteristic for solar-stimulated activity. The same spectra provided us with the model-dependent coma expansion velocity of $0.8 \pm 0.1 \text{ km s}^{-1}$, which is typical for a comet at this heliocentric distance. The average model-dependent production rate at $r = 1$ AU was $(2.70 \pm 0.09) \times 10^{25} \text{ molec s}^{-1}$ (with about 20% of absolute uncertainty), showing that the surface of SW3-C was exceptionally active. The calculated production rate is similar to the corresponding results obtained by other authors, although some discrepancies are present. In this work we do not address the problem of these discrepancies, because such study would be premature at the moment, keeping in mind that

the results from several other (sub-) millimeter, IR, and optical campaigns have not been published yet. When they are eventually available, several interesting questions may be potentially answered. Particularly, what is the real slope of the long-term evolution of the HCN production rate for this comet? Is HCN the only important parent of CN? Are the IR results consistent with the (sub-) millimeter ones? And if not, what is the underlying reason for this discrepancy?

We have shown that for several physical reasons parent molecules are very good candidates to be used for tracing rotation of active comets. Indeed, we found a strong (about a factor of 2) short-term variability of the HCN production, significantly exceeding the observing noise. It is most likely associated with the rotation of the nucleus of SW3-C. This means that great care must be taken when interpreting production rates from short observing sessions of parent molecules within the inner coma (cf. the day-to-day variability of SW3 noticed by Dello Russo et al. 2007). Several possible solutions for periodicity are found. Three of them, falling in the range 3.0–3.4 h, are consistent with the determination by Toth et al. (priv. comm.), and we consider them as the most realistic from our list. The apparent firmness of the rotation period suggests that only a very small fraction of the total outgassing, perhaps 0.2% or less, was effectively accelerating or decelerating the nucleus rotation. This contrasts with the significantly higher efficiency of this process in comet Tempel 1, which is plausibly explained by the much larger active fraction of the nucleus of comet SW3-C. The period of 3.0–3.4 h is unusually short for a cometary nucleus, tentatively suggesting too fast rotation as the reason of original splitting. However, since we cannot trace the spin evolution of SW3-C back to the moment of break-up, and a reliable threshold for rotational disruption of the mother comet cannot be calculated, our result cannot be considered as a solid proof of this scenario. On the other hand, the observed stability of SW3-C against rotational disruption is informative concerning the bulk tensile strength of the nucleus, which we found to be of at least 14–45 Pa.

The rotation period of a comet shortly before it splits apart would indicate the reason of break-up much better than the period determined post-factum. Therefore, following Drahus & Waniak (2006), we postulate monitoring of the spin state of possibly large number of active comets, which may spin-up or -down due to torques induced by non-radial outgassing. It is then only a question of time when a prediction of rotational break-up will become possible for a certain object, giving us a definite test for this concept.

We demonstrated that such research can be done by applying a standard periodicity analysis to a time series of parent molecule production rates, calculated from the inner coma in a standard way. Indeed, it is probably the most natural “language” for studying the rotation of active comets, as it automatically provides good estimations for some parameters of outgassing, such as the production rate and sublimation velocity, which are essential for constraining physical models of the accelerating spin of the nucleus.

2.7 Supplementary discussion

2.7.1 Validation of the model and parameters

Here we estimate the uncertainty of the conversion of the line area $\int T_{\text{mB}} d\nu$ into the corresponding production rate Q , introduced by the simplifying assumptions of our model

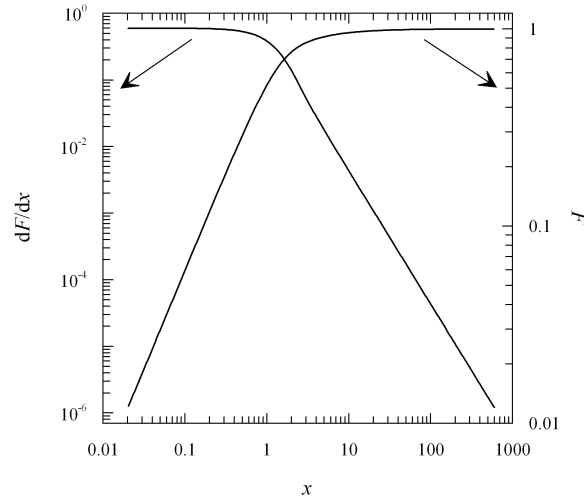


Figure 2.11: Flux in the model coma as observed by our model beam. The left vertical scale concerns the relative flux contribution dF/dx , generated in a shell of a unit thickness and the nucleocentric radius x . The right vertical scale concerns the cumulated relative flux F , produced in a sphere with the nucleocentric radius x . The x quantity is a relative length, measured in units of the beam radius at half-power.

and by the uncertainties of the adopted model parameters (Section 2.4.1). We performed the calculations using the values calculated or assumed in Sections 2.4.1 and 2.4.2, i.e., $\langle Q_0 \rangle = 2.70 \times 10^{25} \text{ molec s}^{-1}$, $T = 80 \text{ K}$, and $v_{\text{exp}} = 0.8 \text{ km s}^{-1}$. Whenever the water production rate was needed, we used $1.2 \times 10^{28} \text{ molec s}^{-1}$, which we consider as a mean-diurnal value during our campaign. It is based on the result by Schleicher (2006), who estimated the production of water from his optical observations of OH, yet we scaled his result to $r = 1 \text{ AU}$ through a power law with an exponent of -4 (we consider it as a “textbook” value; cf. Section 2.4.3). This is consistent with the results from Villanueva et al. (2006) and Dello Russo et al. (2007), based on direct observations of H_2O in IR, which are scattered around the adopted value when normalized in the same way (marginally or not important for the latter). (Note, that the IR-based production rates are likely to be snapshot values whereas the OH-based result is presumably a mean-diurnal production rate; cf. Sections 2.5.1 and 2.6.)

First, working with the model itself, we investigated how much flux is contributed to our observations by the molecules at different nucleocentric distances ρ . Such dependence is entirely controlled by the beam pattern: in our model the total number of molecules in a thin shell centered at the nucleus is independent of the shell radius (if the thickness is fixed), and also the light emission properties of the molecules are identical throughout the coma. We also calculated cumulative flux contributions from the nucleocentric distances below a certain radius. Both profiles are presented in Fig. 2.11. In the final step, with the aid of these profiles, we investigated the effects introduced individually by each of the assumptions, along with the input parameters, which we present in the following sections.

2.7.1.1 Was the coma optically thin?

Let us consider an optical depth $\tau = 0.25$ as small enough to validate treatment of the coma as optically thin. Then, assuming for a moment the coma to be completely stationary, this criterion is satisfied at $\rho \geq 100$ km for the $J(3-2)$ transition and at $\rho \geq 150$ km for the $J(4-3)$ one. However, Fig. 2.11 shows, that even in the extreme case (May 10, 2006), when the size of the beam was smallest (see Table 2.1), and the optical depth largest, merely 13% of the molecules were within the optically thick regime.

In fact the cometary coma is not stationary but it expands rapidly. Therefore, molecules along a column have different velocity components along the line of sight, and due to different Doppler shifts, the emissions from the molecules are slightly misaligned in frequency. For this reason, the optical depth along a column of an expanding coma is smaller than for a static coma with the same number density – hence the net impact on our derivations is $\ll 13\%$.

2.7.1.2 Were LTE conditions present throughout the coma?

We convolved the model flux contributions (Fig. 2.11) with the nucleocentric profiles of the non-LTE to LTE occupancy ratios of the $J = 3$ and $J = 4$ rotational levels. We found that the determined production rates are overestimated by 6.5–13.5% (depending mostly on the beam size). We adopted the non-LTE distribution of the rotational levels from Bockelée-Morvan et al. (2004a), yet we scaled the nucleocentric distance to keep the water density profile consistent with SW3-C, which was an order of magnitude less productive than assumed in their model. Although the adopted distribution was calculated for the (constant) kinetic temperature of 50 K, this inconsistency is probably negligible.

The analysis shows, that determination of the production rates assuming the Boltzmann distribution of the energy levels was justifiable in our case; by no means, however, this fact can be identified with the LTE conditions present throughout the observed coma, which we do not address here.

2.7.1.3 Was the photodissociation process negligible?

A convolution of the model flux contributions (Fig. 2.11) with an exponential decay of HCN gives 2.5–4.5% underestimation of the determined production rates (depending on the beam size). We used for this test the quiet-Sun HCN photodissociation rate of $1.26 \times 10^{-5} \text{ s}^{-1}$ (Huebner et al. 1992). The error introduced by this assumption is very small because the comet approached the Earth so closely that we observed the inner coma only (half-power radius of the beam was about 1000 km). The photodissociation process, however, starts playing an important role at much larger nucleocentric distances, since the characteristic photodissociation scale-length for HCN is about 60 000 km.

2.7.1.4 Were the molecules isotropically ejected from the nucleus?

Comet SW3-C was sublimating preferentially in (roughly) the Sunward direction, which is perfectly clear from the evolution of the line position with phase angle, visible in the night-averaged spectra (Section 2.3). Isotropic outgassing is additionally refuted by the single-peak shape of the night-averaged spectra, as isotropic models, such as ours, predict

an obvious central dip when the coma is larger than the beam. Anisotropic, pro-solar outgassing, is perfectly understandable, since it is the Sun that controls the temperature distribution over the nucleus. Therefore, there is no question whether or not the molecules were isotropically ejected from the nucleus, but how important violation of this assumption is, while determining the production rate using our model.

Let us first consider separately an impact of an anisotropic outgassing on the derived production rates at two extreme geometries: a sublimation restricted to the plane perpendicular to the line of sight, and restricted to the plane parallel to the line of sight, where both planes cross the nucleus. For simplicity we assume here that outgassing is constant in time. In the former situation, there is no influence on the calculated production rates, i.e. the total flux observed by the beam leads to an unambiguous retrieval of this quantity regardless of the angular profile of the local sublimation rates (that may not be constant over the nucleus surface due to e.g. its dependence on an insolation angle). However, the latter scenario permits either an excess or a deficit of the observed flux with respect to the isotropic sublimation (at the same global rate), depending on a preferred direction of outgassing. An excess of the flux appears when the molecules are preferentially ejected along the line of sight, thus many of them (i.e. more than for an isotropic sublimation) accumulate in the beam for a long time. On the other hand, if the molecules are preferentially ejected in a direction perpendicular to the line of sight, many of them leave the beam rapidly, resulting in a deficit of the observed flux. In consequence, the calculated production rate is respectively over- and underestimated, if a model assuming an isotropic sublimation is used for the retrieval. Considering a comet whose nucleus is a uniformly volatile plain sphere whose outgassing is entirely controlled by the zenith angle of the Sun, it is intuitively clear that the largest underestimation of the production rate should be expected when the comet is at the phase angle $\phi = 90^\circ$, whereas the highest overestimation should occur at $\phi = 0^\circ$ and 180° .

This agrees with our quantitative analysis which is presented in Fig. 2.12. It was obtained in the frame of our model, generalized however for a moment to account for an anisotropy of the outgassing. As the activation function we used $\cos^\gamma z$, where z is local zenith angle, and $\gamma = 1$ (though we also show the results for $\gamma = 0.5$ and $\gamma = 2$ for comparison). If $\gamma = 0$ is used, the model reduces itself to the standard isotropic version. For simplicity we assumed that the molecules are ejected in the direction strictly perpendicular to the nucleus surface. Although this formally implies no collisions and $T = 0$ K (in a thermodynamical sense), such “artifacts” of the model are not very important while investigating the influence of geometric projections. The obtained result is very general, e.g. independent of the beam size and pattern, as long as the other assumptions of our model are satisfied (e.g. negligible photodissociation).

Unfortunately, it is very difficult to model an anisotropic outgassing in a realistic, time-dependent way (cf. Section 2.7.1.5), thus the isotropic model of Haser (1957) is the choice of almost every author (see e.g. A’Hearn et al. 1995, Bockelée-Morvan et al. 2004a). We followed this approach – even though it is not very realistic – for the obvious reason of simplicity, and also to keep the basic consistence with most of the other published results (note, that the photodissociation process, naturally tackled by the Haser model, is negligible in our case – see Section 2.7.1.3). For our observations of comet SW3-C, which was around $\phi = 90^\circ$ in that time (see Table 2.1), this may result in about 20% systematic underestimation of the production rates (see Fig. 2.12). In spite of this,

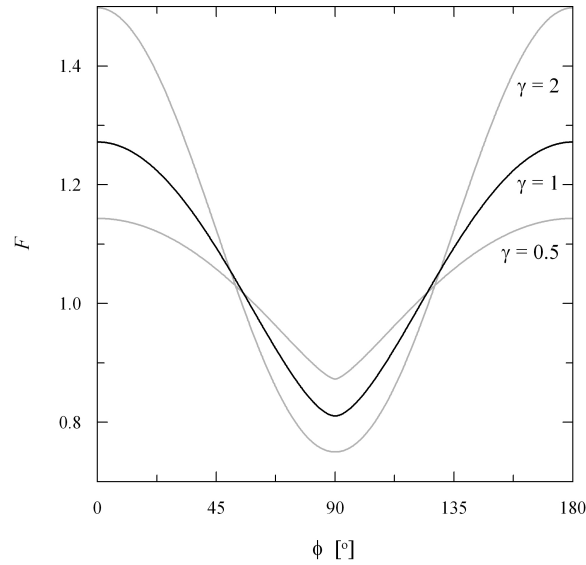


Figure 2.12: Dependence of the relative model flux F on phase angle ϕ for different exponents γ (see text).

the self-consistence of the values should be practically unaffected, thanks to the fairly constant phase angle, which varied only $\pm 15^\circ$ around the minimum of this dependence (see Table 2.1).

2.7.1.5 Was the production rate constant in time?

We analyze the heliocentric evolution (Section 2.4) and the short-term variability (Section 2.5) of the HCN production, although we had determined the rates under the assumption that they are constant. This assumption, which greatly simplifies our model making it time-independent, is however well satisfied in both cases, considering each process as a sequence of isolated states, such as the production is constant within each particular state, yet it varies from state to state.

The characteristic time scale for this problem, calculated in the frame of our model, is only about 45 min, and after this time most of the molecules (73–87% depending on the beam size) would have gone outside the beam (encircled by its radius at half-power). This is a clear advantage of the exceptionally close approach of SW3 to the Earth (see Table 2.1), making our beam unusually small at the comet distance. Provided the production rate evolved on a time scale significantly longer than 45 min, and bearing in mind that the individual exposures (4–5 min) never exceeded this characteristic time scale, the obtained single spectra can be indeed considered as snapshots of a steady-state coma.

Obviously the heliocentric evolution of the production rate happens on a time scale much longer than 45 min (Section 2.4.2). However, is the same argumentation valid to justify our analysis of the short-term variation (Section 2.5.3)?

First of all, a rotation phase profile of the production rate which one observes may be noticeably different from the outgassing pattern intrinsic to the nucleus surface (cf. Biver et al. 2007). Generally, it is shifted in phase, its amplitude is decreased and shape deformed, which is caused by non-zero beam size and non-zero exposure, that imply

collecting the flux from molecules released at different moments of time – thus different rotation phases or even cycles. Most importantly, however, the periodicity of the observed phase profile remains unchanged thus can be directly linked with the rotation period of the nucleus. The faster the molecules leave the beam, and the slower the nucleus rotates, and finally the shorter the individual exposures are, the closer the observed phase profile is to the intrinsic one. However, to determine only the rotation period correctly, it is already sufficient to satisfy all the three aforementioned conditions to be constant in time at any values. In such a case, a physical interpretation of the phase profile (e.g. locating and comparing sources of activity) may be done only upon decomposition of the intrinsic outgassing pattern from the observed one. But even then, or if we deal with a truly intrinsic phase profile, such an interpretation may still be problematic. That is because the phase profile is entirely controlled by superposition of instantaneous ejections from the active regions at a given rotation phase, so we can barely resolve the individual sources at similar nucleocentric longitudes as well as those the insolation over which does not change noticeably over the rotation cycle (though in both cases they can be isolated by modeling the spectral line shape and/or by imaging). Therefore, while investigating a phase profile of the production rate, one should rather refer to the *effective* active sources.

We are convinced that the discussed effects of *flux processing* do not affect our observations significantly, and hence the observed phase profile is close to the *effective* intrinsic activity pattern of the nucleus; regardless of the slightly varying exposure and the noticeably varying beam size. That is because both the characteristic time scale for a significant loss of the molecules from the beam and the individual exposures were shorter than a time scale of any clear feature stimulated by the nucleus rotation (see Fig. 2.10). Interestingly, this justification applies to all the eight phase profiles, because those which are highly structured are found at low frequencies, and the complexity decreases fairly linearly with the increasing frequency.

Note also a comparison of properties of the phase profiles for parent coma vs. daughters and dust presented in Section 2.5.1.

2.7.1.6 Were the expansion velocity and the temperature of the molecules constant in space and time? Were they equal to the adopted values?

Let us restrict this analysis to the nucleocentric distances $\rho = 200\text{--}5000$ km, where about 80% of the model flux contribution comes from. For a comet at $r = 1$ AU with the production rate of water as estimated for SW3-C, indeed, in this range the nucleocentric profile of the outflow velocity should be practically constant at about 0.9 km s^{-1} (see e.g. Bockelée-Morvan & Crovisier 1987). This is very close to the value of $0.8 \pm 0.1 \text{ km s}^{-1}$, which we derived from the line widths in the night-averaged spectra (see Section 2.4.1), and which is consistent with the determinations for other comets around the same heliocentric distance (cf. e.g. Biver et al. 1999, 2002a).

However, we are conscious that this result may be affected by several simplifications of our model. Particularly, if most of the outgassing goes permanently in one direction, the corresponding spectral line may be very narrow regardless of the outflow velocity, and thus may result in significant underestimation of the velocity if a model assuming an isotropic sublimation (such as ours) is used for fitting the line width. For a rotating nucleus with discrete active source(s), the situation may be improved by the *flux processing* (see

Section 2.7.1.5), which somehow simulates isotropization of coma. That is because such a narrow line would be drifting in frequency as the gas radial velocity changes over the rotation cycle, and hence the *processed* line would be broader. Our night-averaged spectra are definitely subjected to this *processing* due to their long effective exposures, however, it is not likely to significantly isotropize the coma as we did not find any hint of the line position variability due to the nucleus rotation (see Section 2.5.1). Since the observations were obtained at fairly “frozen” geometric circumstances (see Table 2.1), the Sunward anisotropy (cf. Sections 2.3) remains unfortunately unchanged by the *processing*. As we concluded in Section 2.7.1.4, it is very difficult to model an anisotropic outgassing in a realistic way, therefore we determined the expansion velocity in a standard manner which is easy to implement and which ensures basic consistence with most of the other published results.

The model by Bockelée-Morvan & Crovisier (1987) also suggests, that the kinetic temperature of the parent coma has a nearly constant nucleocentric profile at about 15 K in our case. The very low model temperature is a direct result of the cooling process induced by the adiabatic expansion of gas, with only very weak heating by highly energetic photodissociation products, whose number was simply too low for comet SW3-C to efficiently drive the process. However, e.g. Lis et al. (1997) determined a (rotational) temperature equal to 73 K for comet Hyakutake at very similar geo- and heliocentric distances, and using similar observing facility (beam radius 400–800 km depending on the transition frequency), whereas the same model suggests $T < 40$ K already accounting for the 10 times higher productivity of that comet. This suggests that the temperature yield by this model should be considered as a robust lower limit for the mean gas temperature within our beam.

Additional constraints on the inquired HCN temperature come from IR observations of SW3-C (Table 2.6). As expected, the temperature was rising with the decreasing heliocentric distance and size of the sampled coma. Unfortunately, the helio- and nucleocentric dependencies cannot be separated, nor is any of these measurements anyhow compatible with our beam size. However, since the temperatures by Dello Russo et al. (2007) were determined at very similar heliocentric distances, our best guess is that they are at the high end of what is reasonable to expect for our observations of SW3-C. We realize that they were sensitive only to the high-temperature region close to the nucleus, whereas our beam sampled the more distant colder gas too; however, the warmer gas, heated by collisions with the photodissociation products further from the nucleus, should also contribute to our beam if the process was efficient (see the characteristic nucleocentric scalengths for the adiabatic cooling and the photolytic heating in e.g. Bockelée-Morvan & Crovisier 1987). Temperature determinations from other molecules and for fragment B (also reported by other authors), although instructive, unfortunately do not remove the ambiguity of this discussion.

Last but not least, the ratio of the $J(4-3)$ to the $J(3-2)$ line areas $\int T_{\text{mB}} dv$ is also suggestive about the temperature, although it cannot be used to measure it directly. One problem is that we did not observed both lines simultaneously, hence their ratio is influenced by the nucleus rotation if different rotation phases were sampled on different nights (cf. Section 2.5), and, at smaller extent, by the little change in observing geometry (see Table 2.1). Another problem is that the beam size was different for each of the observed transitions (cf. Table 2.1), hence the line ratio is influenced by the nucleocentric tempera-

Table 2.6: List of published HCN rotational temperatures T_{rot} based on IR spectroscopic observations of SW3-C.

Date UT (2006)	r [AU]	Coma extract [km \times km]	T_{rot} [K]	Reference
April 7	1.270	101 \times 420	52^{+15}_{-10}	Villanueva et al. (2006)
April 16	1.194	75 \times 312	53^{+18}_{-10}	Villanueva et al. (2006)
May 14	1.000	25 \times 102	77 ± 2	Dello Russo et al. (2007)
May 15	0.995	26 \times 105	88 ± 3	Dello Russo et al. (2007)

ture profile (see before), and also because of a possible drop of the main-beam efficiency at the higher frequency (though undetected – see Section 2.2). Nevertheless, using the night-averaged spectra from May 10 and 11, 2006 (see Fig. 2.5), we computed the ratio of 1.34 ± 0.05 , which suggests the temperature of only 30 ± 2 K (see Fig. 2.13). Taking however the aforementioned effects into account it is clear that this estimation should be considered as another lower limit on the temperature.

Taking all the arguments into account we eventually adopted $T = 80$ K, which may be, however, slightly overestimated.

Nevertheless, for both monitored transitions we checked with our model how the line area $\int T_{\text{mB}} dv$ depends on the temperature, and the result is presented in Fig. 2.13. It shows, that if for example we took the temperature as low as 45 K, the production rate obtained from the $J(3-2)$ transition would be 38% lower, and 14% lower from the $J(4-3)$ one. Therefore, if the temperature were lower than adopted, then the production rates we report in this work would be a bit overestimated, and the heliocentric dependence would be overly steep (Section 2.4.2). On the other hand, an influence of the uncertainty on the temperature is too weak to affect our periodicity analysis (Section 2.5), which is fairly stable against much larger changes of the heliocentric reduction (see Section 2.7.3.4).

The fact that the temperature probably varies noticeably with the nucleocentric distance (cf. the profiles in Bockelée-Morvan & Crovisier 1987, for higher production rates), and with a direction (cf. analysis of this effect for the production rate in Section 2.7.1.4) are not issues here, since its constant value is a model concept only, aimed at optimum retrieval of the production rates. Therefore it should be considered as an effective temperature for a given beam rather than a precisely defined thermodynamical property of the coma. The expansion velocity is less sensitive to these effects, which are practically negligible comparing to the problems discussed in the second paragraph of this section.

The heliocentric evolution of the coma expansion velocity and of the temperature must be practically negligible on the time scale of our campaign, which is due to an excellent stability of the observing geometry (see Table 2.1). Similarly, we ensured that the uncertainty about the temperature is negligible for the determination of the expansion velocity.

Last but not least, we acknowledge that in this discussion we consider the rotational temperature to be the same as the kinetic temperature – hence we directly compare the observational measurements of the former with the model predictions for the latter. However, this identity is true only under LTE, which was not necessarily well satisfied in our case (see Section 2.7.1.2).

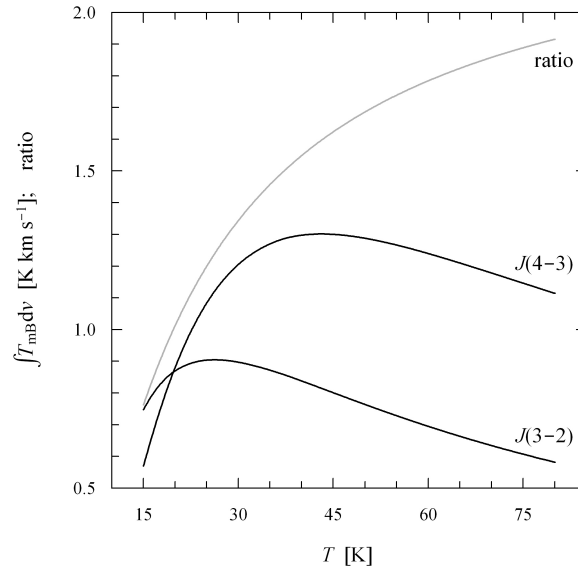


Figure 2.13: Dependence of the line area $\int T_{\text{mB}} dv$ on the coma temperature T (assumed to be constant) for both considered transitions (black lines). It was derived with our model for the HCN production rate $Q = 2.7 \times 10^{25} \text{ molec s}^{-1}$, the geocentric distance $\Delta = 0.1 \text{ AU}$, and the beam properties of the SMT (Section 2.2). The line ratio is shown by the gray line.

Considering the determined production rates as *isotropic*, it is clear that all the other model assumptions do not affect them significantly. The stability of our instrument was about 20% (Section 2.2), and the statistical error of an individual measurement is also 20% on average. Furthermore, the estimated deficit of our production rates resulting from the assumptions discussed in Sections 2.7.1.1 and 2.7.1.3 cancels at some extent the excess resulting from the assumption discussed in Section 2.7.1.2 and from the adopted coma temperature discussed in Section 2.7.1.6. Thus, the overall systematic error introduced by the deviation of our model from reality should be lower than 20%, and the self-consistence of our production rates much better, justifying the use of this simple approach.

2.7.2 Validation of the heliocentric correction (contributed by Michael Küppers)

The heliocentric evolution of the production rate is superimposed with the short-term variability due to the rotation of cometary nucleus. The determined heliocentric dependance may be different from the real one if the rotation phase of the nucleus is sampled irregularly. To evaluate the uncertainty introduced by this effect on our mean-diurnal HCN production rate at $r = 1 \text{ AU}$, and on its heliocentric evolution, we assumed a simple sinusoidal rotation phase profile, superimposed with a power-law dependance on a heliocentric distance. Then the production rate Q at the time t and the heliocentric distance r is given by:

$$Q = \left(1 + \frac{A-1}{A+1} \sin(2\pi(t-t_0)f)\right) Q_0(r/r_0)^n, \quad (2.3)$$

where Q_0 is a mean-diurnal production rate at $r = r_0 = 1$ AU, n is an exponent of the power-law heliocentric dependence, A is the ratio between maximum and minimum production rate during one rotation cycle, f is the rotation frequency, and t_0 is a moment of the zero rotation phase.

We used $A = 2$, as typically found in our analysis (see Section 2.5.3), and $n = -8.2$ as obtained for our data (see Section 2.4.2). For the frequency f between 0.02 and 0.8 h⁻¹, and the unknown zero-phase moment t_0 ranging between 0 and 1/ f , we calculated the model production rates according to Eq. (2.3), using the moments of time t of our observations. Then we determined Q_0^* and n^* from a power-law fit to such artificially created data, likewise we did for our HCN measurements (cf. Section 2.4.2).

Generally, the reconstructed quantities Q_0^* and n^* are different from the input ones, Q_0 and n , because the heliocentric reduction cannot take into account the rotation term, that is unknown at that point. We found that the measured Q_0^* tends to be slightly lower than the real Q_0 . Its mean value $\langle Q_0^* \rangle$, calculated from the complete range of the zero-phase moments t_0 , is between 1.3 and 2.9% lower than Q_0 , depending on the frequency f . The standard deviation of Q_0^* around $\langle Q_0^* \rangle$, measuring how strongly the determined Q_0^* depends on the zero-phase moment t_0 at a given frequency f , is found between 0.1 and 17.3%, with the median of only 2.9%. Generally, the error introduced on Q_0^* by the influence of the nucleus rotation is smaller than those from the other error sources, which are discussed in Section 2.7.1.

The mean value of the reconstructed power-law exponent, $\langle n^* \rangle$, is always equal to the real n , regardless of the frequency f . That is because the variations average out when varying t_0 over a full rotation period. The standard deviation σ_{n^*} , as a function of frequency f , is shown in Fig. 2.14. It shows, that it is possible to obtain from our data n^* which is much different from the real n , especially for lower frequencies f , but the discrepancy is very sensitive to the actual f . Moreover, we investigated the probability of obtaining $n^* \geq -4$ (which we consider as a “textbook” exponent; cf. Section 2.4.3), strongly differing from the real $n = -8.2$, and found it to be equal to 2.2%. The same analysis, yet limited to the rotation periods in the range 3.0–3.4 h (as the most likely rotation period of SW3-C – see Section 2.5.4), yielded the probability of 3.6%. On the other hand, if we would have assumed $n = -4$, than the probabilities of deriving $n^* \leq -8.2$ are 2.1% and 3.8% for the overall and restricted ranges respectively.

Interestingly, the discussed functions of the rotation frequency f , such as standard deviations of the reconstructed Q^* and n^* , as well as $\langle Q_0^* \rangle / Q_0$, in fact do not depend on the actual input values of Q_0 and n . But since the distribution of n^* around the assumed n is slightly asymmetric, they cannot be interchanged while calculating probabilities, which is illustrated by our results shown in the previous paragraph.

Summarizing, small possibility exists that the steep instantaneous slope of the heliocentric dependance, derived in Section 2.4.2, is an artifact. However, this is still unlikely to significantly affect the periodicity analysis, as in Section 2.7.3.4 we show, that the presence of the solutions between 3.0 and 3.4 h is stable against such large changes in the assumed heliocentric evolution of the production rate.

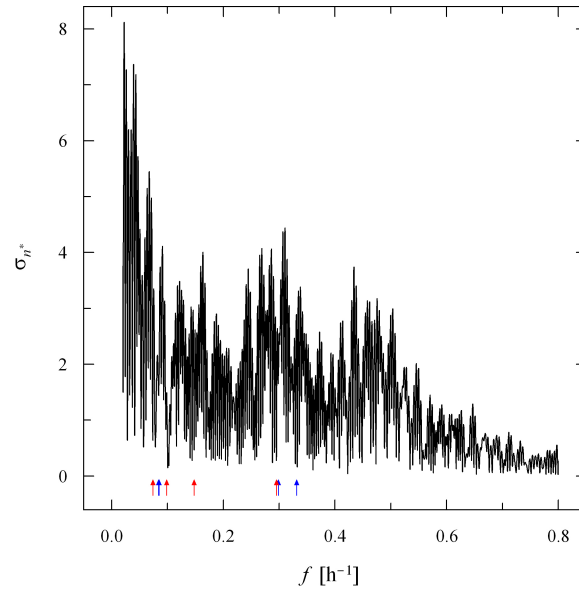


Figure 2.14: Standard deviation among the reconstructed power-law exponents, σ_{n^*} , as a function of the rotation frequency f . The simulated production rates were calculated from Eq. (2.3). Positions of the eight best solutions (Table 2.3) are indicated by the arrows: red for those from the system and blue for the others, though solutions B and C are unresolved.

2.7.3 Validation of the periodicity analysis

The analysis of periodicity presented in Section 2.5.3 is clearly insensitive to the systematic uncertainties of the production rates, introduced by the simplifications of our model, which we extensively discussed in Section 2.7.1. There are, however, several other problems which might have potentially affected the analysis. We discuss them in this section, and present direct tests for the robustness of our results.

2.7.3.1 Seasonal effects?

Following the statistical approach of Drahus & Waniak (2006), who adopted the routine of Michałowski (1988), we investigated the extent at which the orbital motion of the comet might have affected the observed periodic variability of the HCN production rate driven by the nucleus rotation (cf. Section 2.5.3). The results are summarized in Table 2.7. They show, that one may expect to observe shifts of the rotation phase, but they are relatively small comparing to the scatter of the individual data points. Furthermore, since such phase shifts increase roughly linearly with time, they are well compensated by a (very small) adjustment of the rotation period, which is then called synodic (in contrast to the “real” one, so-called sidereal). Small phase shifts additionally suggest that the amplitude and shape of the phase profile was also stable during our observations.

2.7.3.2 Angular acceleration and/or complex rotation of the nucleus?

Small yet active cometary nuclei are subjected to rapid changes of their rotation periods (see Section 2.5.2). The effect is produced by torques which appear as a result of the outgassing at non-radial directions. Even though the torques may be small, and may

Table 2.7: Maximum possible phase shifts at given confidence levels, calculated with respect to the mid-point of the first observing run, May 10.4979, 2006 UT. The statistics was constrained from over 1 million spin axis orientations distributed uniformly in space.

Date UT ^a (May 2006)	Confidence level	
	75%	95%
11.6885	0.004	0.009
12.5524	0.008	0.016
20.6222	0.040	0.083
22.4882	0.047	0.100

^aMiddle moment of an individual observing run.

largely cancel out, the effective residual torque is still expected to efficiently drive the process, and consequently, to cause a measurable change in the rotation period and in the spin axis orientation, on a time scale of a single apparition.

Several authors, e.g. Samarasinha et al. (1986), Jewitt (1999), and recently Drahus & Waniak (2006), presented a very similar simple description of this effect. Using the notation of the last authors, an instantaneous rate of change in the rotation frequency df/dt , can be described as:

$$df/dt = \frac{15}{16\pi^2} \frac{v_{\text{subl}} Q_{\text{tot}}}{R^4 \varrho} S, \quad (2.4)$$

where v_{subl} is the gas sublimation velocity, Q_{tot} is the production rate of all gaseous species, R is the effective radius of the nucleus, ϱ is the nucleus bulk density, and S is a dimensionless *scaling factor* which is the fraction of the total outgassing Q_{tot} which effectively accelerates or decelerates the rotation.

Using this equation we estimated the magnitude of angular acceleration for SW3-C during our campaign. The sublimation of gas was characterized with $Q_{\text{tot}} = 1.2 \times 10^{28}$ molec s⁻¹ (the adopted water production rate; see the beginning of Section 2.7.1), and $v_{\text{subl}} = 0.8$ km s⁻¹ (the expansion velocity of the HCN coma; see Section 2.4.1), and the nucleus with $R = 0.5$ km (Toth et al. 2005, 2006, Nolan et al. 2006), and $\varrho = 600$ kg m⁻³ (as found for comet Tempel 1; cf. A'Hearn et al. 2005). The least known parameter is S , which we assumed to be also the same as for Tempel 1. Since the nucleus of the latter was recently discovered to be slowly spinning up (Belton & Drahus 2007), the rate of change in the frequency, measured in the Deep Impact approach photometry at the level of 7×10^{-8} h⁻², suggests $S = 1.5\%$, when linked with the other measured properties through Eq. (2.4). Finally, as the inquired estimation for SW3-C we obtained $df/dt = 1.4 \times 10^{-4}$ h⁻². Though it is a factor of 2000 (!) stronger than measured in comet Tempel 1, it is not a surprise that comet SW3-C should be changing its spin much faster than the six-times-larger nucleus of comet Tempel 1 (cf. A'Hearn et al. 2005), bearing in mind the biquadratic dependence on the radius, and that the comets had comparable production rates during both campaigns (cf. Biver et al. 2007).

Integration of df/dt over the duration time of our campaign yields the expected change of the rotation frequency equal to 0.041 h⁻¹, regardless of the frequency itself. Double integration gives the expected change of the rotation phase, which is equal to 1.51 when referred to the middle moment of the campaign. The latter shows, that the *classical*

approach (see Section 2.5.2) is completely irrelevant in such a case, because the phase shift of the first and last data point is more than one full rotation cycle!

Nevertheless, in spite of this expectation, an argument suggesting a fairly constant periodicity may also be raised. As we noted in Section 2.5.4, the rotation period of 3.2 ± 0.2 h, obtained by Toth et al. (priv. comm.) for April 10, 2006, is similar to our three shortest-period solutions (i.e. F, G, and H – see Table 2.3). If both their result and any of these three solutions are indeed correct at their epochs, then the corresponding change of the rotation period between these two campaigns does not exceed 0.2 h. This corresponds to $df/dt \approx \pm 2.2 \times 10^{-5} \text{ h}^{-2}$, and consequently, yields the *scaling factor* of approximately $S \approx \pm 0.23\%$; which is a factor of 6.5 lower than for comet Tempel 1, and hence the net torque in SW3-C was much less efficient. This may result from the exceptionally large active fraction of the nucleus of SW3-C, which was about a factor of 20 more volatile than the nucleus of comet Tempel 1 (see Section 2.4.3 and especially Fig. 2.8). Jewitt (1999) shows, that the *scaling factor* (which he calls a *dimensionless moment arm* and denotes as k_T) is inversely proportional to the square-root of the number of active sources randomly distributed in azimuth. If therefore we interpret the difference in the surface volatility as a difference in the number of active sources, we will obtain the *scaling factor* ratio of both comets of approximately 4.5, which is comparable to what we derived before taking simplism of our argumentation into account.

This result should be now confronted with the duration of our campaign. The change of the rotation frequency is implied to be equal to $\pm 0.0063 \text{ h}^{-1}$, and the change of the rotation phase equal to 0.23 when referred to the middle moment of the campaign. To satisfy the latter we need to assume that if the rotation period were not constant, the frequencies of the considered solutions (determined in the *classical* way) would correspond to the middle time of the campaign – which is, however, very likely, since the time arrangement of our data is rather symmetric, and the quality does not change too much with time. Normally, such phase shifts should visibly decrease the quality of the phase profile. But our observations cluster at the beginning and at the end of the campaign, therefore the phase shifts are fairly constant within each group (although formally proportional to the square of time), thus they are well compensated by a (very small) adjustment of the rotation period. The residual phase shifts are then insufficient to affect the obtained periodicities, and introduce only some small and “safe” excess scatter.

Note, that the low efficiency of the accelerating torque, and consequently, the small changes of the rotation parameters during our campaign, are still the upper limits. That is because any other rotation period, within the uncertainty range of the result by Toth et al. (priv. comm.), would be even closer to one of the three shortest-period solutions from our list – thus being in support of it and suggesting slower changes of the rotation period. At the same time the increased difference with respect to the other solutions would make them unlikely. That is because faster changes of the rotation period would be required, which would consequently make their reality (as detected in the *classical* way) questionable, though we acknowledge that in such case the *scaling factor* would be closer to its theoretically-predicted value. An indication towards one of our three shortest-period solutions would also fix the sign of the period changes: currently we find the spin-up and the spin-down scenarios equally possible as the rotation period by Toth et al. (priv. comm.) is almost exactly between the extreme solutions H and F.

The possibility that the considered periodicities are affected or even completely gener-

ated by complex rotation instead of simple is also very unlikely. In such case the periods of rotation and precession must have been very close to a resonance, yielding probably a much longer apparent periodicity in our analysis. Only the 1:1 resonance would enable detection of the true period, although not distinguished as complex with our methods. But it is difficult to imagine a reason for such a (or even any) resonance, and even harder a comet rotating with the period much shorter than 3 h – as stability of the nucleus is then problematic (cf. e.g. Davidsson 1999, 2001). On the other hand, if obliquity of the instantaneous spin axis to the constant total angular momentum vector is not large, or if the period of precession is much longer than the duration of our campaign, then the true periodicity can be correctly detected with our methods, and the effect of complex rotation would only increase scatter in the phase profile. Note also, that it was recently postulated, that the characteristic relaxation time scale for small Solar System objects is of the order of only one year (e.g. Efroimsky 2001) rather than the traditional millions of years (e.g. Jewitt 1999), showing that it is the simple rotation that should dominate among these bodies (which seems to be observed – cf. e.g. Samarasinha et al. 2004).

We addressed these problems by analyzing scatter in the considered phase profiles. Taking into account the RMS error of our reduced production rates Q_0 , which is equal to 0.582×10^{25} molec s⁻¹, we derived that Θ would be equal to 0.448 if the data points were scattered as suggested by the RMS. In contrast, the three discussed periodicities are detected at Θ of only 0.641–0.785 (cf. Fig. 2.9), corresponding to 20–32% excess of scatter (though noticeably lower than 49% for the unphased data). Thus, it may indeed hint some small changes of the spin state or the observing geometry (discussed in Section 2.7.3.1), but it may also result from some instrumental effects (see Section 2.2), and/or intrinsically imperfect repeatability of the sublimation pattern. In any case, the detected periodicity should be practically unaffected by these effects.

We conclude, that our analysis, being done within the frame of a constant and simple periodicity approximation, is fully justifiable for the shortest-period solutions (i.e. F, G, and H). All the other solutions may be considered as realistic only if the period found by Toth et al. (priv. comm.) is wrong, and the rotation was sufficiently stable during our campaign. Otherwise, they must be regarded as artifacts, as presence of any of them would require a very rapid evolution of the rotation period, making detection of such a solution strongly problematic, and actually requiring disruption of SW3-C, due to an overly fast rotation, shortly before the HST run, which was not observed.

2.7.3.3 Where does the noise-induced solutions preferentially occur?

Another argument that should be considered in this discussion refers to the statistical properties of the noise-induced solutions (see Sections 2.5.2 and 2.5.3). So far, by analyzing the number N of solutions satisfying the condition $\Theta < \Theta_0$ (which is fairly independent of the frequency f), we showed that all the solutions listed in Table 2.3 are statistically significant (see the confidence levels in Fig. 2.9). Nevertheless, another statistics $N(f_0 < f < f_0 + df)$, indicating at which frequencies the noise-induced (global) solutions preferentially occur, provides an additional constraint on the robustness of our results. We present it in Fig. 2.15.

As might have been expected, most of the noise-induced solutions can be found at high frequencies. This means, that if some of the solutions obtained for our observational

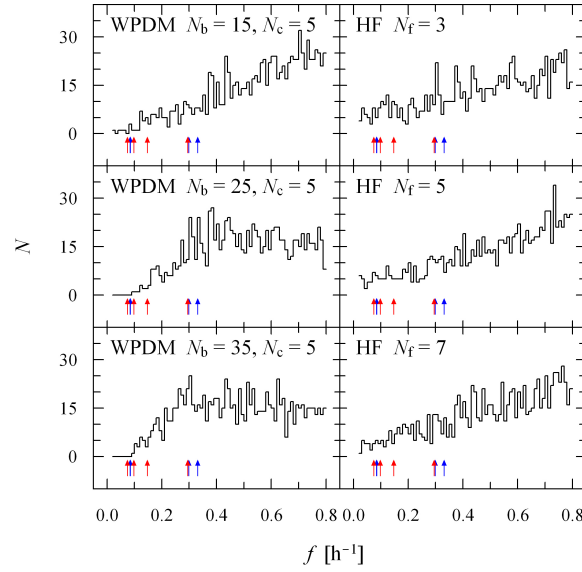


Figure 2.15: Histograms of the noise-induced solutions. Here N indicates a number of simulations (from the total number of 1000) featuring global minima within a 0.01 h^{-1} frequency interval centered at f . Positions of the eight best solutions (Table 2.3) are indicated by the arrows: red for those from the system and blue for the others, though solutions B and C are unresolved.

data were in fact induced by noise, they would be the shortest-period ones rather than the others, which are practically impossible to arise from noise at $f < 0.15 \text{ h}^{-1}$. On the other hand, one should bear in mind that all the solutions we list were found at sufficiently low Θ to be convinced, that their presence is due to real short-term variability of the production rate. Therefore, the matter of the debate is just which of the phasings is the true one, but this ambiguity cannot be resolved with such an analysis.

2.7.3.4 Analysis of two test data sets

We also verified our results by performing the same periodicity analysis as before (cf. Section 2.5.3) for two additional data sets. Data set A is based on the same AOS observations as used previously (cf. Section 2.2), but a different heliocentric trend was subtracted: we used a much shallower power law than before (cf. Section 2.4.2), with an exponent of -4 , which we consider as a “textbook” value (cf. Section 2.4.3). Data set B was constrained from the spectra provided by the facility Forbes Filterbanks (FFB-A and FFB-B), which were working parallel to the AOS spectrometers. They have total bandwidths of about 1 GHz with 1024 channels each (a resolution of 1000 kHz). These spectra were reduced in the same way as were the AOS observations (cf. Section 2.2), and their own power-law heliocentric trend was subtracted (a bit steeper than the one calculated for the AOS observations – cf. Section 2.4.2). We should note that in theory the meaningfulness of data set B should be rather limited, because the observing noise comes mainly from the receiver, thus all the spectrometers should feature the same noise level and even pattern; real life shows, however, that this is not exactly true, because additional sources of noise might have also been present (cf. Section 2.2).

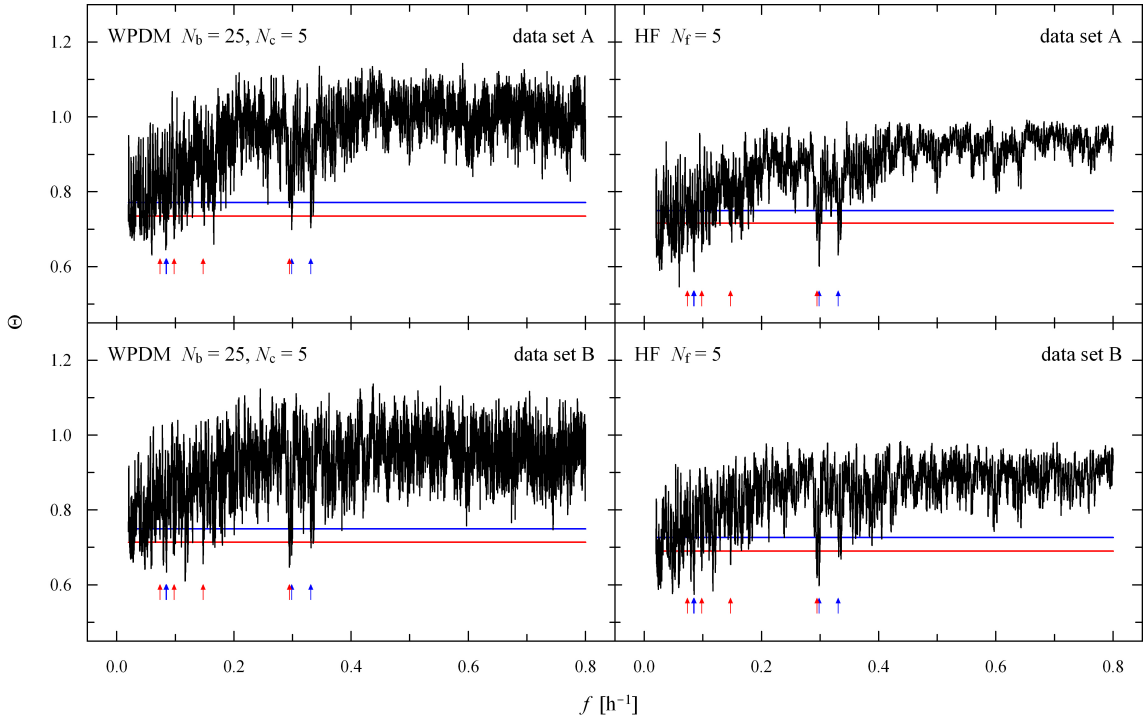


Figure 2.16: Periodograms for our two test data sets calculated with both methods. The horizontal lines indicate the confidence levels of 75% (blue) and 95% (red). Positions of the eight best solutions (Table 2.3) are indicated by the arrows: red for those from the system and blue for the others. Solutions B and C are barely resolved in this figure.

All the solutions we found before are also detected in these two tests, and most of them are again represented by the deepest minima (see Fig. 2.16). However, two additional significant solutions are also present: one at $f = 0.16569 \text{ h}^{-1}$ in the data set A (although it is weakly visible in the presented periodogram for HF with $N_f = 5$, it is already very striking for $N_f = 7$, and appears at nearly the same frequency), and one at $f = 0.11711 \text{ h}^{-1}$ in the data set B. But they neither show-up sharply in the neighboring tests, nor in the original analysis.

The best stability is demonstrated by our shortest-period solutions (i.e. solution F, G, and H – see Table 2.3), which are strong in both test cases. The reason for that is a very simple shape of the corresponding phase profiles, which makes them insensitive to small distortions. In contrast, the solutions at lower frequencies, including those newly found, giving more complicated phase profiles, are more sensitive to the searching routine and settings, heliocentric reduction, noise realization and spectral sampling in a specific spectrometer, as well as geometric and spin instabilities (cf. Sections 2.7.3.1 and 2.7.3.2).

3 Comet 17P/Holmes

3.1 Introduction

On Oct. 23/24, 2007 comet 17P/Holmes underwent a cataclysmic event which consequently raised its optical brightness by a factor of a million, making it an easy object to see with the naked eye (Fig. 3.1). It was the greatest cometary outburst observed to date. Coincidentally, the comet was perfectly placed in the Northern hemisphere, prompting several observing campaigns.

17P/Holmes is a Jupiter-Family comet. It approaches the Sun to 2.05 AU with the orbital period of 6.9 years. Snodgrass et al. (2006) determined the radius of its nucleus to be of 1.62 km, which is in good agreement with the earlier result by Lamy et al. (2000), and which is absolutely typical for a comet (cf. e.g. Lamy et al. 2004).

It was accidentally discovered by Edwin Holmes (London, England), who spotted it on Nov. 6/7, 1892 near the Andromeda Galaxy. It was established later that this happened nearly five months after the perihelion passage. Contemporary observers described the comet as a bright star-like object distinctly visible to the naked eye, and appearing as a uniform disc when seen through a telescope. It was quickly realized that the comet was



Figure 3.1: Comet 17P/Holmes imaged by Jack Newton on Nov. 5.1, 2007 UT in the broad optical range. The inner disc is the dust coma, the outer halo is the daughter coma (dominated in this image by C_2), and the blueish stripes is the ion tail (dominated in this image by CO^+).

discovered thanks to a massive explosion which must have occurred a few days earlier. Furthermore, comet Holmes burst for the second time in mid January, 1893, though it did not reach the brightness level from the first explosion. The very favorable location in the sky made it widely observed, which resulted in rich observing material that is available in literature. After the perihelion passage in 1906 the comet was temporarily lost; it was recovered in 1964 and is observed at every return since then.

The 2007 explosion was first noticed by Juan Antonio Henríquez Santana on Oct. 24.067 UT, and immediately confirmed by many observers world wide (Buzzi et al. 2007). Estimations have placed the onset of the outburst about Oct. 23.8 UT (Hsieh et al. 2007). It occurred nearly six months after the perihelion passage, at the helio- and geocentric distances of 2.4 and 1.7 AU respectively. Early optical images revealed a perfectly circular (presumably spherical) cloud of dust, which was expanding at a fairly constant rate. Additionally, a dusty *blob* was visible in the inner coma, separating slowly from the nucleus, and also expanding itself (see e.g. Snodgrass et al. 2007). Both structures displayed peculiar morphological features. The dust environment was composed of two types of grains: hot – refractory, and cold – icy (Yang et al. 2009). It is not clear however how important was the role of the icy grains in producing the molecular parent coma. It was quickly realized that the dust cloud was embedded in a larger halo of gas; in the best images the size ratio of both environments reached approximately a factor of four around Nov. 1. This coincides with a timid appearance of emission signatures in optical spectra, which were initially showing nothing but dust continuum. Since the strongest emissions are those of daughter radicals (especially C_2 and CN), their gradual and delayed appearance in comet Holmes is perfectly understandable. If the material was ejected in an impulsive event, daughter products needed some time to be photochemically created from their parents; moreover, if a significant fraction of the parents originated from icy grains blown at the outburst, even their appearance would be spread in time, thus amplifying the delay of the daughters. One should also note that photochemical processes at 2.4 AU from the Sun are much slower than at 1 AU (photochemical lifetime $\tau \propto r^2$). For the same reason, even later, that is about one week after the onset, an ion tail started progressively appearing. By the end of November there was, however, again no gas emission signatures visible in optical images. The observed radicals and ions photodissociated into even simpler elements and dispersed in space, and possible alternative sources of parent molecules (such as the grains or the post-outburst nucleus) were apparently incapable of sustaining the daughter coma at the explosive level. This cut-off should not be considered as sharp, since it depends on one's sensitivity to detect the leftovers or the radicals from the (weak) post-outburst activity (cf. Capria et al. 2008). Curiously enough, the characteristics of the recent outburst are strikingly similar to what had happened to the comet 115 years before.

In this chapter we present our results from high-resolution spectroscopic monitoring of comet Holmes at millimeter wavelengths. On many occasions this technique has proven to be a powerful tool for studying the gas environment in comets, thus it is also ideal for characterizing their explosions. Through rotational transitions it allows investigation of the comet's molecular composition. Furthermore, it provides excellent diagnostics of the physical conditions within the observed coma, including spatial density, kinetic temperature, and also gas kinematics as the spectra are velocity-resolved. Worth emphasizing is that our campaign provides the very first observations of the Holmes' parent coma after the outburst (and ever, in fact). At the current stage we do not aim at explaining the



Figure 3.2: The 12-m millimeter-waves telescope on Kitt Peak (Arizona).

physical process(es) which triggered the outburst, and, for the still stronger reason, the two historical events; this would be premature if based on our results only. Instead, we present our observational material, and discuss it in a qualitative way. Our preliminary findings have been already published by Drahos et al. (2007, 2008a,d).

3.2 Observations and data reduction

We traced this event with the telescopes operated by the Arizona Radio Observatory¹. The campaign was divided into two main parts: the immediate monitoring was realized with the 12-m telescope on Kitt Peak² (Fig. 3.2), whereas the Submillimeter Telescope on Mt. Graham (see Fig. 2.2 in Chapter 2) was used for the late follow-up observations. The scientific outcome of the *early* part is far superior with respect to the *late* one, therefore we focus on it in this and the following sections. The second part, a bit ill-fated, is presented separately in Section 3.6.

We could use the 12-m telescope every day between Oct. 25.5 and 31.5, 2007 UT for a few hours. We acknowledge that our observations were accommodated immediately after the outburst was noticed, that means the regularly scheduled programs were interrupted. The geometric circumstances along with the list of observed molecules are given in Table 3.1.

We utilized three dual-polarization single-sideband SIS receivers: *3mmlo* (68–90 GHz), *3mmhi* (90–116 GHz), and *2mm* (130–170 GHz), which all are facility instruments. However, at the time of observing, only one polarization channel was functional at *3mmlo*. All the receivers feature a rejection level of an unwanted sideband better than 20 dB across the entire wavelength range. Spectral analysis was performed using the facility Millime-

¹<http://aro.as.arizona.edu/>

²See technical details at http://aro.as.arizona.edu/12_obs_manual/12m_user_manual.htm.

Table 3.1: Geometric circumstances.

Date UT ^a (Oct. 2007)	r ^b [AU]	Δ ^c [AU]	ϕ ^d [°]	λ ^e [°]	β ^f [°]	Molecules
25.5957	2.4421	1.6333	16.660	67.304	29.235	HCN, CO
26.5373	2.4457	1.6313	16.415	67.172	29.333	CH ₃ OH, CS
27.4990	2.4494	1.6294	16.166	67.031	29.428	CO, H ₂ CO, HCN
28.3765	2.4527	1.6278	15.940	66.897	29.512	HCN
29.3823	2.4566	1.6262	15.682	66.736	29.604	CS
30.3948	2.4605	1.6247	15.423	66.567	29.693	HCN
31.4407	2.4646	1.6234	15.158	66.386	29.780	H ₂ S, HCN

^aMiddle moment of a daily run.^bHeliocentric distance.^cGeocentric distance.^dPhase angle.^eEcliptic longitude.^fEcliptic latitude.

ter Autocorrelator (MAC). Halves of the array of spectral channels were permanently connected to each of the receiver's polarization channel, and provided an identical arrangement of the spectral channels in each of them. This is a particularly nice feature of MAC, which enables co-adding the spectra from both polarizations (which increases the S/N) without the need for re-scaling and/or re-positioning the spectral channels. The instrument was configured to provide the total bandwidth of 150 MHz and a spacing of the spectral channels of 24.4 kHz. The real spectral resolution, defined as the FWHM channel width, is however twice that value, that is 48.8 kHz. This means that neighboring spectral channels are significantly correlated. Nevertheless, for simplicity we considered them as if they were completely independent, and hence as the spectral resolution we simply adopted the channel spacing. The spectra were calibrated in terms of the main-beam brightness temperature T_{mB} following the standard procedures (cf. Chapter 2.2). Additionally, the absolute frequency scale was converted to the relative radial-velocity scale (negative velocities indicate blueshift), and corrected for the radial velocity of the comet with respect to the telescope. In Table 3.2 we list the observed transitions and provide basic instrumental data for the corresponding frequencies.

Position of the comet was continually calculated from the orbital elements provided by the JPL HORIZONS system³ for the epoch of our observations. The spectra were taken in a position-switching mode, with a 0.5° offset for the sky-background determination. At that separation distance the coma influence was presumably negligible, as even the best optical images show the daughter cloud to be smaller than that before the end of our *early monitoring*. Integration times at the off- and on-source positions were always equal, and amounted to 15 or 30 sec. The number of ON–OFF pairs giving birth to one spectrum was 6, 10, or 20; in combination with the integration times this gives the exposures of 6 or 10 min (where half of this time was spent at the offset position). In fact, each spectrum took slightly longer – the extra time was spent for the instrumental calibrations and compensation of time losses when the telescope was blown of the requested position.

Observations of the comet were arranged in compact blocks of time, each of them

³<http://ssd.jpl.nasa.gov/?horizons>

Table 3.2: Molecular data & telescope characteristics.

Molecule	τ^a	Transition	ν^b	Beam ^c		$\Delta\nu^d$	η_{mB}^e
	[day]		[GHz]	[$''$]	[km] ^f	[km s ⁻¹]	
HCN	4.35	$J(1-0) F = 1-1$	88.6304160	35.5	41 907	0.0826	0.95
		$F = 2-1$	88.6318470				
		$F = 0-1$	88.6339360				
CO	107.17	$J(1-0)$	115.2712018	27.3	32 222	0.0635	0.85
H ₂ CO	0.35	$2_{0,2}-1_{0,1}$	145.6029490	21.6	25 510	0.0503	0.80
CS	6.97	$J(3-2)$	146.9690330	21.4	25 272	0.0498	0.80
CH ₃ OH	5.36	$5_{0,3}-5_{1,4}$	157.1789700	20.0	23 625	0.0466	0.78
CH ₃ OH		$4_{0,3}-4_{1,4}$	157.2461000				
CH ₃ OH		$1_{0,3}-1_{1,4}$	157.2707000				
CH ₃ OH		$3_{0,3}-3_{1,4}$	157.2724700				
CH ₃ OH		$2_{0,3}-2_{1,4}$	157.2760400				
H ₂ S	0.28	$1_{1,0}-1_{0,1}$	168.7627624	18.6	22 009	0.0434	0.76

^aPhotochemical lifetime – a characteristic timescale after which $1/e$ molecules photodissociate. Taken from Biver et al. (1999) and scaled to the middle heliocentric distance $r = 2.4533$ AU through $\tau \propto r^2$ dependence.

^bTransition frequency from the JPL spectral line catalog (Pickett et al. 1998); available online at <http://spec.jpl.nasa.gov/>.

^cHalf-power beam radius.

^dVelocity spacing of the spectral channels, corresponding to 24.4 kHz.

^eMain beam efficiency based on the telescope’s documentation (cf. footnote #2 in main text).

^fCalculated for the middle geocentric distance $\Delta = 1.6284$ AU.

dedicated to a different molecule. Our daily runs could accommodate 1–3 such blocks, and the number of spectra enclosed in one block was adjusted to the apparent S/N of the line (though unavoidably limited by the available observing time). The spectra from both polarization channels were finally averaged all together within the blocks (weight proportional to the exposure and inversely to the square of the system temperature) to produce one high-quality spectral profile per molecule per daily run. Analysis of the individual spectra within a block, as if they were a short time-series, would be pointless due to large noise, and because we do not expect to observe phenomena on the timescales shorter than few hours (see e.g. the discussion on detecting the effects from nucleus rotation in Chapters 2.5.1 and 2.7.1.5, and compare with the beam sizes of the 12-m telescope in Table 3.2).

The daily spectra were further reduced by subtracting a linear baseline. In those of CS, H₂S and H₂CO, where only one line is present, the baseline was fitted in the interval between -10 and $+10$ km s⁻¹ with a gap for the line between -3 and $+3$ km s⁻¹. However, the interval was adjusted to the specific cases of HCN and CH₃OH where several spectral features are naturally present (cf. Figs. 3.3 and 3.6 respectively), and also to CO – the spectra of which were contaminated with emission from galactic sources (cf. Fig. 3.9). After the baseline trend was removed, we determined the RMS of noise, using

Table 3.3: Line parameters as measured in the daily spectra.

Date UT ^a (Oct. 2007)	Exposure ^b [min]	Molecule	Transition	$\int T_{\text{MB}} dv$ [K km s ⁻¹]	v_0 [km s ⁻¹]
25.5427	29.4	HCN	$J(1-0)$ $F = 0-1$	0.559 ± 0.041	0.168 ± 0.077
			$F = 2-1$	2.721 ± 0.039	0.167 ± 0.013
			$F = 1-1$	1.598 ± 0.039	0.133 ± 0.022
25.6351	48.9	CO	$J(1-0)$	< 0.256 ^c	
26.5080	39.2	CH ₃ OH	$2_{0,3}-2_{1,4}$	0.691 ± 0.039	0.079 ± 0.044
			$\{ \begin{smallmatrix} 3_{0,3}-3_{1,4} \\ 1_{0,3}-1_{1,4} \end{smallmatrix} \}$	1.301 ± 0.048	
			$4_{0,3}-4_{1,4}$	0.934 ± 0.038	0.217 ± 0.032
			$5_{0,3}-5_{1,4}$	0.815 ± 0.041	0.122 ± 0.035
26.5734	29.4	CS	$J(3-2)$	1.736 ± 0.045	0.495 ± 0.020
27.4552	66.6	CO	$J(1-0)$	< 0.098 ^c	
27.5313	35.3	H ₂ CO	$2_{0,2}-1_{0,1}$	0.117 ± 0.037	0.288 ± 0.259
27.5767	17.6	HCN	$J(1-0)$ $F = 0-1$	0.210 ± 0.047	-0.061 ± 0.293
			$F = 2-1$	0.743 ± 0.045	0.262 ± 0.049
			$F = 1-1$	0.389 ± 0.048	0.322 ± 0.106
28.3765	68.7	HCN	$J(1-0)$ $F = 0-1$	0.053 ± 0.026	0.023 ± 0.469
			$F = 2-1$	0.328 ± 0.025	0.165 ± 0.065
			$F = 1-1$	0.201 ± 0.025	0.139 ± 0.096
29.3823	68.6	CS	$J(3-2)$	0.289 ± 0.021	0.324 ± 0.050
30.3948	49.1	HCN	$J(1-0)$ $F = 0-1$	0.104 ± 0.025	0.501 ± 0.336
			$F = 2-1$	0.314 ± 0.024	0.035 ± 0.053
			$F = 1-1$	0.200 ± 0.023	0.178 ± 0.115
31.4062	58.8	H ₂ S	$1_{1,0}-1_{0,1}$	0.175 ± 0.027	0.024 ± 0.052
31.4956	29.4	HCN	$J(1-0)$ $F = 0-1$	0.049 ± 0.034	0.501 ± 0.819
			$F = 2-1$	0.241 ± 0.031	-0.005 ± 0.106
			$F = 1-1$	0.120 ± 0.032	-0.256 ± 0.243

^aMiddle moment of the observing block.^bEffective exposure of the daily spectrum.^c3 σ upper limit.

the scatter of brightness in the spectral channels within the baseline-fitting intervals. In both procedures an iterative 3 σ rejection of “bad” channels was applied.

A line was parameterized by the area $\int T_{\text{MB}} dv$ and position v_0 , the latter being defined as a point splitting the area into halves. We considered the line as detected when the area was at least a factor of three above the error on it; otherwise we provide only a 3 σ upper limit. The lines were measured consequently in the interval between -3 and $+3$ km s⁻¹ around the zero velocity, though there are two exceptions: (i) the $3_{0,3}-3_{1,4}$ and $1_{0,3}-1_{1,4}$ lines of CH₃OH are blended, hence we measured them all together inside the outer limits of the individual line intervals; (ii) the separation of $F = 2-1$ and $F = 1-1$ hyperfine components of HCN $J(1-0)$ is only 4.840281 km s⁻¹ thus the facing sides of their intervals were reduced to exactly half of the separation (which does not affect the analysis as the components are completely resolved – see Fig. 3.3). The line characteristics are summarized in Table 3.3.

Errors on the line parameters were estimated using the Monte Carlo approach. On each spectrum we superimposed 1000 realizations of noise, and then, in each individual simulation we determined the parameters. Scatter of the values is a very good measure

of the investigated uncertainties (see e.g. Press et al. 1992). Therefore, as the errors we adopted the standard deviations calculated with respect to the line parameters in the original spectrum. For all the spectral channels within one spectrum we assumed the same (Gaussian) distribution of noise, with the variance equal to the square of RMS noise (determined from the baseline-fitting intervals). We acknowledge that the simulations should have been ideally based on noiseless representations of the real spectra. However, we encountered problems with obtaining good fits, presumably because of the complex line profiles in some of them. Note, that the obtained uncertainties, resulting entirely from the data noise, do not account for other error sources (e.g. neither the one on $\int T_{\text{mB}} dv$ accounts for the uncertainty on main-beam efficiency η_{mB} , nor the one on ν_0 includes the error on line's rest frequency; none of them accounts for the uncertainty on baseline subtraction, etc.).

Each cometary block was always preceded by test observations. These included integrations of continuum in Mars (preceded by pointing calibration on the planet), followed by pointing calibration on standard sources located near the comet. The latter was realized by fitting the telescope's pointing offset to a 5-point continuum map. At the last step we acquired spectra of a standard source W3(OH), which offers bright emission lines of many molecules, and which was located near the comet (we skipped this point only before the methanol block on Oct. 26.5, 2007 UT, as we had not found any literature records concerning the target transitions; on the daily runs when only one block was accommodated, we observed W3(OH) also afterwards). From these observations we concluded that the absolute stability of the instrument was better than 20%, and the pointing precision was about 5'' – the latter being at least on order of magnitude worse than the precision of ephemeris, but still having a negligible influence on the obtained spectra.

Because our discussion is based entirely on the daily spectra, we will refer simply to “spectra” most of the time in the next sections of this chapter.

3.3 Early evolution of the line shapes

Early evolution of the outburst was traced through the $J(1-0)$ transition of HCN (Fig. 3.3) and the $J(3-2)$ transition of CS (Fig. 3.4). Both lines show large and consistent day-to-day changes in their profiles:

- Oct. 25.5, 2007 UT: The first spectrum of HCN shows a double-peak line profile, with the red component being clearly stronger.
- Oct. 26.6, 2007 UT: The first spectrum of CS confirms the double-peak profile, yet the red component is relatively much stronger.
- Oct. 27.6, 2007 UT: The second spectrum of HCN shows the line to be about four times weaker than before; the profile is dominated by the red component, the blue one being hardly visible, confirming the previously noticed trend.
- Oct. 28.4, 2007 UT: The third spectrum of HCN reveals the line to be about two times weaker than the day before; the profile has clearly a single-peak shape, it is now symmetric and its position has drifted from “red” to “zero”.

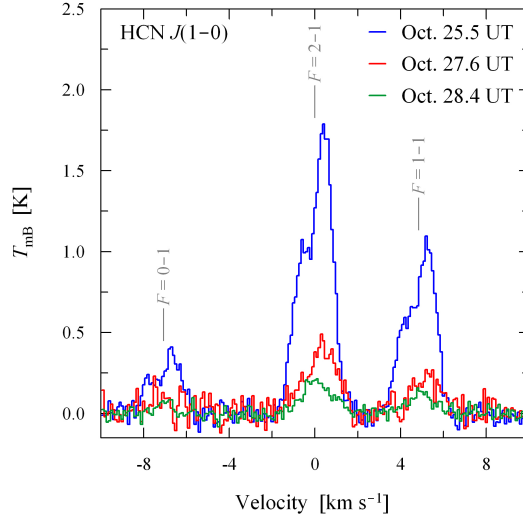


Figure 3.3: Evolution of the HCN $J(1-0)$ hyperfine triplet at 88.6 GHz. The spectra from Oct. 30.4 and 31.5, 2007 UT look the same as on Oct. 28.4, 2007 UT, thus they are omitted. The spectral resolution was reduced to 0.1 km s^{-1} for illustrative purpose to increase the apparent S/N.

- Oct. 29.4, 2007 UT: The second spectrum of CS shows the line to be six times weaker than before; the decrease in brightness is consistent with the evolution of HCN; the line profile confirms the previous observation, yet the excellent S/N makes it clearly visible that the peak is very sharp.
- Oct. 30.4 and 31.5, 2007 UT: The spectra of HCN look the same as on Oct. 28.4, 2007 UT.

This behavior is well illustrated by the temporal evolution of line area $\int T_{\text{mB}} dv$ and velocity v_0 (Fig. 3.5). It clearly shows that both lines were continually fading and reddening until Oct. 28, 2007 UT. Then the intensity of (at least) HCN temporarily stabilized, and the spectral profiles started becoming symmetric with respect to the zero velocity.

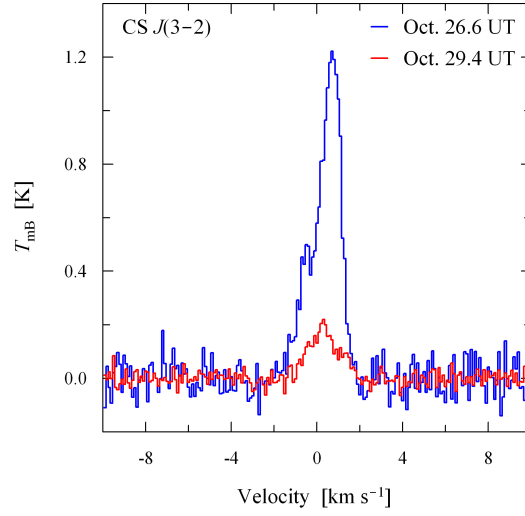


Figure 3.4: Evolution of the CS $J(3-2)$ line at 147.0 GHz. The spectral resolution was reduced to 0.1 km s^{-1} for illustrative purpose, to increase the apparent S/N.

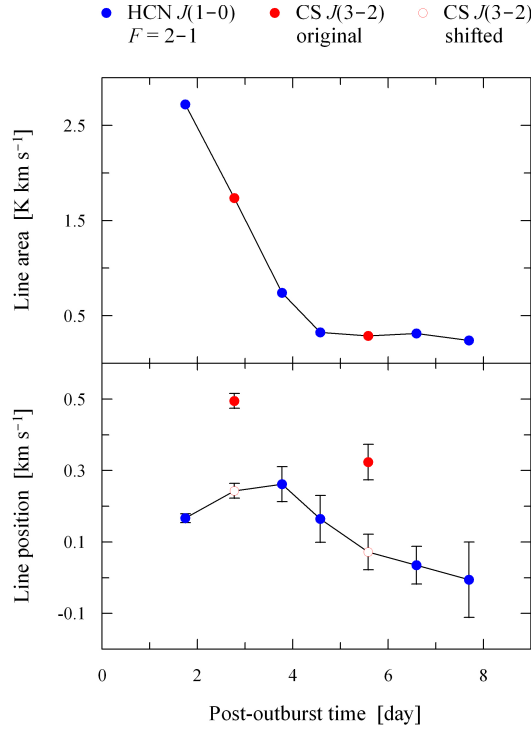


Figure 3.5: Post-outburst evolution of the line area $\int T_{\text{MB}} dv$ (*top panel*) and of the line position v_0 (*bottom panel*). The parameters were measured for HCN $J(1-0)$ $F = 1-0$ and for CS $J(3-2)$. *Top panel*: The error bars are of the order of the point size, thus they were omitted. CS excellently coincides with HCN, thus the line areas were not normalized to each other. *Bottom panel*: The line position of CS is systematically red-shifted with respect to HCN; therefore the positions shifted by $\Delta v_0 = -0.2517 \text{ km s}^{-1}$, which optimally match the HCN trend, are additionally shown to support the overall behavior. Possible reasons for this discrepancy are discussed in Section 3.7.

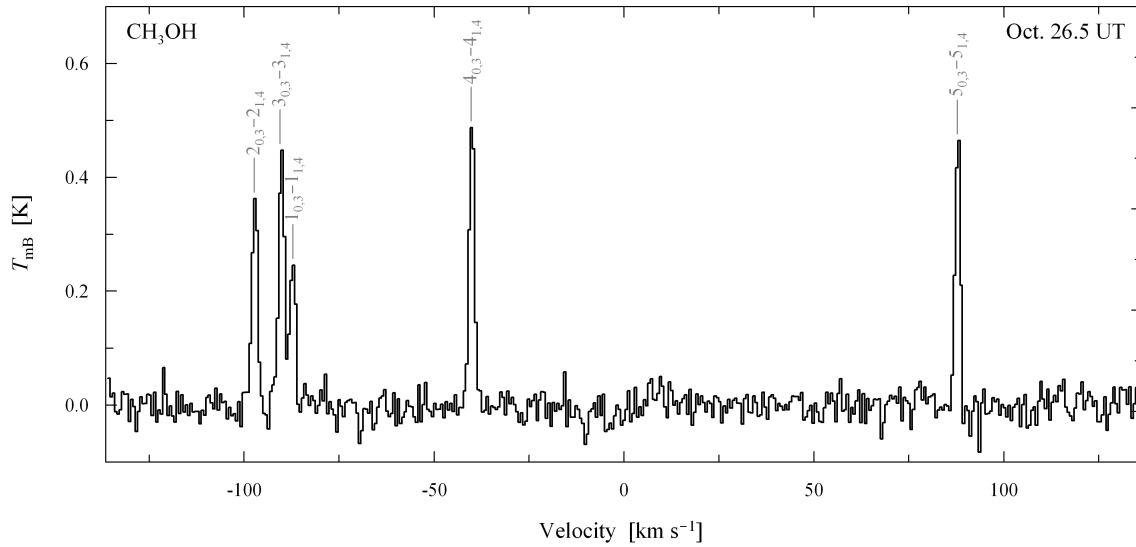


Figure 3.6: Spectrum of CH_3OH centered at 157.225 GHz. The spectral resolution was reduced to 0.6 km s^{-1} for illustrative purpose to increase the apparent S/N.

3.4 Rotational temperature and expansion velocity

As the rotational temperature we consider here the excitation temperature of the rotational transitions. It can be determined by comparing (fitting) intensities of several lines from the same molecule observed simultaneously. For this purpose, on Oct. 26.5, 2007 UT we observed five lines of CH_3OH (Fig. 3.6), three of them being completely resolved.

Assuming that the rotational energy levels are populated according to the Boltzmann distribution, we applied the rotational diagram technique (see Chapter 1.3.4; also e.g. Bockelée-Morvan et al. 1994a) to the resolved lines. We found the spectrum to be consistent with the rotational temperature of $51 \pm 8 \text{ K}$, where the adopted error results entirely from the fit quality.

Using the five line profiles in Figs. 3.3 and 3.4, we also determined the gas expansion velocity. Assuming the kinetic temperature to be equal to the above rotational temperature, and following the standard procedure (see Chapter 2.4.1; also e.g. Biver et al. 2002a), we found the mean velocity to be equal to $0.65 \pm 0.15 \text{ km s}^{-1}$, where the adopted error is a standard deviation of the constituent measurements. We note that the error reflects the real differences between the measured spectra rather than their S/N ratios.

The obtained results should be considered with great caution as they are model-dependent, and the standard models which we used are certainly far from providing accurate characteristics of comet Holmes (and perhaps of any other). For example, the temperature and velocity presumably vary with the nucleocentric distance, and perhaps with a direction too, hence the inferred quantities are *effective* for the observed part of coma. All these cause potential pitfalls which are discussed in Chapter 2.7.1.6, and which were not included (in a direct sense) in the determined errors.

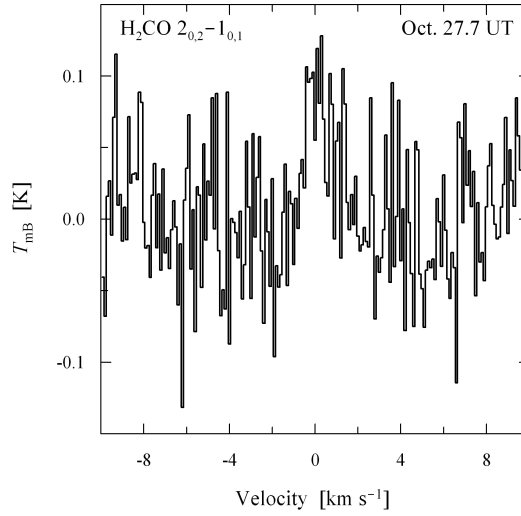


Figure 3.7: Spectrum of H_2CO at 145.6 GHz. The spectral resolution was reduced to 0.1 km s^{-1} for illustrative purpose to increase the apparent S/N.

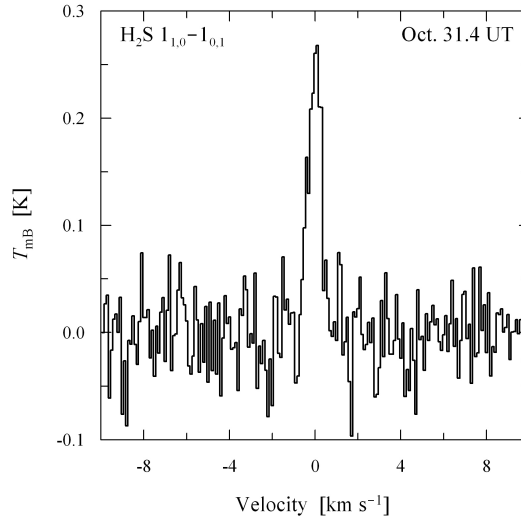


Figure 3.8: Spectrum of H_2S at 168.8 GHz. The spectral resolution was reduced to 0.1 km s^{-1} for illustrative purpose to increase the apparent S/N.

3.5 Other molecules

On Oct. 27.5, 2007 UT we detected the $2_{0,2}-1_{0,1}$ transition of H_2CO (Fig. 3.7) and on Oct. 31.4, 2007 UT we detected the $1_{1,0}-1_{0,1}$ transition of H_2S (Fig. 3.8). Despite large efforts on Oct. 25.6 and 27.5, 2007 UT, the $J(1-0)$ transition of CO was not detected.

We note, that the spectrum of H_2S shows the line to be much narrower than those of HCN and CS (cf. Fig. 3.3 and 3.4). It suggests the expansion velocity of only 0.3 km s^{-1} , which is to be confronted with 0.65 km s^{-1} determined for HCN and CS (Section 3.4), where both were measured in the same way. The reason for this difference is further investigated in Section 3.7.

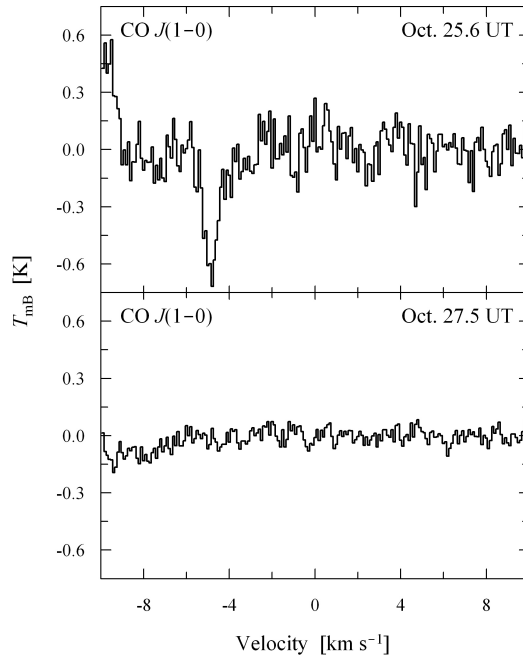


Figure 3.9: Spectra of CO at 115.3 GHz. The clear absorption and emission features are from galactic sources. They can be distinguished from cometary emissions (apparently invisible in these spectra) by their velocities significantly different from zero, which is due to different radial velocities of the sources compared to the comet. The absorption features are artifacts which appear when a source is located at the OFF position. The spectral resolution was reduced to 0.1 km s^{-1} for illustrative purpose to increase the apparent S/N.

3.6 Late monitoring

On Nov. 29.2, Dec. 5.2, and Dec. 28.2, 2007 UT, and on Mar. 14.0 and 14.9, 2008 UT, we monitored the comet using the 10-m Submillimeter Telescope (SMT) on Mt. Graham (see Fig. 2.2 in Chapter 2). The target line was the $J(3-2)$ transition of HCN at 265.88643392 GHz, which normally gives the brightest emission line in the cometary mm spectrum. At that frequency, the telescope’s half-power beam radius is equal to $14.5''$. (For more details see Chapter 2.2.)

We used the 1.3-mm sideband-separating dual-polarization SIS receiver – a prototype for ALMA⁴. From a range of facility backends, which were connected simultaneously, the most reliable ones turned out to be the *Forbes Filterbanks*, which we used for data analysis. They provide 1024 identically-arranged spectral channels in each of the receiver’s polarization channel; the spectral-channel spacing is 1 MHz, which is 1.1275 km s^{-1} at the observed frequency. The main-beam efficiency η_{mB} , averaged over both polarization channels, is equal to 0.74 ± 0.02 , as provided in the telescope’s documentation⁵. We note that it has changed comparing to our own measurements with the previous receiver; we also note that the new receiver demonstrates a substantially improved noise performance comparing to its predecessor (cf. Chapter 2.2). The temperature and velocity scales were calibrated following the standard procedures (cf. Section 3.2 and the reference therein).

⁴Read more about the ALMA project at: <http://www.alma.cl/>.

⁵http://aro.as.arizona.edu/~aro/smt_docs/smt_beam_eff.htm

We arranged and later analyzed the observations in a similar way as we did in the first part of the campaign (Section 3.2), introducing only a few changes:

- On Nov. 29.2, 2007 UT the weather conditions were particularly poor (the atmospheric transmission at zenith of about 50% at the observed frequency; this is to be compared with 80–90% on good nights), so we used the *beam & position switching* mode. The sub-reflector throw was set equal to $\pm 2'$ (which gives the offset position $4'$ away from the comet) and the nutation rate to 2.2 Hz. Using our *anisotropic model* (see next paragraph) we verified, that the coma signal at the off-source position was below 0.5% of that at the on-source position – thus completely negligible from a practical point of view.
- Except for Nov. 29.2, 2007 UT, individual exposures were equal to 10 min and resulted from twenty ON–OFF pairs. On Nov. 29.2, 2007 UT, we used 5-min exposures originating from five OFF–ON–ON–OFF sequences. Integration times at the off- and on-source positions were always the same and equal to 15 sec.
- The baseline-fitting interval was greatly extended comparing to the first part of the campaign, because of the much lower spectral resolution (thus smaller number of independent channels) in the *late* spectra. For the daily spectra from Nov. 29.2, Dec. 5.2, and Dec. 28.2, 2007 UT, we used the range between -75 and $+75$ km s $^{-1}$, whereas for those from Mar. 14.0 and 14.9, 2008 UT, the range was further extended, spanning between -400 and $+400$ km s $^{-1}$, where the difference was compelled by differences in background quality. Particularly, in the daily spectrum from Nov. 29.2, 2007 UT, the baseline is clearly curved in the specified interval, hence we subtracted it upon fitting a quadratic function. (Likewise for the *early* spectra, a gap left for the line was always between -3 and $+3$ km s $^{-1}$.)
- On Dec. 28.2, 2007 UT, after the cometary block, when the telescope was pointed toward calibration sources (V384 Per and W3(OH)), we realized a severe pointing offset, which – most probably – had occurred during the cometary observations. By comparing the off-center spectra of W3(OH) with a map of it, which we took with the same setup on a different occasion, we concluded the offset was equal to $22''$. Using our *anisotropic model* (see next paragraph) we checked, that such an offset affects cometary spectra by producing a 63% drop of the line intensity and slightly altering its profile. Thus, it may have been well responsible for the non-detection of the line on that day. Unfortunately, it is difficult to calibrate-out this problem, because we know neither: (i) how it happened (jump vs. progressive misalignment), nor (ii) when it happened. Therefore, we assumed the worst case – that is, that the cometary observations were affected by this offset right from the beginning – and, consequently, we increased the upper limit on the line area by a factor of 2.7.
- A major lesson learnt from the observations on Dec. 28.2, 2007 UT, was the need for frequent checks of the telescope's pointing. Therefore, on Mar. 14.0 and 14.9, 2008 UT, we interrupted the cometary block with a pointing calibration every eight individual exposures (approximately every 2 h).

Table 3.4: Summary of the late monitoring of HCN $J(3-2)$.

Date UT ^a	r ^b [AU]	Δ ^c [AU]	ϕ ^d [°]	τ ^e [day]	Beam ^f [km]	Exposure ^g [min]	$\int T_{\text{MB}} dv$ [K km s ⁻¹]
Nov. 29.2193, 2007 UT	2.5797	1.6816	11.244	4.81	17 728	35.9	< 0.128 ^h
Dec. 5.2461, 2007 UT	2.6045	1.7184	11.697	4.91	18 115	232.0	0.064 ± 0.013
Dec. 28.2190, 2007 UT	2.7010	1.9335	15.458	5.28	20 384	180.0	< 0.167 ^{h,i}
Mar. 14.0068, 2008 UT	3.0324	3.1466	18.397	6.65	33 172	330.0	< 0.026 ^{h,j}
Mar. 14.8901, 2008 UT	3.0362	3.1617	18.319	6.67	33 331	160.0	

^aMiddle moment of a daily run.^bHeliocentric distance.^cGeocentric distance.^dPhase angle.^ePhotochemical lifetime – a characteristic timescale after which $1/e$ molecules photodissociate. Taken from Biver et al. (1999) and scaled using $\tau \propto r^2$ dependence.^fHalf-power beam radius.^gEffective exposure of the daily spectrum.^h 3σ upper limit.ⁱCorrected for the pointing offset (see text).^jBased on the average spectrum from both daily runs.

When modeling the line-intensity drop at the offset positions (see before), we used our *anisotropic model* (Chapter 4.4), assuming a spherical uniformly-volatile nucleus as the only source of activity. Whereas some (possibly significant) sublimation from the icy grains blown at the outburst cannot be excluded, we still do not think that they significantly influenced the ON-to-OFF line-intensity ratio. This seems especially unlikely at small offsets, such as 22'' investigated for Dec. 28.2, 2007 UT. At larger offsets, such as 4' investigated for Nov. 29.2, 2007 UT, we would expect the density of grains at the offset position to be lower than around the nucleus; consequently, this would further escalate the difference between line intensity at the two distinct positions. We also note, that at the phase angle ϕ of comet Holmes (and any other ϕ different from 0° and 180°), the line-intensity drop depends on the offset's position angle. For simplicity, we did not account for this effect, which is anyway small at small ϕ , and used the average result from four symmetric offsets instead. Moreover, the error due to this uncertainty seems to be negligible comparing to the uncertainty as to whether or not the model is at all relevant to simulate the *late* spectra of comet Holmes.

In Table 3.4 we summarize this part of the campaign, and in Fig. 3.10 we additionally present the spectra from all the daily runs. It is clearly visible, that – despite large efforts – the line was detected with confidence only once, on Dec. 5.2, 2007 UT; we measured its position to be equal to -0.07 ± 0.24 km s⁻¹. For the other daily runs we obtained only more or less sensitive upper limits. On one hand this very much contrasts with the great observing material collected during the first part of the campaign, which took even less telescope's time. On the other hand it excellently demonstrates how quickly the comet was loosing its excessive activity.

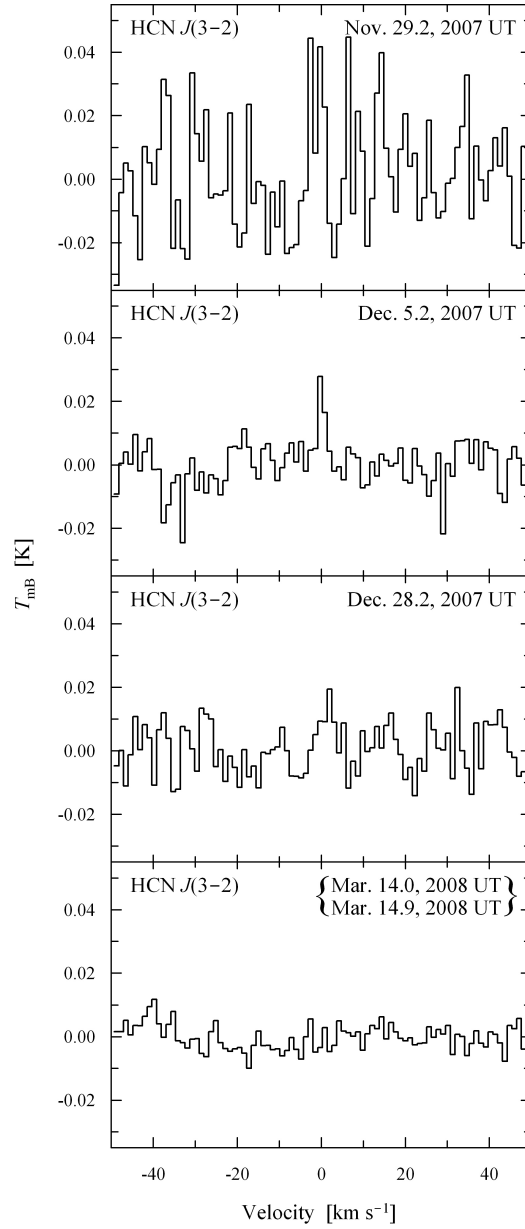


Figure 3.10: Spectra of HCN at 265.9 GHz. The spectral resolution is kept original, and equal to 1.1275 km s^{-1} . The line is clearly visible only in the spectrum from Dec. 5.2, 2007 UT. The non-detection on Dec. 28.2, 2007 UT may, at least partly, result from a severe pointing error which occurred during the exposure (see text).

3.7 Discussion

Our *early* spectra of comet Holmes pictured the outburst as a very dynamic event. They show large day-to-day changes of the line profiles, systematic differences between those of different molecules, and rapidly decreasing intensities – further confirmed by the *late* spectra. The latter suggests that the great bulk of observed peak activity originated from an impulse-like event, confirming the common impression (cf. Section 3.1). However, a continuously expanding and photodissociating spherically-symmetric cloud or bubble of gas, as visible in the optical images, is unable to produce all the aforementioned spectral characteristics alone.

First of all, in every spectrum of HCN $J(1-0)$, the line-area ratio of the hyperfine triplet – a property, which is independent of specific excitation conditions and mechanisms (Bockelée-Morvan et al. 1984) – resembles its laboratory value, which is consistent with an optically-thin emission. It is therefore safe to say, that also the other (weaker) emissions were optically thin.

Under this assumption consider a spherically-symmetric gaseous *shell* consisting of different molecules that are isotropically mixed. Assume that it was ejected instantly from a point-source, and is continuously expanding with a constant and isotropic velocity since then. In such case, all the lines would feature symmetric double-peak profiles (different areas permitted, of course) with the central dip exactly at the zero velocity. Depth of the dip would only depend on the size ratio of *shell* and beam, thus it would deepen with time (following growth of the *shell*) and show systematic differences from line to line (as the beam size depends on the observed frequency). Moreover, as the *shell* would be continuously photodecaying and expanding into less and less sensitive regions of the beam, the areas of all lines would be decreasing; that would, however, look slightly differently for different lines because of different beam sizes and molecular lifetimes (cf. Table 3.2). Of course, the processes of expansion and decay would stimulate evolution of the physical properties of the *shell* (density, mixing ratios, temperature, energy-levels distributions), but these would only globally scale its brightness (though differently for different emissions), hence would not influence the line shapes – except for the areas. Position and width of all the lines would be the same, and would not evolve at all (the position being actually fixed at the zero velocity).

Now instead of the *shell* consider a *cloud* of gas. It holds the properties of the *shell*, except for the expansion velocity which now increases with the nucleocentric distance (which is actually necessary to develop such a cloud from an instantly produced point-source). In such case spectra of different molecules would feature different shapes, yet the symmetry with respect to the zero velocity would be preserved. The reason for this is very simple: think of the growing *cloud* as of being composed of adjacent *shells* – each moving radially outwards with its own velocity. Molecules within a *shell* produce a spectrum as described before. However, spectra from different *shells* have different widths because of the different velocities (and, to a smaller extent, temperatures – see further). Since the spectrum of the entire cloud is simply a sum of them, its profile would differ from line to line (of the same, and of different molecules) in this specific way, because in each individual case the same *shell* would contribute with a different weight (or equivalently, would contribute a different fraction of the overall line-area). The reason for this is also simple: gradient of the expansion velocity would stimulate stratification of the density,

temperature, and – individually for each molecule – the energy-levels distributions, where the first and last are the properties which directly scale the brightness. (Note that the mixing ratio would remain spatially constant, or equivalently, the finite photochemical lifetimes of the molecules would not escalate the stratification of density, and that all the properties would still be isotropic.) Consequently, brightness of the cloud would also be stratified, and its distribution would vary among the lines. Therefore, and bearing in mind that the beam size is also line (-frequency) dependent, the unequal weights from the same *shell* become perfectly understandable. Needless to say, temporal evolution of the cloud would stimulate the lines to be continuously fading and metamorphosing the shapes of their profiles, yet the symmetry with respect to the zero velocity would always be preserved. (Note, that the *shells* would remain adjacent only in an infinitesimal time interval, which violates the obvious demand for global continuity. Consider this therefore as a snapshot scenario, which we present for an illustrative purpose only.)

The presented scenario can already qualitatively explain why the profiles of different lines have different widths, and – through the variable depth of the central dip – why some of them feature a single and some other a double peak. It also handles the rapid weakening of the lines, and the continues evolution of their shapes (i.e., of the width, and the central dip’s depth).

Especially striking is the difference between the line with of H_2S (Fig. 3.8) and of the others lines, so let us analyze this case more in depth. Both the photochemical lifetime and the beam size for H_2S were pretty much the same as for H_2CO observed four days earlier (Table 3.2), which means, that both spectra originated from roughly the same region of the coma. However, the latter has a significantly broader line (Fig. 3.7) – and this is evident in spite of the large noise. Did then the expansion velocity decrease in this region in the meantime? Perhaps, but it is also entirely possible that the radial profiles of the energy-levels distributions were very different for these two molecules on those days, and consequently, “promoted” visibility of different parts of the coma (different *shells*) that were expanding with different velocities. What does not seem likely though, is a decrease in velocity of the entire cloud. We do not see any physical reason for that, and it is also refuted by the “normal” width of the HCN hyperfine components (the signal of which originated from a much larger region of the coma) observed just after H_2S on that daily run (not included in Fig. 3.3 for clarity).

In spite of reproducing some of the spectral signatures, this simple scenario fails to explain a few other:

- presence of asymmetric and symmetric line profiles; for example, the asymmetric double-peak line of CS in Fig. 3.4 vs. the symmetric single-peak lines of CH_3OH in Fig. 3.6 (confirmed at the original spectral resolution) – both observed on the same daily run; also the temporal evolution of the asymmetry (Figs. 3.3 and 3.4);
- differences in the line position; for example the systematic shift between HCN and CS (Fig. 3.5) and the other lines (Table 3.3); also evolution of the line position (Fig. 3.5), and even discrepancies in the position of lines from the same molecule and observed simultaneously (the entries for CH_3OH in Table 3.3);
- temporal stabilization of the line intensity (Fig. 3.5).

These observational characteristics raise an obvious demand for the scenario with an anisotropic gas-density distribution. Therefore, and bearing in mind the results from a variety of different techniques, we propose four competing sources of activity, which contribute the molecules: (i) suddenly ejected into a spherically-symmetric cloud, (ii) sublimating from the icy grains released by the blowout, (iii) originating from the *blob* in the inner coma, and, finally, (iv) coming directly from the refreshed nucleus surface. We note here, that unlike the activity of a typical comet, and unlike the (ii–iv) activity sources of comet Holmes, the first and the primary source of its spectacular appearance cannot be parameterized by the production rate Q , which, by definition, characterizes long-lasting sublimation. Certainly, the more natural quantity is here the total number of ejected molecules N . The proposed scenario qualitatively explains the whole inventory of the observed lines, and at the same time is consistent with the outcome of other studies (cf. Section 3.1).

Note that in this discussion we silently assumed all the observed molecules to be the parents. In fact CS is presumably a daughter of CS₂; however, as the parent’s photochemical lifetime is very short ($\tau = 50 \text{ min} = 0.035 \text{ day}$ at the middle heliocentric distance $r = 2.4533 \text{ AU}$), in all practical aspects the properties of CS resemble those of the parents (Bockelée-Morvan et al. 2004a).

The determined rotational temperature and expansion velocity, though unavoidably burdened by the model simplifications, are comparable to those of other comets at similar heliocentric distances (e.g. Biver et al. 2002a). This means that at least these two characteristics of comet Holmes were pretty much normal.

In the second part of the campaign we aimed at monitoring the $J(3-2)$ transition of HCN, but only on Dec. 5.2, 2007 UT the line was detected with confidence (Fig. 3.10). We note that HCN gas in LTE at 51 K has the $J(3-2)$ line theoretically a factor of eleven brighter than the $J(1-0)$ $F = 2-1$ one – assuming that both are optically thin (see before). This difference is normally increased by different beam size at these two distinct frequencies, which is, however, difficult to evaluate for comet Holmes, as its coma-density profile remains barely investigated – especially shortly after the outburst, when it was presumably rapidly evolving. (Note, that such evaluation should, ideally, also account for the temperature and expansion velocity profiles, and include non-LTE excitation, but it is a great challenge to do it properly.) In this specific case, the difference between lines’ intensities is, however, partly reduced by the difference in comet’s orbital position which occurred in the meantime. Nevertheless, the changes of beam size and geometry can alter the line-intensity ratio by up to a factor of few, whereas the HCN brightness measured on Dec. 5.2, 2007 UT is below 3% of what was measured on the last day of the *early monitoring* (taking into account the laboratory line-intensity ratio).

Moreover, using our *anisotropic model* (Chapter 4.4), and assuming: a plane-spherical uniformly-volatile nucleus as the only source of activity, a rotational temperature of 51 K, and a gas-expansion velocity of 0.65 km s^{-1} (cf. Section 3.4), we determined the production rate of HCN on that day to be equal to $(1.8 \pm 0.4) \times 10^{25} \text{ molec s}^{-1}$. If we also assume that at least a part of this late activity originated from the leftover icy grains, the scenario that the nucleus was behaving like nothing had happened 1.5 months earlier seems quite plausible (cf. Chapter 2.4.3 and Fig. 2.8 in Chapter 2).

3.8 Summary and outlook

Summarizing, we provide the very first observations of parent molecules in comet Holmes, initiated within less than two days after its remarkable outburst. We continued monitoring it for one week on a daily basis, and then, on a few occasions, until March 2008. The early spectra show velocity-resolved, often high-S/N line profiles of five different molecules (HCN, CH₃OH, CS, H₂CO, and H₂S), and sensitive upper limits on CO. They were used to trace the evolution of the outburst, and evaluate the physical conditions in the coma. The late monitoring provides constraints on the timescale at which the comet was returning to its regular activity.

We avoid interpreting the observations in terms of the standard steady-state isotropic models (e.g. Haser 1957, or Chapter 1.3), which are, in most aspects, irrelevant for such a complex and rapidly evolving gas environment. Adequate modeling of this event is not trivial and requires a very specialized tool, which we are still far from having developed. Therefore, at the moment we cannot do more than just present our observations, and analyze them in a qualitative way.

Our ultimate goal is to develop a self-consistent model with all the four sources of activity tackled altogether. Fedded with the results from other campaigns, and then applied to our own data, it will allow us to separate the sources from each other, and consequently, to trace their individual evolutions. Eventually, we should be able to present a comprehensive picture of gas and its role in this event, starting back from the very first days after the onset of the outburst. Learning this will be then the starting point to investigate the history of its internal state before “moment zero”, that is, to uncover the silent process(es) which triggered the whole event.

4 Comet 8P/Tuttle and a new model of the cometary microwave spectra

4.1 Introduction

8P/Tuttle (Fig. 4.1) is a Halley-Type comet with an orbital period of 13.6 years. It has been named after Horace Parnell Tuttle, who discovered it on Jan. 5, 1858. However, the first discovery dates back to Jan. 9, 1790, when it was spotted by Pierre Méchain, though its periodical nature was not realized at that time. The comet is known for being the parent body of the Ursid meteors, which was first suggested by William Frederick Denning about a century ago. In spite of its long presence in the annals of astronomy, comet Tuttle has remained relatively poorly characterized until its last approach in 2007/2008.

The return in 1994 suffered from about the worst possible geometric circumstances; however, the comet was successfully detected two years earlier, when still very faint, which yielded the nucleus radius of 7.3 km (Licandro et al. 2000). In contrast, the apparition in 1980 was good, but the observing techniques still far from the current standards. Nevertheless, very comprehensive studies have been carried out with a variety of tech-

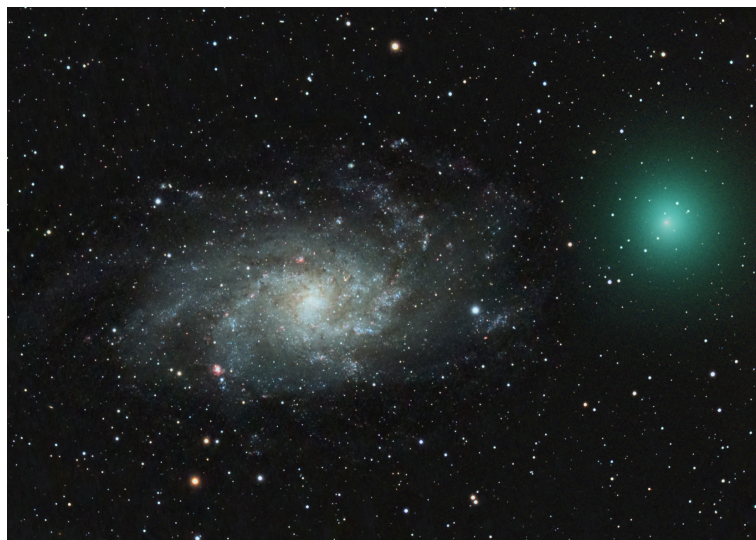


Figure 4.1: Encounter of comet 8P/Tuttle (*right*) with the Triangle Galaxy (*center*) captured by Mike Broussard on Dec. 31.1, 2007 UT in the broad optical range. The green color of the comet's coma results mostly from the emission of C_2 , which prevails in the optical spectrum of the comet.

niques, including UV spectroscopy (Weaver et al. 1981, Festou et al. 1982), narrowband optical photometry (A'Hearn et al. 1995) and optical spectroscopy (Johnson et al. 1984, Ip et al. 1985, Newburn & Spinrad 1984, 1985, Cochran 1985a,b), as well as IR photometry (A'Hearn et al. 1981, Campins et al. 1982). One of the basic conclusions was that the comet has very little dust (cf. Fig 4.1).

The recent apparition of comet Tuttle has been by far the most favorable since its discovery. Around the New Year's Day of 2008 it approached the Earth to only 0.25 AU, and at the same time was perfectly placed in the Northern hemisphere. It was a great opportunity to investigate its physical nature in detail, which prompted several observing campaigns, and resulted in very rich observing material collected across all wavelengths. Let us highlight at least some of the most important findings.

Perhaps the most remarkable result came from radar observations from Arecibo: Harmon et al. (2008a,b) suggested that the nucleus is a highly bifurcated object – possibly a contact binary. Note that currently comets are the only Solar System minor body population which do not show binarity. In addition, the intriguing possibility that it could be comprised of two chemically different components was raised by Bonev et al. (2008), who observed the comet spectroscopically in IR.

Moreover, the rotation period of the nucleus, essentially unknown prior this apparition, has been determined by several groups using a handful of techniques. Schleicher & Woodney (2007) and Woodney et al. (2008a,b), and – independently – Waniak et al. (2009), carried out narrowband optical imaging of the CN coma. Both groups observed recurrent shells from which they inferred the period to be close to 5.7 h, and concluded that they were produced by a single active vent. However, the cited above radar observations yielded the period of 11.4 h, which has been supported by the bare-nucleus-equivalent photometry from the Hubble Space Telescope (Lamy et al. 2008). An interesting possibility arises then, that perhaps the period was indeed as long as 11.4 h, however, the nucleus featured two equiproductive vents, located symmetrically on opposite sides at the same latitude. Under certain assumptions concerning the spin axis orientation and/or sublimation, such scenario might have created a coma pattern barely distinguishable from what would be produced by a single jet recurring every 5.7 h. Although such configuration would be very special thus unlikely (cf. Chapter 2.5.4), it would not be that surprising in case of comet Tuttle bearing in mind the other suggested peculiarity.

The exceptionally close approach of comet Tuttle created also another great opportunity – after comet 73P/Schwassmann-Wachmann 3 in May 2006 (see Chapter 2) – to search for manifestations of the nucleus rotation in the emission of parent molecules. We undertook this study by observing again the HCN molecule, which is perhaps the best tracer of the nucleus rotation in the mm spectrum of comets (cf. Chapter 2.1 and 2.5.1). Concurrently, these observations were coordinated with other studies by our team, which included: (i) narrowband optical imaging of the CN coma (supplemented with the C₂, C₃ and dust bands) using the 2-m telescope at Rozhen (Waniak et al. 2009), (ii) radio observations of OH at 18 cm with the 32-m radio telescope in Piwnice, and (iii) broadband optical spectroscopy with the 2-m telescope at Rozhen (Borisov et al. 2008) and 0.9-m telescope in Piwnice. The overall observational material is very rich, and several publications are currently in preparation; particularly on a unique scenario explaining the HCN and CN observations at once, which has been our ultimate goal.

In this chapter we have focused on the microwave part of the campaign. In Section 4.2

we present our data, and in Section 4.3 we show the results of a standard analysis of periodicity. Then we introduce a novel approach to this problem (Section 4.4), and present the results of its application to our data (Section 4.5). Finally, Section 4.6 summarizes this work, and outlines future developments and possible applications of this approach. Our preliminary findings have been already published by Drahus et al. (2008b,c).

4.2 Observations

We observed this comet on three consecutive dates: Dec. 31.0, 2007 UT, and Jan. 1.0 and 2.0, 2008 UT, for 5.0 h, 3.2 h, and 4.6 h respectively, using remotely the Sub-millimeter Telescope on Mt. Graham (see Fig. 2.2 in Chapter 2). The comet was at $r = 1.10$ AU, $\Delta = 0.25$ AU, and $\phi = 56^\circ$. Our target line was the $J(3-2)$ transition of HCN at 265.88643392 GHz, which normally gives the brightest emission line in cometary mm spectrum.

We used the *1.3-mm* sideband-separating dual-polarization SIS receiver – a prototype for ALMA¹. The highest spectral resolution of 250 kHz was provided by a pair of identical *Filterbanks* – each connected to a different polarization channel of the receiver. Note that this resolution corresponds to 0.28 km s^{-1} at the observed frequency (or equivalently $\nu/d\nu = 1.1 \times 10^6$), which makes the spectra velocity-resolved, and hence is sufficient for studying the kinematics of HCN. Each of the spectrometers provided a total bandwidth of 64 MHz, which was divided into 256 spectral channels.

At the observed frequency, the telescope’s half-power beam radius was $14.5''$, that is 2600 km at the comet’s distance, and the main-beam efficiency η_{mB} was 0.74 ± 0.02 when averaged over both polarization channels². Position of the comet was continually calculated from the orbital elements provided by the JPL HORIZONS system³ for the epoch of our observations. The spectra were taken in a *position-switching* mode, with a 0.5° offset for the sky-background determination (where the coma contribution was completely negligible). The temperature and velocity scales were calibrated following the standard procedures (cf. Chapter 1.2 and Chapter 2.2).

Our observing strategy was the same on each date. After the initial calibrations, the observations were arranged in a closed cycle, which was repeated incessantly over the entire daily run. First, 2 consecutive 8-min exposures of the comet were taken, and then followed by 2 short (1.3 or 2-min) exposures of a standard source W3(OH). In each case half of the exposure was given to the observed target and half was spent for measuring the background. One complete cycle: Tuttle–Tuttle–W3(OH)–W3(OH) took about 30 min (integrations + calibrations + switching), and eventually comprised one point in our time series (hereafter a *master spectrum*). Note however, that for each single exposure we obtained in fact two independent spectra – from the two polarization channels. Thus, in fact, each master spectrum was created upon averaging 4 unrelated 8-min spectra. The only exception is the master spectrum #17 – the last one from the middle date – which is a single exposure (yet still from both polarization channels), as there was no time left to take the second one. In total we have got 27 master spectra: 10 on the first date, 7 on the

¹Read more about the ALMA project at: <http://www.alma.cl/>.

²See http://aro.as.arizona.edu/~aro/smt_docs/smt_beam_eff.htm.

³<http://ssd.jpl.nasa.gov/?horizons>

middle, and 10 on the last one. All of them are presented in Fig. 4.2.

As for the millimeter-astronomy standards the quality of these spectra is exceptionally high. This is because of few factors which fortunately coincided during our run: (i) an extremely dry atmosphere (the H₂O column typically of 1.5 mm) provided a transmission of about 90% at zenith, which is very high at the observed frequency (cf. Chapter 1.2); (ii) the newly installed ALMA-prototype receiver demonstrated an excellent stability and noise performance; (iii) tracking of the telescope was unusually stable; and finally (iv) we encountered nearly no technical problems, which is rare even nowadays!

4.3 Analysis

For the obvious physical reasons, neutral parent molecules are excellent candidates to be used for studying the rotation of active comets (cf. Chapter 2.5.1). It may manifest itself by stimulating the variability of: (i) line area, (ii) line position, and (iii) specific line profile. The first two effects were found by Biver et al. (2007) for comet Tempel 1 using HCN, and the last two by Henry et al. (2002), Henry (2003) and (tentatively) Boissier et al. (2007) for Hale-Bopp, using CO and sulfur-bearing molecules respectively. Jockers & Szutowicz (priv. comm.) found the second effect alone for comet 2P/Encke using HCN, and the first effect alone was observed for comet C/2001 Q4 (NEAT) in H₂O (Biver et al. 2009), and for comet C/2007 N3 (Lulin) in many molecules (Biver, priv. comm.). This list has been extended by our own detection of the line-area variability in comet 73P-C/Schwassmann-Wachmann 3 (Chapter 2.5).

Looking at the spectra of comet Tuttle in Fig. 4.2 it becomes obvious that the line profile was indeed evolving in an organized manner on a short timescale – presumably due to the nucleus rotation. The profile has two components: one at about -1 km s^{-1} (hereafter the *blue component*), and the other one at about $+0.5 \text{ km s}^{-1}$ (hereafter the *red component*). The blue component dominates in most of the spectra – except for the last two, where the red one is clearly brighter (especially in the very last one). This basic observation is of a fundamental importance, as it readily implies that the nucleus rotation phases covered by the last two spectra could not have been observed before. Consequently, this leads to the following windows for the rotation period:

- 5.70 h – 5.75 h,
- 7.32 h – 7.67 h,
- 10.35 h – 11.51 h,
- 13.95 h – 15.35 h,
- ...,

where the first two windows are independent and are followed by their multiples. Higher multiples are also possible, but they suffer from an insufficient overlap or/and coverage of the observed rotation phases, thus it is impossible to evaluate their reliableness. Overall, the obtained windows are nicely consistent with the results from other techniques (Section 4.1).

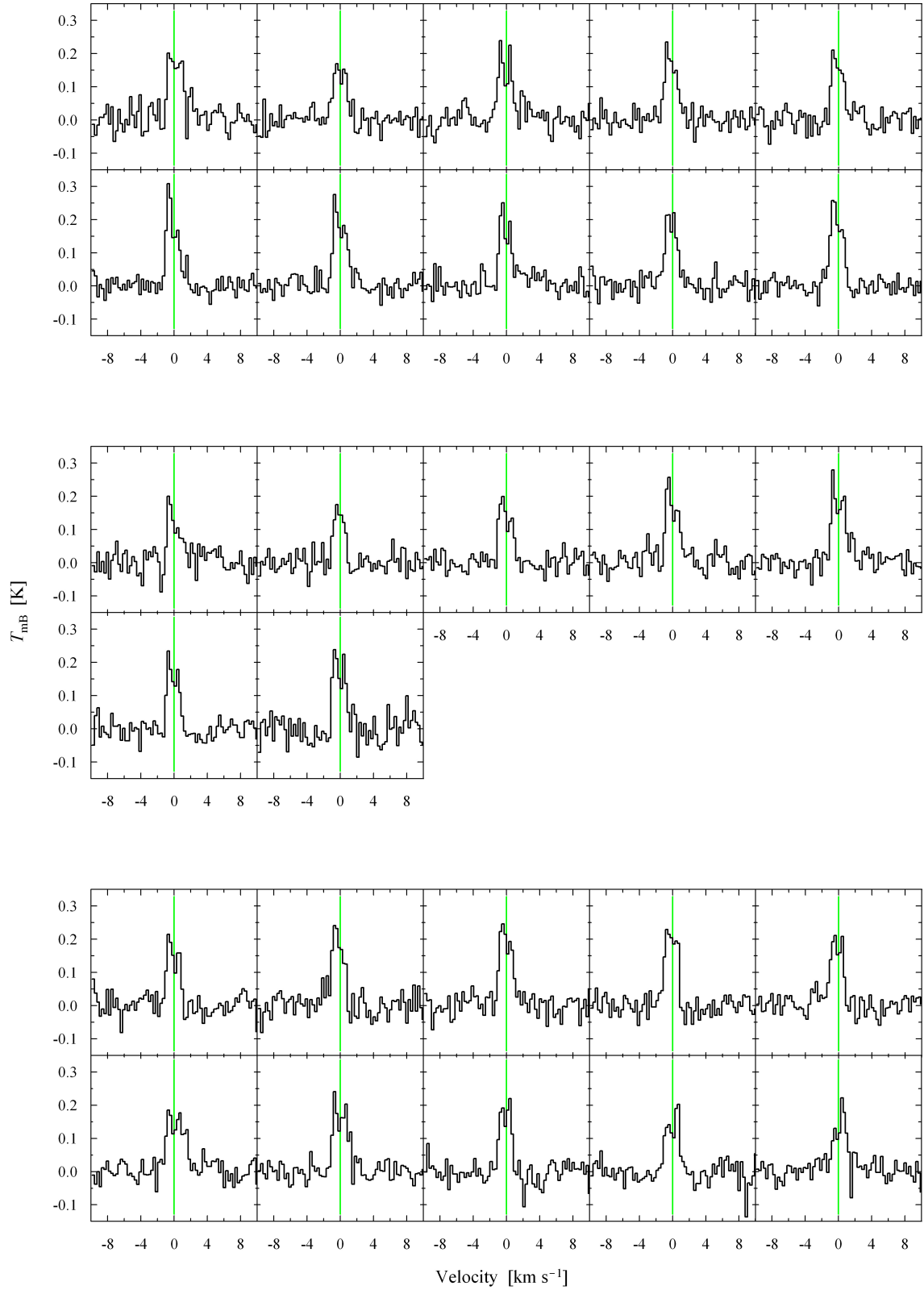


Figure 4.2: The master spectra of HCN at about 265.9 GHz at the original spectral resolution of 0.28 km s^{-1} . The three blocks correspond to the first (*top*), middle (*middle*), and last (*bottom*) date of observations. Time increases from *left to right*, and the spectra from the same night are approximately 30 min apart.

Surprisingly, however, a periodographic analysis of the line area and position, performed in the same manner as described in Chapter 2.5.2, did not yield any statistically-significant solution, though the above periodicities were clearly visible. We interpret this as being caused by (i) a small number of the data points, and (ii) an intrinsically small amplitudes of the variabilities of both line parameters.

4.4 A new model of cometary microwave spectra

Anisotropic outgassing – often in combination with non-uniform nucleus volatility – has been evidenced by imaging the daughter and dust comae for many years now. Subsequently, adequate Monte-Carlo techniques have been developed to model these effects and retrieve information about the nucleus spin and activity pattern.

Nowadays, there is a rapidly growing observational evidence for great importance of these effects also in microwave spectra of comets (cf. Section 4.3). This creates an obvious and immediate demand for similar constructions, which should replace the time-honored isotropic model of Haser (1957). Surprisingly, however, little was done in this matter to date. Hu et al. (1991) modeled the spectral line shapes under anisotropic outgassing, and Larson et al. (1991) applied it to the velocity-resolved spectra of H₂O in comets Halley and C/1986 P1 (Wilson). Later, Bockelée-Morvan et al. (2004b) modeled the spectra of HCN in comet 19P/Borrelly with a stationary polar jet. However, in all these works, and also in few other on modeling the radio lines of OH, the anisotropy was constant in time, that is, the coma was in a steady state. This was guaranteed either by the assumption that a sublimation from a unit surface element depends solely on the solar zenith angle, or by polar location of the area with an enhanced volatility. In reality, however, the anisotropy is time-dependent, that is stimulated by the nucleus rotation (on a short timescale), and by orbital motions of the comet and observer (on a long timescale).

To our best knowledge, only Henry et al. (2002) and Henry (2003) modeled cometary spectra accounting for the time-dependent anisotropic outgassing. To interpret the short-term line position variability of CO in comet Hale-Bopp, they assumed a rotating nucleus with a jet. Knowing *a-priori* the rotation period and spin axis orientation, they retrieved the location, opening angle and strength of the jet. We are also aware of an on-going study by Jockers & Szutowicz (priv. comm), aimed at a similar characterization of a jet in 2P/Encke, using the same *a-priori* information about the comet. It is based on their microwave spectroscopy of HCN and narrowband optical imaging of CN carried out nearly simultaneously. All the other detections of rotation-stimulated variability in cometary spectral lines (cf. Section 4.3) were treated only with a standard periodicity analysis of the line parameters (area and/or position) which yields the nucleus rotation period.

Our ambition was to go further than that, and make use of the complete spectral line profiles. That is because they contain far more information than any of the line parameters, i.e. the area and position, considered either alone or altogether. Therefore, only an adequate model for the lineshapes would be capable of exploring completely the potential of cometary microwave spectra.

4.4.1 Coordinate systems

We define the Sun–comet–observer plane as the *model plane*, and the plane which crosses the comet and is normal to the comet–observer line as the *observing plane*. Note that the planes are orthogonal.

Let us now define three Cartesian coordinate systems $\vec{C}_i = (x_i, y_i, z_i)$:

- \vec{C}_1 : a system on the surface of a spherical nucleus; the system rotates with the nucleus and z_1 is the nucleus spin axis;
- \vec{C}_2 : a non-rotating system originating at the nucleus center; z_2 is normal to the model plane and is in the observing plane, and x_2 points at the Sun;
- \vec{C}_3 : the same as for $i = 2$, except that x_3 points at the observer, hence z_3 and y_3 are in the observing plane.

All the systems are left-handed, and the spherical coordinates $\vec{S}_i = (r_i, \theta_i, \varphi_i)$ are given by:

$$\begin{cases} x_i = r_i \cos \theta_i \cos \varphi_i \\ y_i = r_i \cos \theta_i \sin \varphi_i \\ z_i = r_i \sin \theta_i \end{cases} \quad (4.1)$$

where $r_1 = r_2 = r_3 \equiv r$ is the radial distance, θ_i is measured from xy_i towards z_i , and φ_i is measured in xy_i from x_i towards y_i .

Note that transformation $\vec{S}_2 \rightarrow \vec{S}_3$ is trivial, and involves only the angle φ :

$$\varphi_3 = \varphi_2 + \phi, \quad (4.2)$$

where ϕ is the phase angle of the comet.

Oppositely, transformation $\vec{S}_2 \rightarrow \vec{S}_1$ is utmost general, as it involves the nucleus spin axis orientation (β, γ) and the instantaneous rotation phase $\alpha = \alpha(t)$; in the Cartesian coordinates \vec{C}_i we define it in the following convention:

$$\begin{cases} x_1 = x_2(\cos \gamma \cos \alpha - \sin \gamma \cos \beta \sin \alpha) - y_2(\sin \gamma \cos \alpha + \cos \gamma \cos \beta \sin \alpha) + z_2 \sin \beta \sin \alpha \\ y_1 = x_2(\cos \gamma \sin \alpha + \sin \gamma \cos \beta \cos \alpha) - y_2(\sin \gamma \sin \alpha - \cos \gamma \cos \beta \cos \alpha) - z_2 \sin \beta \cos \alpha \\ z_1 = x_2 \sin \gamma \sin \beta + y_2 \cos \gamma \sin \beta + z_2 \cos \beta \end{cases} \quad (4.3)$$

where: β is the spin axis latitude – the angle between z_1 and z_2 measured from z_2 towards z_1 ; γ is the spin axis longitude – the angle between z_1 and y_2 measured in xy_2 from y_2 towards x_2 ; $\alpha = \alpha(t)$ is the nucleus rotation phase, which measures the rotation of xy_1 about z_1 , increasing with time t from an arbitrarily chosen phase zero $\alpha_0 = \alpha(t = 0)$; it is given by $\alpha(t) = \alpha_0 + 2\pi t/P$, where P is the nucleus rotation period. Worth noting is that the coefficients of reverse transformation can be conveniently obtained upon transposing those of the forward one in Eq. (4.3).

Equations (4.1), (4.2), and (4.3) provide a closed set for transforming coordinates between the systems. Let us highlight some basic conclusions from these definitions:

- $\alpha, \gamma, \varphi \in [0^\circ, 360^\circ), \beta \in [0^\circ, 180^\circ], \theta \in [-90^\circ, +90^\circ]$,

- the North Pole $\theta_1 = +90^\circ$ points at the Sun (i.e. $z_1 = x_2$) for $\beta = 90^\circ$ and $\gamma = 90^\circ$,
- if $\beta = 0^\circ$ and $\gamma = 0^\circ$, then for $\alpha = +30^\circ$ axis x_2 intersects with the nucleus surface at $\theta_1 = 0^\circ$ and $\varphi_1 = +30^\circ$ (note the signs),
- the radial distance in the observing plane ρ_3 is

$$\rho_3 = r \sqrt{1 - \cos^2 \theta_2 \cos^2(\varphi_2 + \phi)}. \quad (4.4)$$

4.4.2 Sublimation potential and activation function

Now consider a surface element dS located at (θ_1, φ_1) . Instantaneous contribution of the element to the overall production rate Q is dQ , and we define it as:

$$dQ(\theta_1, \varphi_1, t) = \eta(\theta_1, \varphi_1) \Lambda(z_\odot) dS(\theta_1, \varphi_1), \quad (4.5)$$

where $\eta(\theta_1, \varphi_1)$ is the surface *sublimation potential*, and $\Lambda(z_\odot)$ is the *activation function* which scales the potential according to the (time-dependent) solar zenith angle $z_\odot(\theta_1, \varphi_1, t)$. In the non-rotating coordinate system \vec{S}_2 the situation is opposite: the sublimation potential $\eta(\theta_2, \varphi_2, t)$ depends on time, whereas the zenith angle $z_\odot(\theta_2, \varphi_2)$ does not. Note that $\cos z_\odot = \cos \theta_2 \cos \varphi_2$, and $dS(\theta_1, \varphi_1) = R^2 \cos \theta_1 d\theta_1 d\varphi_1$ where R is the nucleus radius.

This immediately implies that the overall instantaneous production rate Q is:

$$Q(t) \equiv \int dQ(t) = \int_0^{2\pi} \int_{-\frac{\pi}{2}}^{\frac{\pi}{2}} \eta(\theta_2, \varphi_2, t) \Lambda(z_\odot) R^2 \cos \theta_2 d\theta_2 d\varphi_2, \quad (4.6)$$

where the coordinates transformation $(\theta_2, \varphi_2) \rightarrow (\theta_1, \varphi_1)$ can be done as explained in Section 4.4.1.

It is convenient to operate with a dimensionless *relative* sublimation potential η^* , which assigns a certain weight to a surface element, and then determine η by an appropriate normalization:

$$\eta(\theta_2, \varphi_2, t) = \eta^*(\theta_2, \varphi_2, t) \frac{\overline{Q}}{\frac{1}{P} \int_0^P \int_0^{2\pi} \int_{-\frac{\pi}{2}}^{\frac{\pi}{2}} \eta^*(\theta_2, \varphi_2, t) \Lambda(z_\odot) R^2 \cos \theta_2 d\theta_2 d\varphi_2 dt}, \quad (4.7)$$

where \overline{Q} is the mean diurnal production rate – that is the production rate $Q(t)$ averaged over the complete rotation cycle. Note that when using η^* and \overline{Q} instead of η , the nucleus radius R is naturally removed from the equation for $Q(t)$.

Determination of the actual activation function $\Lambda(z_\odot)$ is a challenging problem on its own. Appropriately tackled, it should be based on a detailed balance between the energy gain from the insolation, and the losses – among which sublimation is only one of the contributing effects (cf. e.g. Gutiérrez et al. 2000, Prialnik et al. 2004). For practical purposes, however, a simple activation function:

$$\begin{cases} \Lambda(z_\odot) = \cos z_\odot & \text{for } z_\odot > 0 \\ \Lambda(z_\odot) = 0 & \text{for } z_\odot \leq 0 \end{cases} \quad (4.8)$$

is a good first approximation (Prialdnik, priv. comm; Szutowicz, priv. comm), which we implemented also in our code.

It is important to note that for the constant activation function and distribution of the sublimation potential, $\Lambda(z_\odot) = \text{const}$ and $\eta^*(\theta_1, \varphi_1) = \text{const}$, the model reduces itself to the standard isotropic steady-state model of Haser (1957).

4.4.3 Distribution of molecules

Consider now a narrow emission cone originating at the nucleus center, and encircling the element dS at the surface. The cone is directed along (θ_2, φ_2) . Following the argumentation in Chapter 1.3.1, the number of molecules dn in the cone between r and $r + dr$ is independent of r , and equal to $dn(\theta_2, \varphi_2) = dQ(\theta_2, \varphi_2)/v_{\text{gas}} dr$.

Let us now modify this scenario by introducing an exponential photodecay (which attenuates the number of parent molecules), and – specifically to our non-steady-state model – a modulation by the nucleus rotation. First, we assume gas to be moving radially outwards from the nucleus. The velocity of gas v_{gas} is assumed to be constant throughout the coma, i.e. independent of direction (θ_2, φ_2) and of the nucleocentric distance r . Now consider a chunk of gas emitted from the nucleus at the moment of sublimation t_s . Under the above assumptions the nucleocentric distance of the molecules at a moment t is:

$$r = v_{\text{gas}}(t - t_s), \quad (4.9)$$

Consequently, we can write:

$$dn(r, \theta_2, \varphi_2, t) = dQ(\theta_2, \varphi_2, t_s(r, t))/v_{\text{gas}} \Upsilon(r) dr, \quad (4.10)$$

where the $\Upsilon(r)$ is the *photodissociation function*, which is given for parent molecules by $\Upsilon(r) = e^{-r/l}$, where l is the *photodissociation scalelength*; l is related with the *timescale* τ through the gas velocity v_{gas} (cf. Eq. 4.9). Note that the photodissociation process occurs in time domain, and the presented formulation in space domain holds only as long as our assumptions concerning the gas velocity v_{gas} hold.

The above equation accounts for the fact that an outgassing from a given surface element varies over the rotation cycle as the insolation changes. Hence, the instantaneous number of molecules at a distance r is calculated not from the instantaneous production rate contribution $dQ(t)$, but rather from the one retarded to the moment of sublimation t_s , when exactly these molecules were emitted into the cone. For any moment t and distance r the moment t_s can be calculated from Eq. (4.9). Since for a fixed $r = r_f$ we have a linear evolution of t_s with time t , it becomes clear that also the number of molecules $dn(r_f, t)$ changes with time (in a closed cycle, as the nucleus rotates). Therefore, the presented model is a non-steady-state construction. Simultaneously, for a fixed $t = t_f$ the number of molecules $dn(r, t_f)$ varies along the cone in a repetitive manner (molecules from earlier rotation phases are located farther from the nucleus than those emitted later), which is superimposed on the monotonic photodecay. Overall, for a certain spin axis orientation and a jet-like distribution of the sublimation potential, the coma features density waves moving recurrently away from the nucleus, as observed e.g. in the optical images of comet Tuttle (cf. Section 4.1).

4.4.4 Calculation of a spectral line profile

Let us first assume that the line is optically thin. In order to synthesize its profile, we begin with integrating the number of molecules along the cone, weighted by the main-beam sensitivity profile $G(\rho_3)$. By doing that, we take a full advantage of assuming the line to be optically thin, and of a constant line-of-sight component of the velocity along the cone v_{rc} . Now we can derive the number of molecules inside the cone effectively visible by the beam dN_{eff} :

$$dN_{\text{eff}}(\theta_2, \varphi_2, t) = \int_0^{r_{\text{max}}} dn(r, \theta_2, \varphi_2, t) G(r) dr, \quad (4.11)$$

where $dn(r, \theta_2, \varphi_2, t)$ is given by Eq. 4.10, and $G(r)$ by Eq. 1.1 in Chapter 1. Note that Eq. (4.4) relates r with ρ_3 , where the latter is a natural argument for the beam sensitivity, and can also conveniently replace r_{max} for the integration cut-off.

The effective number of molecules $dN_{\text{eff}}(\theta_2, \varphi_2, t)$ can be now easily converted into the brightness temperature generated within the cone (cf. Chapter 1.3.2). Subsequently, it can be spread along the entire spectrum, where the normalized distribution $f(v_r)$ is given by the Maxwell-Boltzmann equation:

$$f(v_r) = \sqrt{\frac{m}{2\pi kT}} e^{-\frac{m(v_r - v_{rc})^2}{2kT}}, \quad (4.12)$$

where m is a mass of one molecule, T is the gas temperature (assumed to be constant throughout the coma), and $k = 1.3806503 \times 10^{-23} \text{ J K}^{-1}$ is the Boltzmann constant. Note that v_{rc} – that is the line-of-sight component of velocity for the molecules in the cone – can be easily calculated through the transformations introduced before in Section 4.4.1:

$$v_{rc} = -v_{\text{gas}} \cos \theta_2 \cos(\varphi_2 + \phi), \quad (4.13)$$

where the minus sign is added *ad hoc* to make the equation compatible with the common redshift and blueshift convention (see Chapter 1.2.3).

Finally, calculation of the line profile is completed upon co-adding the individual contributions from all the directions (θ_2, φ_2) and all the lines (including the hyperfine components) in the synthesizing region.

4.4.5 A spectral line profile at an offset position

It is easy to generalize Eq. (4.11) to take into account an offset position of the beam (i.e. a pointing away from the comet's center). Such an arrangement may be used for e.g. estimating the influence of pointing errors, or modeling spectral maps (individual pixels do not need to be integrated simultaneously).

In such a case, a distance in the observing plane between a given point in the coma (r, θ_2, φ_2) and the beam center is no longer given by the radial position of the point ρ_3 (Eq. 4.4). It must additionally include the offset distance of the beam δ_3 and the offset position angles of the beam ϵ_3 and of the point ε_3 . Using the law of cosines, and denoting this distance as d_3 , we obtain:

$$d_3^2 = \rho_3^2 + \delta_3^2 - 2\rho_3\delta_3 \cos(\epsilon_3 - \varepsilon_3), \quad (4.14)$$

where both offset position angles are measured from y_3 towards z_3 . Note that ε_3 can be easily determined using the transformations in Section 4.4.1:

$$\tan(\varepsilon_3) = \frac{\tan(\theta_2)}{\sin(\varphi_2 + \phi)}. \quad (4.15)$$

Now using Eq. (4.4) with $G(d_3)$ instead of $G(\rho_3)$ is the only modification needed to model off-center spectra.

4.5 Application to the spectra of comet Tuttle

4.5.1 Implementation and basic results

In the first approach we modeled our spectra assuming:

- the rotation period P equal to 5.715 h (cf. Section 4.1);
- a single area of an enhanced sublimation potential (hereafter a *jet*), such that:
 - the potential is a factor of 100 larger than outside the area,
 - the angular radius is equal to 35° (hence it produces a cone with an opening angle of 70° as suggested by Waniak et al. 2009);
- the gas expansion velocity v_{gas} equal to 0.8 km s^{-1} , as we determined from the spectra in a classical way (cf. Chapter 2.4.1 and 2.7.1.6; also e.g. Biver et al. 2002a);
- the gas temperature T equal to 40 K, as determined by Biver et al. (2008).

We integrated the numbers of molecules $dn(r, \theta_2, \varphi_2, t)$ with a constant angular step size $\Delta\theta_2 = \Delta\varphi_2 = \Delta\alpha = 4^\circ$. The radial step was chosen automatically as $\Delta r = P v_{\text{gas}} \frac{360^\circ}{\Delta\alpha}$, that guarantees appropriate sampling of the rotation-stimulated radial density gradient, and the integration cut-off was set at 3 half-power beam radii. Then we scanned through the entire spaces of the spin axis orientations (β, γ) and jet central coordinates (θ_1, φ_1) with a step size of 6° in both coordinates. For each set of parameters a time series of model profiles was calculated and compared with the observed spectra.

As a parameter measuring goodness of the fit, we used

$$\xi = \frac{\sigma_{\text{fit}}}{\sigma_{\text{obs}}}, \quad (4.16)$$

where σ_{fit} is the overall standard deviation of the model profiles from the observed ones, calculated channel by channel in the velocity interval between -3.5 and $+3.5 \text{ km s}^{-1}$, and σ_{obs} is the overall observing noise that plays a role of a normalizing factor, calculated in the same way in the velocity intervals from -10.0 to -3.5 and from $+3.5$ to $+10.0 \text{ km s}^{-1}$. Note that we calculated ξ using all the spectral channels from all the spectra altogether; however, in the numerator σ_{fit} they were weighted according to their quality, using the weights inversely proportional to the squares of signal uncertainties in the channels. For practical reasons we assumed that the weights were the same for all the channels within

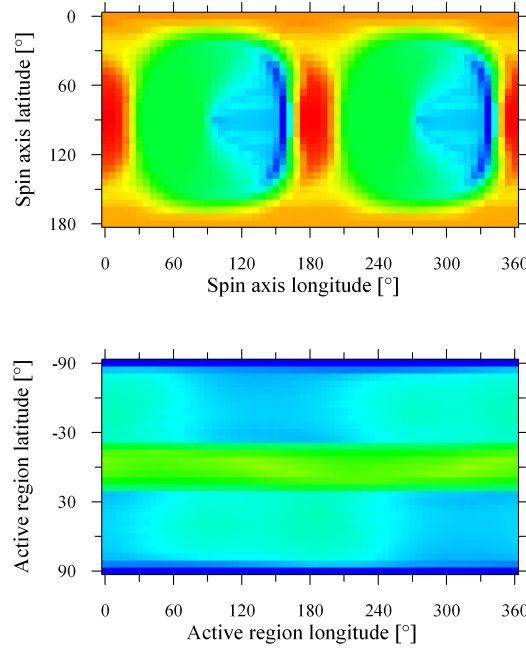


Figure 4.3: Adaptive crosscuts: *top panel* illustrates the space of spin axis orientations (β, γ) , and *bottom panel* the space of active area positions (θ_1, φ_1) . Color scale extends from $\xi = 1.35$ for the best solutions (*blue*) to $\xi = 2.55$ for the worst solutions (*red*). The common step size was 6° .

one spectrum, and determined them from the same velocity intervals as used for calculating the denominator σ_{obs} . Note that for a perfect fit $\xi = 1$; when $\xi > 1$ the fit is not optimal, and when $\xi < 1$ the fit reproduces unrealistic spectral structures (we are fitting noise, basically speaking). In the course of fitting the model the mean diurnal production rate \bar{Q} was automatically retrieved in the LSQ sense; note that it is a simple linear parameter scaling identically the intensity of all the spectra within a time series.

The obtained result provides the values of ξ in a multidimensional space of free parameters. To visualize the output, we calculated *adaptive crosscuts* through the spaces of the investigated parameters: to each orientation of the spin axis (β, γ) we assigned the best solution from the entire space of jet coordinates (θ_1, φ_1) , and vice-versa, to each location of the jet (θ_1, φ_1) we assigned the best solution from the entire space of spin axis orientations (β, γ) . Though the resulting adaptive crosscuts are correlated, they display the spaces of the free parameters separately. The crosscuts obtained for comet Tuttle are presented in Fig. 4.3.

It is immediately visible that both spaces feature longitudinal and latitudinal symmetries. This fact is not surprising though, bearing in mind that the retrieval is performed in the space of radial velocities. The spin axis longitude γ is very localized, latitude β moderately, and the jet coordinates relatively poorly. Due to the aforementioned symmetries, the best solution is found at four different combinations of the parameters:

$$\begin{aligned} \beta &= 78^\circ, & \gamma &= 156^\circ, & \theta_1 &= -90^\circ, \\ \beta &= 78^\circ, & \gamma &= 336^\circ, & \theta_1 &= +90^\circ, \\ \beta &= 102^\circ, & \gamma &= 156^\circ, & \theta_1 &= -90^\circ, \\ \beta &= 102^\circ, & \gamma &= 336^\circ, & \theta_1 &= +90^\circ. \end{aligned}$$

We note that the solution corresponds to the polar location of the jet. It is hence pathologic, as it does not allow for any rotation-driven variability – contrasting with what is discernible in our spectra (cf. Section 4.3). Moreover, the obtained spin axis orientation corresponds to the Earthward tilt⁴ of 74° . This disagrees with the radar observations from Arecibo (obtained around the same time), which suggest the tilt between 0° and 60° (Harmon, priv. comm.), however, is in support of the results from narrowband optical imaging of CN (obtained only about a week later), which indicate the spin axis orientation not far from the Earthward direction, i.e. the Earthward tilt not far from 90° (Waniak et al. 2009).

4.5.2 Further approaches

Being unsatisfied with the first results, we repeated the modeling for the scenario with 11.4-h rotation period, and two equiproductive vents located symmetrically on opposite sides of the nucleus at the same latitude. However, the polar solution (twofold degenerate this time) was again the best. For both scenarios we also investigated a range of expansion velocities, rotation periods (around the expected values), and jet opening angles, but the above solution was notoriously the dominating one. We concluded hence, that a substantial fraction of sublimation must have been indeed independent of the nucleus rotation. This is consistent with our earlier observation, that – overall – the line profile did not change very much over the rotation cycle (Section 4.3). Therefore the code was forcing the polar location of jet(s) – as it was the only possibility to reproduce such situation. Consequently, it could not account for the “second-order” effects, which stimulated the (not-so-strong) line variability. However, the polar cap seems to be real, since it produces the red component of the profile; a uniformly volatile nucleus $\eta^*(\theta_1, \varphi_1) = \text{const}$ with the assumed activation function Λ would always produce a single-peak profile.

In order to reproduce also the slight variability of the line profile, we increased the number of individual features which parameterize the distribution of the sublimation potential – each feature being characterized by the sublimation potential η^* , surface radius, and central coordinates (θ_1, φ_1) . Then, upon investigating all the spaces of free parameters again, we concluded the following properties of comet Tuttle:

- the rotation period of $P = 11.4$ h (cf. Section 4.1);
- the spin axis orientation of $\beta = 88^\circ, \gamma = 168^\circ$;
- the mean diurnal production rate of HCN of $\bar{Q} = 2 \times 10^{25}$ molec s⁻¹;
- the velocity of gas of $v_{\text{gas}} = 0.85$ km s⁻¹;
- a Southern polar cap with an enhanced sublimation potential, such that:
 - the potential η^* is a factor of 40 larger than the base potential outside the cap,
 - the angular radius is equal to 30° , hence the cap extends from the Southern pole at $\theta_1 = -90^\circ$ up to $\theta_1 = -60^\circ$;
- a small but very active circum-polar vent, such that:

⁴Earthward tilt is the angle measured from the observing plane towards the spin axis; the angle between the spin axis and the line of sight is hence complementary to the Earthward tilt.

- the potential η^* is a factor of 4000 larger than the base potential,
- the angular radius is equal to 4° ,
- it is located at $\theta_1 = -78^\circ, \varphi_1 = 260^\circ$, i.e. within the Southern polar cap;
- a large inactive spot on the opposite side of the cometary equator, such that:
 - the potential η^* is 0, which completely deactivates this area (regardless of the solar zenith angle z_\odot),
 - the angular radius is equal to 35° ,
 - it is located at $\theta_1 = +46^\circ, \varphi_1 = 260^\circ$;

whereas the (constant) gas temperature T was assumed to be of 40 K (see Biver et al. 2008). As the zero rotation phase α_0 we defined the rotation phase at the midpoint of our observations, that is Dec. 31.9951, 2007 UT. Consequently, a solar noon at that moment defined the prime meridian $\varphi_1 = 0^\circ$.

A fit of the model with these parameters resulted in $\xi = 1.31$. It is presented in Fig. 4.4. Moreover, in Fig. 4.5 we show an adaptive crosscut calculated for the spin axis orientation. It resembles the one in Fig. 4.3, except that now the right-hand side does not obey the previously-noticed symmetry. This is because the distribution of the sublimation potential $\eta^*(\theta_1, \varphi_1)$ was fixed this time, and the symmetry was created by its correlation with the spin axis orientation (if we change the axis longitude $\gamma \rightarrow \gamma + 180^\circ$, and transpose the potential distribution $\eta^*(\theta_1, \varphi_1) \rightarrow \eta^*(-\theta_1, \varphi_1 + 180^\circ)$ the spectrum will remain unchanged).

4.5.3 Discussion

The modeling revealed that the rotation period of 5.7 h is incapable of reproducing the observed line variability – in contrast to the one of 11.4 h.

The spin axis was practically in the model plane (i.e. the Sun–comet–observer plane; cf. Section 4.4.1), and the Earthward tilt was 68° . The new pole solution is hence only marginally inconsistent with the radar observations, and remains fairly consistent with the results from narrowband optical imaging of CN. Nevertheless, it is generally similar to the spin axis orientation obtained with a simpler parametrization of the sublimation potential, which is also evident upon comparing Figs. 4.5 and 4.3 in the “compatible” range of spin axis longitudes (i.e. between 0° and 180°). Therefore this parameter seems to be rather weakly sensitive to the “second-order” sublimating features, and hence should be fairly easily retrievable from microwave spectra using our model, at least in the geometry similar to that of comet Tuttle during our campaign.

The retrieved velocity of gas is comparable to the result obtained in a standard way, i.e. assuming an isotropic expansion. It is also the same as obtained by Biver et al. (2008) for this comet, and is consistent with the determinations for other comets around the same heliocentric distance (cf. Chapter 2.4.1; also e.g. Biver et al. 1999, 2002a); note, however, that all the cited results were obtained assuming an isotropic expansion, which potentially might have led to large errors (see Chapter 2.7.1.6). Bearing in mind the nucleus radius (cf. Section 4.1), the mean diurnal production rate should be considered as relatively low compared to other comets (cf. Chapter 2.4.3).

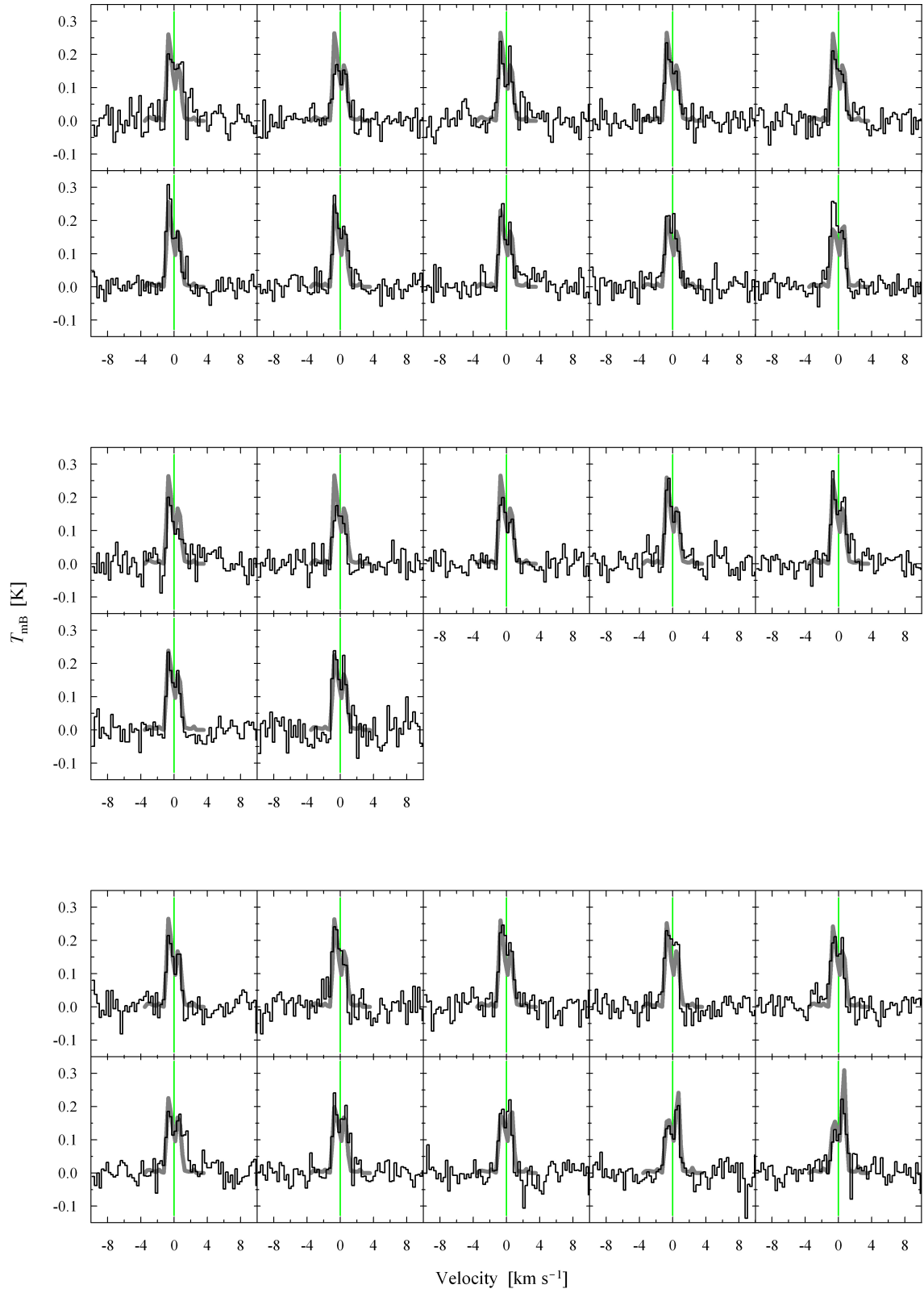


Figure 4.4: The same as Fig. 4.2, but with the best fit of the model (thick gray lines).

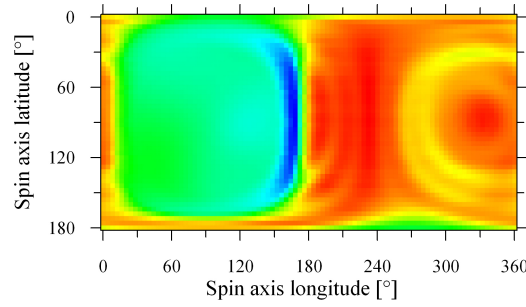


Figure 4.5: Adaptive crosscut illustrating the space of spin axis orientations (β, γ) , for the other free parameters fixed at their optimum values. Color scale extends from $\xi = 1.31$ for the best solution (*blue*) to $\xi = 2.86$ for the worst solution (*red*). The step size was 4° .

The inferred features in the distribution of the sublimation potential can be directly linked with the observed characteristics of the line profile. In the geometry of comet Tuttle, the base potential, producing maximum outgassing towards the Sun, created the blue component, whereas the red component was created by the Southern polar cap. The inversion of their intensities appeared at the rotation phases when the base sublimation was attenuated by the inactive spot and the sublimation from the Southern polar region further increased by the highly volatile vent. Although the fit quality is already only about 30% worse than the RMS noise in the spectra, it is clear that it could be further fine-tuned (even down to $\xi < 1$) by keeping on enriching the parametrization of the sublimation potential. However, it is important to understand that this property is very much model-dependent. It is used along with the concept of an activation function and the assumption of a spherical nucleus as a way of describing the directional distribution of gas density in the code. The closer the nucleus is to a plane sphere, the more physical distribution of the sublimation potential one will retrieve. But in the case of comet Tuttle this assumption is probably far from reality (see Section 4.1), hence the physical meaningfulness of this parameter is already problematic, and thus aiming at retrieving “higher-order” features would be pointless. On the plus side, the other parameters, including the spin axis orientation, are weakly sensitive to this ambiguity.

Nevertheless, the retrieved distribution of the sublimation potential can be interpreted as featuring two jets located opposite to each other in longitude. One is real, narrow, within the Southern polar cap, and the other is apparent, broad, caused by the volatile part of the nucleus at the longitudes opposite to those of the inactive spot. The middle-latitude location of the broad feature is consistent with the estimates by Woodney & Schleicher (priv. comm.) based on optical images of CN. However, the optical studies (see ref. in Section 4.1) revealed that it was the only variable feature within the coma, and that it was appearing every 5.7 h, which disagrees with our result. A possibility arises then, that perhaps the period was as long as 11.4 h and the circum-polar jet produced a similar feature, and altogether they created a coma pattern as would be created by a single feature rotating every 5.7 h. But this is only our speculation at the moment, and a subject of intensive investigations based on the results from both techniques (cf. Section 4.1). On the other hand, our conclusion that a substantial fraction of sublimation was independent of the nucleus rotation is consistent with the result by Waniak et al. (2009) who found that a large fraction of the CN coma was created from a steady-state anisotropic source.

4.6 Summary and conclusions

On three dates around the New Year's Day 2008 we obtained a time-series of the HCN spectra. The line profiles evolved with time in an organized manner, which we interpreted as stimulated by the nucleus rotation, and used to constrain the rotation period. Our estimates are consistent with the determinations from other techniques.

Since such effects have been reported for only a few comets before (one of them being our original contribution), it is important to rise a question why they are not observed routinely? Clearly, they can be best detected when the observation is limited to the inner coma only. However, using large microwave telescopes, which offer beam sizes of the order of $10''$, this is satisfied for comets already 0.5 AU from the Earth, which appear relatively frequently (cf. Chapter 6). We suspect that over years these effects were routinely averaged-out in hours- or even days-long effective exposures, aimed at providing the highest S/N. Alternatively, they could be missed when undersampled, if an observer aimed at detecting as many molecules as possible in a short time. The latter is well illustrated by comet Tuttle itself: Biver et al. (2008) detected several molecules but did not find any convincing indications for the short-term variabilities. Indeed, our observations have shown, that the signatures of rotation could have been very easily missed for this comet. This leads to a conclusion that careful arrangement of observations is critically important for such a study, and one should aim at obtaining the longest possible and undisturbed time-series. Unlike in night astronomy, this requirement can be easily satisfied by a single microwave facility, which can observe day and night, provided that the comet does not set below the local horizon.

In order to interpret the spectra we developed a new model of the spectral line profiles, which is a non-steady-state anisotropic construction. Upon being applied to our data it yielded the spin axis orientation and activity pattern of the nucleus. They are in general agreement with the results from other techniques, although they differ in details. To our best knowledge, the spin axis orientation has never been inferred from cometary spectra, and overall, the microwave line profiles have never been explored so extensively to date.

The model still leaves a large space for improvements. The spherical nucleus should be ideally replaced with a more accurate shape if known; it should be also modeled thermally to determine distributions of a sublimation temperature, velocity, and rate, removing the assumption of isotropy on the first two quantities. The coma should be ideally represented by a more accurate hydrodynamical or kinetic construction, which would predict radial profiles of the gas temperature and velocity, and the energy-levels population should be determined through a full time-dependent statistical equilibrium. For exceptionally active comets the assumption of optically thin lines should also be replaced with a full radiative transfer treatment, including determination of the energy-levels population. Indeed, to model cometary spectral line profiles we need a model of “everything”. Although single “pieces” have been developed by many authors over decades now, they are very complicated and computationally demanding on their own. For this reason, adopting and linking them all together into one self-consistent construction would be very difficult, and the state-of-the-art code would be most likely too slow to be used for a retrieval from observational data.

Also the technical side of the code can be further improved. When calculating the radial step, not only the rotation-stimulated gas density gradient should be considered,

but also those resulting from a beam sensitivity and photochemical lifetime; the former one may be dominant for very small beam sizes (e.g. a comet close to the Earth), and the latter for very short lifetimes (e.g. a comet close to the Sun). Fitting realized as a scan through the spaces of free parameters is good to roughly estimate their values, but then a general LSQ method with an adaptive step size for all the parameters should follow, to optimize the initial solution and retrieve the covariance matrix. We note, however, that the obtained errors would anyway be underestimated, as the free parameters are model dependent.

Also application of the model leaves a space for extensions. These include modeling observations taken at off-center positions (simple maps), and over a large arc on the sky (easily realized for Earth-approaching comets), which should greatly improve the robustness of retrieval. If applied to a long time series the model would be sensitive to distinguish a constant/accelerated and a simple/excited rotation of the nucleus. When applied to several parent molecules it could be used to verify if they originated from different reservoirs on the nucleus (chemical heterogeneity), or the same gas mixture was produced everywhere (chemical homogeneity).

5 Prospects for *in-situ* observations of 67P/Churyumov-Gerasimenko

5.1 Introduction

Rosetta (named after the *Rosetta Stone*) is a planetary mission of the European Space Agency¹ (Fig. 5.1). After its successful launch on Mar. 2, 2004, the spacecraft is on its way to comet 67P/Churyumov-Gerasimenko, which is the primary target of the mission. In the meantime it provides snapshot observations of planets and asteroids which are being passed by. *Rosetta* has a potential to become absolutely unprecedented in the history of exploration of comets. That is mainly because of two intended aspects of the mission: (i) landing on the nucleus, and (ii) long-term scientific activity. The spacecraft consists of two components: the *Philae* lander, and the orbiter, both densely packed with scientific instruments. It is worth stressing that *Rosetta* is not a sample-return mission, and all the scientific investigations will be carried out *in situ*.

67P/Churyumov-Gerasimenko is a Jupiter-Family comet discovered in 1969. It has a nucleus about 2 km in radius, rotating in a 13-h cycle. The comet shows clear seasonal effects, and features very asymmetric outgassing (asymmetric with respect to the perihelion point). Worth noticing is a particularly interesting history of its orbit: before 1840 the perihelion distance was at about 4.0 AU, then it reduced to 3.0 AU, and in 1959 further down to 1.3 AU, which actually made its discovery possible with the contemporary instruments. This means that the comet has been barely processed by the solar radiation, unless of course, it was closely approaching the Sun in some earlier episodes of its misty past. (This is unfortunately impossible to answer due to instability of the solutions for orbital motion in a complex system – such as the solar system. Cometary orbits are hence unavoidably chaotic, which manifests itself on sufficiently long timescales). Currently the comet is on a 6.5-year orbit. The most recent perihelion passage was in February/March 2009, and the next one will happen in August 2015, when the comet will be already accompanied by *Rosetta*.

The spacecraft will arrive at the comet in spring 2014. At that time Churyumov-Gerasimenko will be just emerging from the aphelion arc, hence its activity will be marginal. Subsequently, the orbiter will initiate continuous observations following the comet on its way towards the perihelion, and then until it will start falling into another “winter sleep”. It will provide a detailed portrait of the nucleus and its atmosphere from a variety of distances and viewing angles, and will trace their temporal evolution incessantly. These results will be supplemented by the contribution from the lander, which

¹<http://www.esa.int/esaMI/Rosetta>

Table 5.1: Timeline of the encounter with comet 67P/Churyumov-Gerasimenko.

Date	r^a [AU]	Mission objectives
Jan. → May, 2014	4.5 → 4.0	reactivation of the spacecraft; the distance and velocity between <i>Rosetta</i> and the comet gradually decrease
Aug., 2014	3.5	early characterization of the nucleus and selection of the landing site; the distance decreases from 200 to 25 km
Nov., 2014	3.0	<i>Philae</i> lands on the nucleus
Aug., 2015	1.2	perihelion
Dec., 2015	2.0	(happy) end of the mission

^aHeliocentric distance.

will operate for at least 65 h after the descent on a built-in battery, and perhaps for as long as 3 months on the solar panels. Timeline of the encounter is briefly summarized in Table 5.1.

An excellent overview on the mission and the comet can be found e.g. in Tubiana (2008). In this chapter we will focus on the potential science with MIRO – the Microwave Instrument for the Rosetta Orbiter (Fig. 5.2).

MIRO is a (sub-)millimeter telescope with a 30-cm antenna, capable of operating in two spectral regions: (i) the *millimeter* one at 190 GHz ($\lambda = 1.6$ mm), which is exclusively dedicated to observations of continuum emission, and (ii) the *submillimeter* one at 562 GHz ($\lambda = 0.5$ mm), which has two backends – a broadband continuum detector, and an ultra-high resolution Chirp-Transform Spectrometer (CTS) for line observations.

Focusing on spectral lines, the *submillimeter* instrument of MIRO consists of a double-sideband single-polarization heterodyne receiver, fixed-tuned to simultaneously observe six neutral molecular species: H_2^{16}O , H_2^{17}O , H_2^{18}O , CO, NH_3 , and CH_3OH . The receiver temperature is of about 3600 K, which corresponds to 2 K of RMS in 5 min for a raw double-sideband spectrum (cf. Chapter 1.2.4). At this frequency the half-power beam radius is equal to $3.6'$, that is about 25 m from a distance of 25 km. The total bandwidth of the CTS is equal to 180 MHz, and is divided into 4096 spectral channels. The resulting spectral resolution is equal to 44 kHz, which is 23.5 m s^{-1} , or equivalently $\nu/\Delta\nu = 12.8$ million, at the observed frequency. Such resolution is extremely high, and is the key feature which gives MIRO a great potential in studying the properties of molecular coma. The instrument offers a frequency-switching mode only, the greatest advantage of which is a complete lack of any moving parts which are always first to fail. In addition, any offset-position-based switching mode would be useless while observing from *inside* the source itself!

The technical specifications and intended scientific outcome are presented in details by Gulkis et al. (2007).

The immediate goal of this work is to simulate how the lines observed by MIRO will look like. Interesting on its own, this will also be the starting point for further studies, aimed at verification which physical information about the comet can actually be retrieved and with which accuracy. Ultimately, this will be used to optimize the observing strategies for *Rosetta* from the point of view of the science with MIRO.

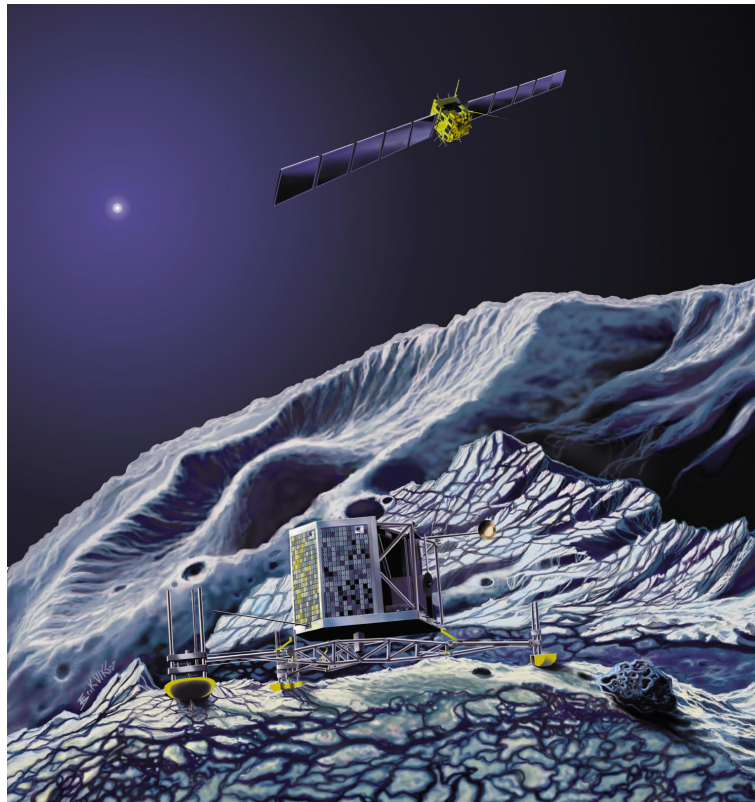


Figure 5.1: Artistic vision of the *Rosetta* orbiter and lander. ©ESA

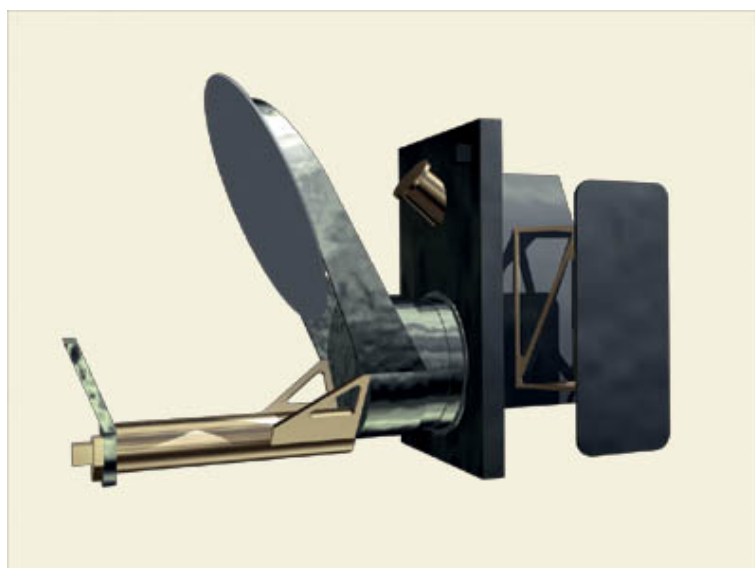


Figure 5.2: The MIRO instrument. ©ESA

5.2 Simulations

We tackled this problem by combining various (preexisting) models of the cometary coma – some of them having been designed exclusively for comet Churyumov-Gerasimenko – with (also preexisting) a general-purpose code for simulating microwave spectral lines in LTE environment. We investigated mainly two problems: (i) detectability of the lines already at the arrival of *Rosetta*, and (ii) distinguishability of the different coma models in the MIRO spectra. In this work we focus on the water molecule, which takes the lion's share as a constituent of the cometary ice; more precisely, we investigate H_2^{16}O , which is by far its most abundant isotope (e.g. Rothman et al. 2005).

5.2.1 Models

We used outputs from three different physical models of the coma of comet Churyumov-Gerasimenko. (By a physical model of a coma we mean a construction which provides the spatial profiles of density, temperature, and velocity vector of the element(s) of interest – that is of H_2^{16}O in the studied case.) The outputs of the models were calculated for the moment of *Rosetta*'s arrival at the comet. Below we present each of them in a nutshell (details can be found under references). We do not, however, analyze and discuss their strong and weak points, which would be far beyond the scope of this work.

- *The model of Haser (1957)*. A classical steady-state isotropic model which includes photodissociation. We adopted a constant H_2^{16}O production rate of 2.5×10^{26} molec s^{-1} , a constant expansion velocity of 0.5 km s^{-1} , and a constant temperature of 20 K. Steady-state isotropy is guaranteed by the assumption of a plane uniformly-volatile spherical nucleus which sublimates independently of insolation.
- *The model of Crifo et al. (2004)*. An anisotropic hydrodynamical steady-state model. It adopts the nucleus shape from Lamy et al. (2006), though treats it as a non-rotator. The nucleus is thermally-modeled in a grid of cells. This is a baseline for calculating sublimation fluxes in the cells, and ultimately, modeling the entire coma. The total production rate of water has been normalized to 2.5×10^{26} molec s^{-1} . The output of this model was kindly made available to us by V. V. Zakharov, who also provided us with an extensive support in its implementation.
- *The model of Tennishev et al. (2008)*. An anisotropic kinetic steady-state model, where the Boltzmann equation is solved using the direct simulation Monte Carlo method. The nucleus is represented by a uniformly-volatile plane sphere of 2 km in radius, which is modeled thermally using the approach of Davidsson & Gutiérrez (2004, 2005, 2006). The day and night sides are tackled inconsistently: for the day side the spin-axis is assumed to be directed towards the Sun, which ensures a steady state (no rotation-induced time-dependent effects); for the night side average conditions for a rotating nucleus with the spin axis oriented normal to the orbit plane have been used (which also ensures a steady state). The production rate of water from the entire surface has been normalized to 1.0×10^{24} molec s^{-1} , which is a factor of 250 less than adopted in the two other models. This inconsistency partly results from a bit greater heliocentric distance assumed for the beginning of

scientific operations of *Rosetta* (3.25 AU assumed here vs. 3.0 AU before). The output of the model is made freely available online² (also for other heliocentric distances) through the Inner Coma Environment Simulator.

Each of these three models supplied the code for simulating microwave spectral lines by Jarchow & Hartogh (2005). It calculates molecular emissions assuming the Boltzmann distribution of the energy-levels, and taking the transition parameters from the JPL spectral line catalog (Pickett et al. 1998)³. Propagation of the radiation intensity along the line of sight (cf. Chapter 1.3) is calculated individually for each frequency channel by integrating the differential radiative-transfer equation using the Runge-Kutta method with an adaptive step-size control (e.g. Press et al. 1992). Note that the assumption of LTE is absolutely natural for simulating observations of the inner coma (Bockelée-Morvan, priv. comm.), and has been commonly used for similar studies (e.g. Zakharov et al. 2008). The integration is performed only along one ray (a *pencil* beam); though this simplification could be easily replaced with an integration over the actual beam pattern, it has a negligible influence for the spectra in the great bulk of observing geometries planned for *Rosetta* (Bockelée-Morvan, priv. comm.).

5.2.2 Observing geometries

We investigated two observing geometries, when: (i) *Rosetta* is “looking” towards the nucleus center (*nadir* direction), and (ii) opposite to the nucleus center (*zenith* direction). In each case we separately analyzed the situation when: (i) *Rosetta* is located 25 km from the nucleus, and (ii) 100 km from the nucleus. All the simulations were consequently calculated along the same axis, as illustrated in Fig. 5.3.

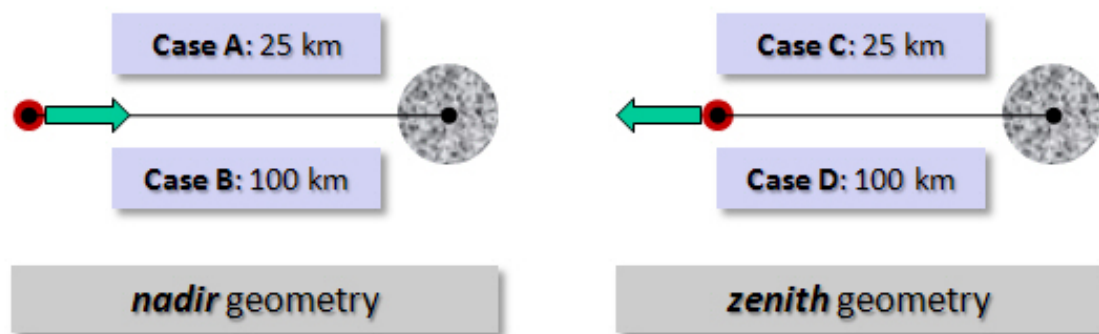


Figure 5.3: Illustration of the investigated geometries.

5.3 Results

The obtained results are presented in Figs. 5.4 and 5.5.

²http://csem.engin.umich.edu/ISSI_Comet/ICES/

³Available online at <http://spec.jpl.nasa.gov/>

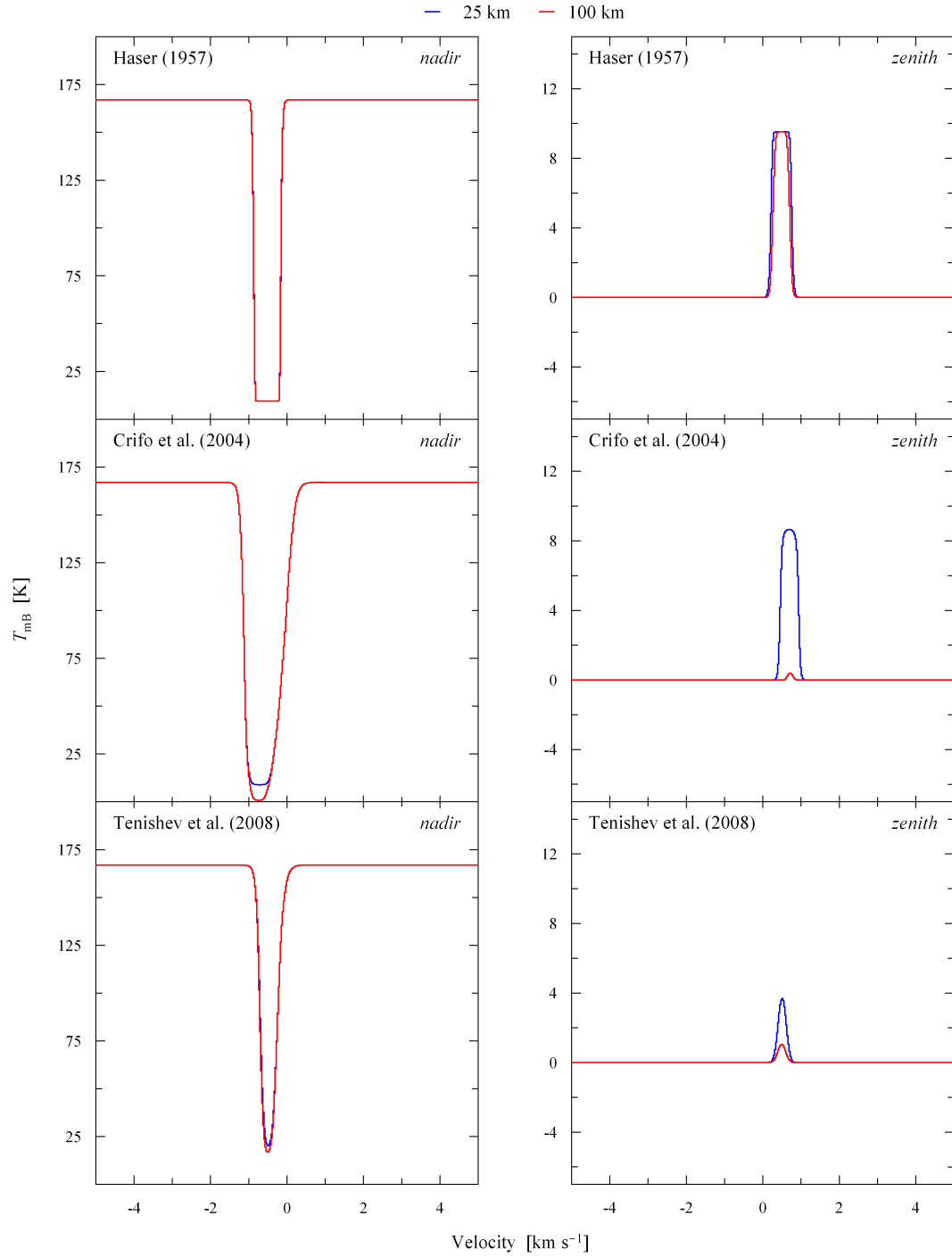


Figure 5.4: Simulated single-sideband spectra of the H₂O line at 556.9 GHz.

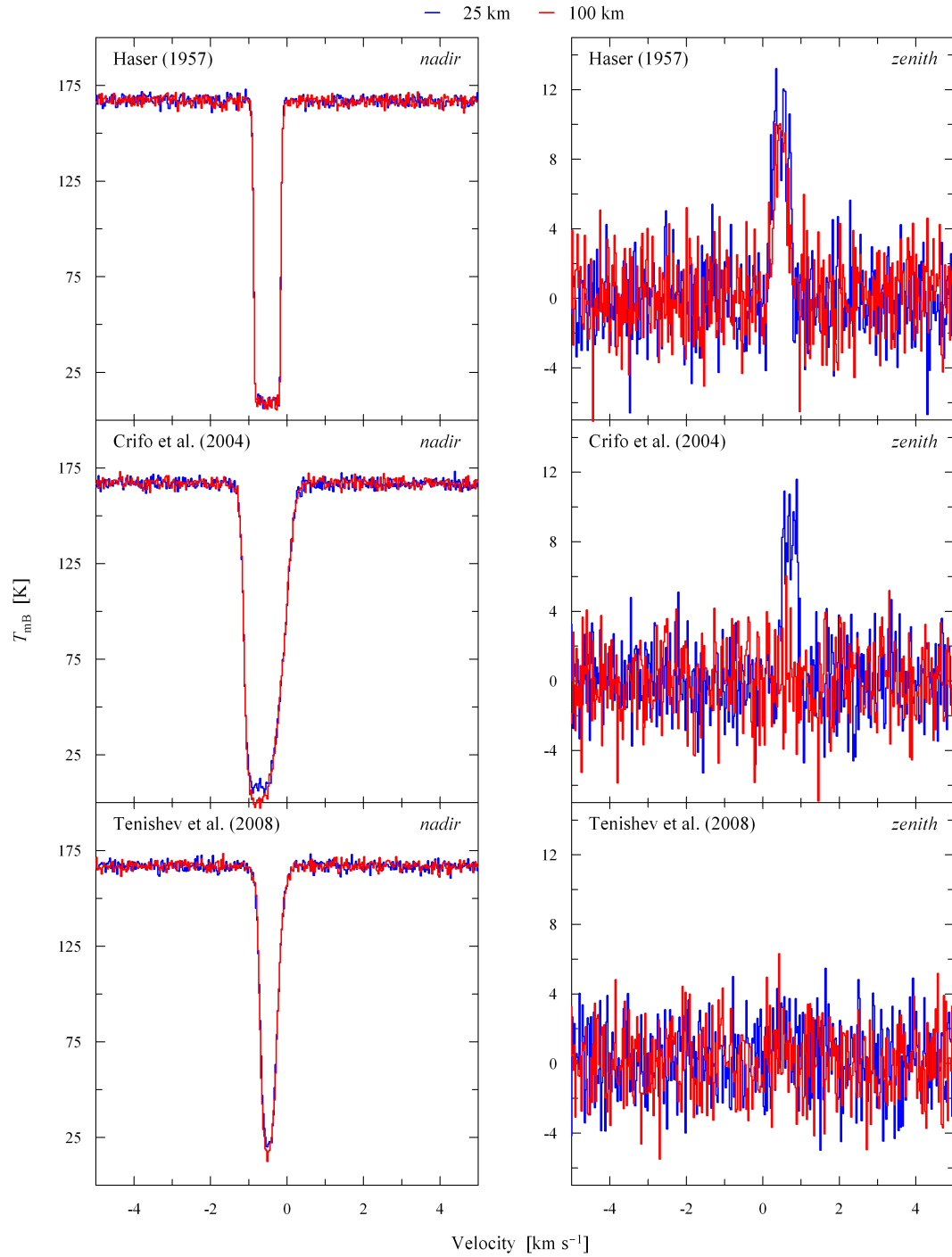


Figure 5.5: The same as in Fig. 5.4, except for a realistic observing noise of 2 K for a 5-min exposure.

5.4 Discussion and conclusions

Let us first analyze the basic properties of the spectra.

Those taken at *nadir* feature a brightness-temperature continuum level controlled by the nucleus surface (about 180 K), and those taken at *zenith* have a continuum from the 2.7-K cosmic microwave background. Note that conversion from the physical temperature to the Rayleigh-Jeans brightness temperature, which is an intrinsic part of the definition of antenna temperature (see Chapter 1.2), decreases the observed continuum levels, and actually makes the 2.7-K one invisible.

Since the gas temperature is generally locked in between the two continuum levels, depending on a viewing direction MIRO will observe either emission or absorption lines. In principle however, parent coma can be heated-up above the nucleus temperature due to collisions with highly-energetic photodissociation products such as neutral hydrogen (see e.g. Combi et al. 2004). The photolytic heating is, however, extremely inefficient at large distances from the Sun, where the nucleus activity is low, because it requires a strong source of atoms and radicals to efficiently maintain the process. For this reason, the parent molecules – once ejected from the nucleus of comet Churyumov-Gerasimenko (at least at about 3 AU) – will progressively cool down.

In both of the viewing directions the position of line is fully controlled by the radial component of the global gas-flow velocity (note that in the isotropic model of Haser this is equal to the coma expansion velocity). It is therefore perfectly understandable why the line is blue-shifted when observed towards the nucleus and red-shifted when observed in the opposite direction. The line width is controlled by the dispersion of this velocity along the line of sight, and, more importantly, by the kinetic temperature of gas (e.g. the Haser model gives no velocity dispersion in the investigated geometries though the line is still broad).

Optical opacity manifests itself by equalizing the line brightness temperature with the temperature of gas (at the frequencies at which it is optically thick). This is perfectly illustrated by the simulations for the Haser model. If the temperature varies along the line of sight (case of the other two models), the brightness temperature from more distant regions is attenuated by closer regions which consequently contribute their own brightness temperature with a greater weight. This effect is a natural consequence of the properties of radiative transfer, and will be easily distinguishable in the MIRO data.

In the early-most phase of the encounter the *nadir* direction will be by far the most reasonable choice, as it will secure detection of the line, and simultaneously provide a precise diagnostics of the nucleus surface temperature. Worth noticing is that it will not really matter from which distance the comet will be observed at that direction, since the great bulk of the molecules will be anyway close to the nucleus, and they will be the main source of the observed brightness temperature.

As to whether or not it will make sense to point *Rosetta* in the opposite direction in this early phase will depend on which of the coma models will turn out to be closest to reality. We note that the line resulting from the model of Tennishev et al. (2008) would certainly disappear in the observing noise, and also the line from the model of Crifo et al. (2004) would be below the detection threshold if observed from a distance significantly greater than 25 km. We also note that the difference in the line brightness temperature between these two models, though significant, is still much smaller than the one intuitively

suggested by the factor-of-250 difference in the assumed production rate (Section 5.2.1). Indeed, for identical temperature and velocity profiles the line intensity would differ by the same amount, but only if being optically thin. Otherwise, line's self-absorption, resulting from basic properties of the radiative transfer, significantly reduces this difference. Consequently, brightness temperature of the lines observed by MIRO will be controlled by the gas temperature, and the production rate will be of a marginal importance, as long as the number of produced molecules will be sufficient for the lines to become optically thick.

Summarizing, we note that the optically-thick lines observed from inside the cometary coma will feature noticeably different properties than optically-thin lines commonly observed from ground. For this reason intuition developed by modeling the latter cannot be readily used to predict the properties of the lines observed by MIRO, and the only appropriate approach to get prepared for science with this instrument is an adequate modeling with full radiative-transfer treatment. Our state-of-the-art line simulator for comet Churyumov-Gerasimenko can be now easily used for investigation of other observing geometries or lines from another molecules.

6 Outlook

My Ph.D. research, carried out with the techniques of microwave spectroscopy, provided me with outstanding opportunities to realize my passion for comets. I was given a chance to observe the fragments of split comet 73P/Schwassmann-Wachmann 3, I had the privilege to investigate the remarkable explosion of comet 17P/Holmes, and finally, I took the opportunity of observing a “textbook” comet 8P/Tuttle – which eventually turned out to be much more than just a textbook one. Overall, I investigated most of the spectacular and unusual comets that visited the skies in that time.

Starting from scratch I developed a model dedicated to interpretation of the cometary observations. In its simplest version it was applied to the first observed comet, followed by a detailed justification of its validity. Ultimately, the model evolved into a highly-specialized tool, which enables exploration of cometary spectra at unprecedented depth, which is demonstrated by its application to the data of comet Tuttle. Currently, the model can perform well only on the spectra of “standard” comets, and it still leaves space for important improvements.

These studies were supplemented with a modest contribution to the optimization of observing strategies for the *Rosetta* mission, and the preparation for analysis of the future data. My task was to merge the already-existing models of cometary coma and radiative transfer into one easy-to-use tool, and explore the properties of the simulated spectral lines.

Altogether, my Ph.D. research characterizes three objects, contributes to the methodology of cometary investigations, and supports the preparation for science with *Rosetta*. It also constitutes a solid basis for novel studies on comets in the future. Below I present and discuss in depth one example of a potentially valuable project.

Example of a project arising from the thesis research

Scientific background

One of the most fundamental cosmogonic questions is *when and how did the elements of life in the Universe arise?* A possible approach to this problem is to understand how the final elements essential for life appeared on Earth, and trace their history throughout the Universe back to the moment of creation. Focusing on water, the starting point is to identify its sources and sinks, and transportation mechanisms in the Solar System.

Comets are known sources of water ice. As noted in Section 1.1, they are grouped in three distinct reservoirs, connected to different formation regions in the protosolar nebula: the Oort Cloud (formation in the outer planets’ region and subsequent ejection to the pe-

ripheries of the Solar System), the Kuiper Belt (just beyond the orbit of Neptune), and the Main Belt (between the orbits of Mars and Jupiter). The non-periodic, long-period, and Halley-Family comets originate from the Oort Cloud, the Jupiter-Family Comets (JFCs) escaped from the Kuiper Belt, whereas the recently discovered active asteroids are located where they formed: in the Main Belt.

To uncover the picture of water migration in the Solar System it is essential to understand the natural lifetime of comets as water carriers. They decay through collisions, complete evaporation, disintegration, deactivation, and tidal disruptions, the least understood process being, however, spontaneous fragmentation, which often leads to complete destruction. One explanation proposed for the latter is *rotational break-up*, saying that the nucleus must split into pieces when the centrifugal force surpasses its self-gravity and material strength (see e.g. Davidsson 1999, 2001, for an up to date theoretical treatment of this problem). However, it was neither clearly verified by observations (though indications exist, see Chapter 2.6, and e.g. Toth & Lisse 2006), nor do we have any idea how efficient it is for different classes of comets.

Current status of the research field

Rotational break-up may happen only when the nucleus is spinning up. Theoretical studies show, that the spin-up process can be produced by non-radial emission of gas, and it can substantially change the rotation period in the time-scale of only one perihelion passage (see e.g. Gutiérrez et al. 2002). Therefore, this scenario is possible for all classes of comets. With this regard, lifetime of an individual nucleus depends, however, on its size, shape, density, and tensile strength, gas sublimation rate and velocity, and the scaling factor S , that is the fraction of an effective jet force which exerts a torque on the nucleus (Drahus & Waniak 2006, see also Chapter 2.7.3.2).

Recent observations of some comets indeed suggest spin-up (or -down) of their nuclei (see e.g. Drahus & Waniak 2006, and references therein), but the results are mostly uncertain. Only 9P/Tempel 1 (JFC) is confirmed to be spinning up (Belton & Drahus 2007, Belton et al. 2009), and it is also the only one for which parameter S was robustly determined (cf. Chapter 2.7.3.2). It is equal to 1.5%, which means, that if the whole gas was sublimating from a point-like source on the equator, the measured spin-up would be consistent with sublimation through a jet tilted by less than 1° with respect to the radial direction! Such efficiency is extremely low, a factor of 20 lower from what Drahus & Waniak (2006) expected for a typical comet, which raises questions. First of all, is there any physical process which may minimize this efficiency, by e.g., aligning jets with the radial direction and/or stimulating formation of such an activity pattern that torques cancel out? If such process exists, can we identify it? Can we find its intrinsic time-scales, and thus understand if it works for the short-period comets only, or for the long-period and non-periodic ones too? If it does not, such difference would differentiate lifetimes of comets from these groups tremendously! Finally, if this hypothetical process does not exist at all, does it mean that these >200 short-period comets that we know are only few lucky survivals from much larger population? If so, their lifetime is much shorter than suggested by the break-up statistics, and the transfer rate from their reservoirs is much higher than expected, simply because many of them must die shortly after being captured yet before being actually discovered.

Specific aims and methods

I propose to carry out a small-sample survey of periodic and non-periodic comets, aimed at determining their angular accelerations and activity patterns. The former parameter is a proxy of lifetime, considering rotational break-up as the primary destruction process. The latter property will be used to calculate jet forces exerted on the nucleus, and hence model the angular acceleration, providing an unambiguous interpretation of the direct measurements.

This study will utilize the two codes and techniques I developed during my M.S. and Ph.D. studies, that is: modeling the spectra of molecular coma, which provides wealth of information about the nucleus, including its spin state and activity pattern (Section 4), and the dynamical periodicity-search routines, which were created to directly determine the rotation period and acceleration (Drahus & Waniak 2006). Maximum scientific outcome will be achieved upon merging these two codes and techniques, such that spectral observations will serve as the input data for direct calculation of the angular acceleration, simultaneously with retrieval of the activity pattern. Since mm-waves spectra of comets have never been explored so deeply before, this program requires a pilot study of the state-of-the-art algorithm and carefully selected targets.

Feasibility of this program

A successful retrieval of the activity pattern sets the highest demands for the data quality: spectral resolution above 10^6 , S/N above 10, individual exposure below 30 min, and half-power beam radius below 4000 km. The former two requirements guarantee sufficiently good spectra, whereas the latter two ensure that the signal in individual spectra originates from the molecules emitted at similar phases of the nucleus rotation; otherwise, influence of the rotation on the line shape, which is crucial for a successful retrieval, may be smoothed out, unless the rotation period is unusually long.

Comets approaching the Earth at 0.4 AU with a total visual brightness of 6 mag marginally satisfy these conditions when a modern 10-m ground-based (sub-) millimeter telescope is used. An additional requirement is set for a successful detection of the angular acceleration. Assuming $S = 1\%$ and typical properties of the nucleus, the observations will be sensitive to this quantity only if the time-span is longer than a week for a body measuring 2 km across, and a month for a 10-km object. This is a substantial amount of observing time, however, it is definitely feasible, as the Earth-approaching comets usually stay sufficiently close and bright for several weeks.

An obvious candidate for this study is 103P/Hartley 2 (JFC), which will approach the Earth at 0.12 AU in October 2010. At the same time the comet will reach the naked-eye visibility at 5 mag, and it will produce enough gas (A'Hearn et al. 1995) to meet the strict requirements given before. Using my model I generated examples of spectra for this comet, and performed a retrieval calculation, which are presented in Fig. 6.1. Staying within 0.4 AU from the Earth for almost 4 months, and measuring only about 1.5 km across (Groussin et al. 2004), comet Hartley 2 will provide an opportunity to determine the angular acceleration with an unprecedented accuracy. In addition, the postulated sample will include non-periodic and/or long-period comets, which, based on the discovery statistics (Table 6.1), will amount to one comet per year on average.

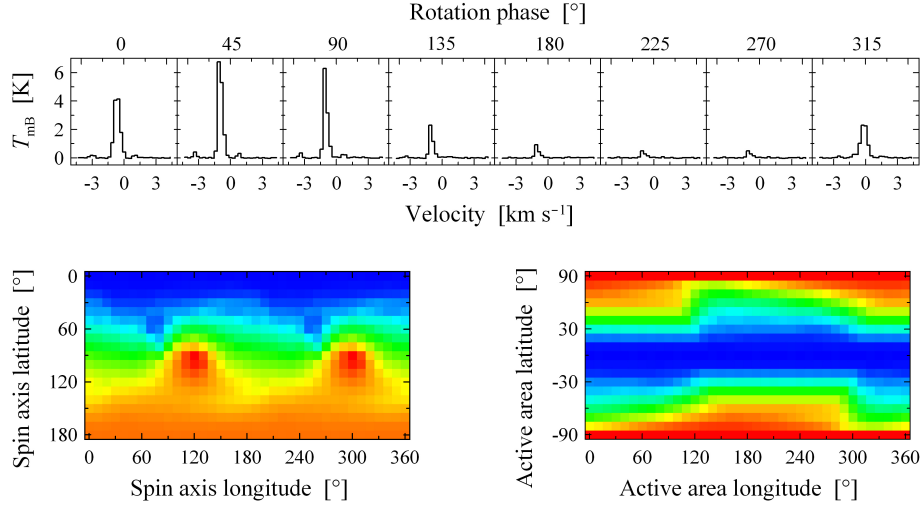


Figure 6.1: *Top panels* show examples of simulated spectra generated with my code for comet 103P/Hartley 2. They were calculated with realistic observing noise, for realistic physical properties and conditions, assuming a spin axis perpendicular to the Sun–comet–observer plane, and a single active region located at the nucleus’ equator. *Bottom panels* show retrieval of these parameters, where blue indicates the best solutions. The spin axis longitude is undefined for the assumed latitude which causes the apparent uncertainty of the active area longitude. Nevertheless, it is clearly visible that these parameters can be easily retrieved for this comet.

Table 6.1: List of comets which could have been studied in the proposed way since January 2000 (originally compiled by Piotr Guzik).

Comet	Type ^a	Discovery date	Earth approach			Δt ^b [day]
			date	Δ [AU]	mag	
C/1999 S4 (LINEAR)	NPC	Sep. 27, 1999	Jul. 22, 2000	0.37	6.0	299
C/2001 A2 (LINEAR)	NPC	Jan. 3, 2001	Jun. 30, 2001	0.24	4.5	178
C/2000 WM ₁ (LINEAR)	NPC	Nov. 16, 2000	Dec. 2, 2001	0.32	5.5	381
153P/Ikeya-Zhang	LPC	Feb. 1, 2001	Apr. 29, 2002	0.40	4.5	452
C/2002 O6 (SWAN)	NPC	Jul. 25, 2002	Aug. 8, 2002	0.26	6.0	14
C/2002 T7 (LINEAR)	NPC	Oct. 14, 2002	May 19, 2004	0.27	3.0	583
C/2001 Q4 (NEAT)	NPC	Aug. 24, 2001	May 6, 2004	0.32	3.0	986
C/2004 Q2 (Machholz)	NPC	Aug. 27, 2004	Jan. 5, 2005	0.35	3.5	131
73P-C/Schwass.-Wachmann 3	JFC	May 2, 1930	May 12, 2006	0.08	6.0	—
73P-B/Schwass.-Wachmann 3	JFC	Dec. 12, 1995	May 14, 2006	0.07	5.5	—
8P/Tuttle	HFC	Jan. 5, 1858	Jan. 1, 2008	0.25	6.0	—

^aNPC = non-periodic comet, LPC = long-period comet, JFC = Jupiter-family comet, HFC = Halley-family comet.

^bTime interval between the discovery and the closest approach to the Earth (meaningful only for NPCs and LPCs); the mean value is equal to 378 days, and one comet per year on average is expected from these groups.

Closing remarks

I propose to carry out a small-sample survey of periodic and non-periodic comets, utilizing mm-waves spectroscopy. Detailed modeling of the spectral lines, using the novel techniques I have developed, will address the problem of lifetime of cometary nuclei, which may challenge our current paradigms. Being relevant to the fundamental question about origin of the elements of life, this program additionally addresses interesting problems specific to cometary science. For example, it will resolve whether different active areas consist of different ices, or they all consist of the same mixture. Moreover, observations will probe physical conditions in the coma, and yield its molecular composition, enabling taxonomic classification of the observed objects. The program is shown to be feasible: comet 103P/Hartley 2 is an excellent first target, and a couple more good candidates are expected. There is also an important context regarding comet 103P/Hartley 2 itself: it is the target of NASA's Epoxi mission (encounter in November 2010), and it will be widely observed by the Cosmic Origins space flotilla and best ground-based telescopes. In this respect, my program offers a chance for a significant contribution to the overall campaign, and vice versa. The practical implication becomes obvious when bearing in mind comet 85P/Boethin, the former target of Epoxi, which has unexpectedly disappeared. Last but not least, this is a pathfinder for future large-sample surveys, utilizing the next generation of submillimeter telescopes, such as ALMA and LMT. These new instruments will push the observing limits far beyond the current limitations, allowing to carry out a cutting-edge research for several comets per year.

Bibliography

- A'Hearn, M. F., Dwek, E., & Tokunaga, A. T. 1981, *Astrophys. J.*, **248**, L147
- A'Hearn, M. F., Millis, R. L., Schleicher, D. G., Osip, D. J., & Birch, P. V. 1995, *Icarus*, **118**, 223
- A'Hearn, M. F., Belton, M. J. S., Delamere, W. A., et al. 2005, *Science*, **310**, 258
- Altenhoff, W. J., Baars, J. W. M., Wink, J. E., & Downes, D. 1987, *Astron. Astrophys.*, **184**, 381
- Baars, J. W. M., & Martin, R. N. 1996, *Rev. Mod. Astr.*, **9**, 111
- Baars, J. W. M., Martin, R. N., Mangum, J. G., McMullin, J. P., & Peters, W. L. 1999, *Publ. Amer. Soc. Pac.*, **111**, 627
- Belton, M. J., & Drahus, M. 2007, *Bull. Amer. Astron. Soc.*, **39**, 498
- Belton, M. J., Meech, K. J., A'Hearn, M. F., et al. 2005, *Space Sci. Rev.*, **117**, 137
- Belton, M. J., Meech, K. J., A'Hearn, M. F., et al. 2009, *Icarus*, submitted
- Biver, N., Bockelée-Morvan, D., Crovisier, J., et al. 1999, *Astron. J.*, **118**, 1850
- Biver, N., Bockelée-Morvan, D., Colom, P., et al. 2002a, *Earth, Moon, Planets*, **90**, 5
- Biver, N., Bockelée-Morvan, D., Crovisier, J., et al. 2002b, *Earth, Moon, Planets*, **90**, 323
- Biver, N., Bockelée-Morvan, D., Boissier, J., et al. 2007, *Icarus*, **187**, 253
- Biver, N., Lis, D. C., Fray, N., et al. 2008, *Lun. Planet. Inst. Conf.*, **1405**, 8151
- Biver, N., Bockelée-Morvan, D., Colom, P., et al. 2009, *Astron. Astrophys.* (accepted)
- Bockelée-Morvan, D., & Crovisier, J. 1985, *Astron. Astrophys.*, **151**, 90
- Bockelée-Morvan, D., & Crovisier, J. 1987, The role of water in the thermal balance of the coma, in *Proceedings of the Symposium on the Diversity and Similarity of Comets*, ed. E. J. Rolfe & B. Battrick (ESA SP-278, Noordwijk, The Netherlands), 235
- Bockelée-Morvan, D., Crovisier, J., Baudry, A., et al. 1984, *Astron. Astrophys.*, **141**, 411
- Bockelée-Morvan, D., Crovisier, J., Colom, P., & Despois, D. 1994, *Astron. Astrophys.*, **287**, 647

- Bockelée-Morvan, D., Padman, R., Davies, J. K., & Crovisier, J. 1994, *Planet. Space Sci.*, **42**, 655
- Bockelée-Morvan, D., Biver, N., Moreno, R., et al. 2001, *Science*, **292**, 1339
- Bockelée-Morvan, D., Crovisier, J., Mumma, M. J., & Weaver, H. A. 2004, The Composition of Cometary Volatiles, in *Comets II*, ed. M. C. Festou, H. U. Keller & H. A. Weaver (Tucson: Univ. of Arizona press), 391
- Bockelée-Morvan, D., Biver, N., Colom, P., et al. 2004b, *Icarus*, **167**, 113
- Boehnhardt, H. 2004, Split Comets, in *Comets II*, ed. M. C. Festou, H. U. Keller & H. A. Weaver (Tucson: Univ. of Arizona press), 301
- Boehnhardt, H., & Kaufl, H. U. 1995, *IAU Circ.*, 6274
- Boissier, J., Bockelée-Morvan, D., Biver, N., et al. 2007, *Astron. Astrophys.*, **475**, 1131
- Bonev, B. P., Mumma, M. J., Radeva, Y. L. et al. 2008, *Astrophys. J.* **680**, 61
- Borisov, G., Waniak, W., Bonev, T., Czart, K., & Drahus, M. 2008, *Bulg. Astron. J.*, **10**, 59
- Buzzi, L., Muler, G., Kidger, M., et al. 2007, *IAU Circ.*, 8886
- Campins, H., Rieke, G. H., & Lebofsky, M. J. 1982, *Icarus*, **51**, 461
- Capria, M. T., de Sanctis, M. C., & Cremonese, G. 2008, *Lun. Planet. Inst. Conf.*, **1405**, 8117
- Cochran, A. L. 1985, *Astrophys. J.*, **289**, 388
- Cochran, A. L. 1985, *Astron. J.*, **90**, 2609
- Combi, M. R., Harris, W. M., & Smyth, W. H. 2004, Gas dynamics and kinetics in the cometary coma: theory and observations, in *Comets II*, ed. M. C. Festou, H. U. Keller & H. A. Weaver (Tucson: Univ. of Arizona press), 523
- Crifo, J. F., Lukyanov, G. A., Zakharov, V. V., & Rodionov, A. V. 2004, Physical model of the coma of comet 67P/Churyumov-Gerasimenko, in *The New Rosetta Targets. Observations, Simulations and Instrument Performances.*, ed. L. Colangeli, E. M. Epifani, & P. Palumbo (Dordrecht: Kluwer), 119
- Crovisier, J. 1985, *Astron. J.*, **90**, 670
- Crovisier, J., Biver, N., Bockelée-Morvan, D., et al. 1995, *IAU Circ.*, 6227
- Davidsson, B. J. R. 1999, *Icarus*, **142**, 525
- Davidsson, B. J. R. 2001, *Icarus*, **149**, 375
- Davidsson, B. J. R., & Gutiérrez, P. J. 2004, *Icarus*, **168**, 392

- Davidsson, B. J. R., & Gutiérrez, P. J. 2005, *Icarus*, **176**, 453
- Davidsson, B. J. R., & Gutiérrez, P. J. 2006, *Icarus*, **180**, 224
- Dello Russo, N., Vervack, R. J., Weaver, H. A., et al. 2007, *Nature*, **448**, 172
- Dones, L., Weissman, P. R., Levison, H. F., & Duncan, M. J. 2004, Oort cloud formation and dynamics, in *Comets II*, ed. M. C. Festou, H. U. Keller & H. A. Weaver (Tucson: Univ. of Arizona press), 153
- Drahus, M., & Waniak, W. 2006, *Icarus*, **185**, 544
- Drahus, M., Paganini, L., Ziurys, L., et al. 2007, *IAU Circ.*, 8891 (Corrigendum: *IAU Circ.*, 8914)
- Drahus, M., Paganini, L., Ziurys, L., & Peters, W. 2008, *Cent. Bureau Elect. Telegram*, 1289
- Drahus, M., Jarchow, C., Hartogh, P., et al. 2008b. *Cent. Bureau Elect. Telegram*, 1294.
- Drahus, M., Jarchow, C., Hartogh, P., et al. 2008c. *Lun. Planet. Inst. Conf.*, **1405**, 8334.
- Drahus, M., Paganini, L., Ziurys, L. M., et al. 2008, *Lun. Planet. Inst. Conf.*, **1405**, 8340
- Drahus, M., Küppers, M., Jarchow, C., et al. 2009, *Astron. Astrophys.* (accepted)
- Duncan, M., Levison, H. & Dones, L. 2004, Dynamical evolution of ecliptic comets, in *Comets II*, ed. M. C. Festou, H. U. Keller & H. A. Weaver (Tucson: Univ. of Arizona press), 193
- Efroimsky, M. 2001, *Planet. Space Sci.*, **49**, 937
- Farnham, T. L. 2001, *Bull. Amer. Astron. Soc.*, **33**, 1047
- Feaga, L. M., A'Hearn, M. F., Sunshine, J. M., Groussin, O., & Farnham, T. L. 2007, *Icarus*, **191**, 134
- Festou, M. C., Feldman, P. D., & Weaver, H. A. 1982, *Astrophys. J.*, **256**, 331
- Fray, N., Bénilan, Y., Cottin, H., Gazeau, M.-C., & Crovisier, J. 2005, *Planet. Space Sci.*, **53**, 1243
- Groussin, O., Lamy, P., Jorda, L., & Toth, I. 2004, *Astron. Astrophys.*, **419**, 375
- Gulkis, S., Frerking, M., Crovisier, J., et al. 2007, *Space Sci. Rev.*, **128**, 561
- Gutiérrez, P. J., Ortiz, J. L., Rodrigo, R., & López-Moreno, J. J. 2000, *Astron. Astrophys.*, **355**, 809
- Gutiérrez, P. J., Ortiz, J. L., Rodrigo, R., López-Moreno, J. J., & Jorda, L. 2002, *Earth, Moon, Planets*, **90**, 239
- Hale, A., Kobayashi, J., & Morris, C. S. 1995, *IAU Circ.*, 6234

- Harmon, J. K., Nolan, M. C., Howell, E. S., & Giorgini, J. D. 2008, *Lun. Planet. Inst. Conf.*, **1405**, 8025
- Harmon, John K., Nolan, M. C., Howell, E. S., Giorgini, J. D., & Magri, C. 2008, *Bull. Amer. Astron. Soc.*, **40**, 393
- Haser, L. 1957, *Bull. Acad. R. Sci. Liege*, **43**, 740
- Henry, F. 2003, *La comète Hale-Bopp à l'interféromètre du Plateau du Bure: étude de la distribution du monoxyde de carbone*, Ph.D. thesis, l'Observatoire de Paris
- Henry, F., Bockelée-Morvan, D., Crovisier, J., & Wink, J. 2002, *Earth, Moon, Planets*, **90**, 57
- Hsieh, H. H., & Jewitt, D. 2006, *Science*, **312**, 561
- Hsieh, H. H., Fitzsimmons, A., & Pollacco, D. L. 2007, *IAU Circ.*, 8897
- Hu, H-Y, Larson, H. P., & Hsieh, K. C. 1991, *Icarus*, **91**, 238
- Huebner, W. F., Keady, J. J., & Lyon, S. P. 1992, *Astrophys. Space Sci.*, **195**, 1
- Ip, W.-H., Fink, U., & Johnson, J. R. 1985, *Astrophys. J.*, **293**, 609
- Jarchow, C. 1998, *Bestimmung atmosphärischer Wasserdampf- und Ozonprofile mittels bodengebundener Millimeterwellen-Fernerkundung*, Ph.D. thesis, Universität Bremen
- Jarchow, C. & Hartogh, P. 2005, *Bull. Amer. Astron. Soc.*, **37**, 646
- Jewell, P. R. & Mangum, J. G. 1999, *Int. Journal of Millimeter and Infrared Waves*, **20**, 171
- Jewitt, D. 1999, *Earth, Moon, Planets*, **79**, 35
- Johnson, J. R., Fink, U., & Larson, S. M. 1984, *Icarus*, **60**, 351
- Jorda, L., & Gutiérrez, P. 2000, *Earth, Moon, Planets*, **89**, 135
- Kadota, K., Jaeger, M., Galad, A., et al. 2000, *IAU Circ.*, 7534
- Kobayashi, H., Kawakita, H., Mumma, M. J., et al. 2007, *Astrophys. J.*, **668**, L75
- Kutner, M. L., & Ulich, B. L. 1981, *Astrophys. J.*, **250**, 341
- Lamy, P. L., Toth, I., Weaver, H. A., et al. 2000, *Bull. Amer. Astron. Soc.*, **32**, 1061
- Lamy, P. L., Toth, I., Fernández, Y. R., & Weaver, H. A. 2004, The sizes, shapes, albedos, and colors of cometary nuclei, in *Comets II*, ed. M. C. Festou, H. U. Keller & H. A. Weaver (Tucson: Univ. of Arizona press), 223
- Lamy, P. L., Toth, I., Weaver, H. A., et al. 2006, *Astron. Astrophys.*, **458**, 669
- Lamy, P. L., Toth, I., A'Hearn, M. F., Weaver, H. A., & Jorda, L. 2007, *Icarus*, **187**, 132

- Lamy, P. L., Toth, I., Jorda, L., et al. 2008, *Bull. Amer. Astron. Soc.*, **40**, 393
- Larson, H. P., Hu, H-Y, Hsieh, K. C., et al. 1991, *Icarus*, **91**, 251
- Levison, H. F. 1996, *Amer. Soc. Pac. Conf. Ser.*, **107**, 173
- Licandro, J., Tancredi, G., Lindgren, M., Rickman, H., Hutton, R. G. 2000, *Icarus*, **147**, 161
- Lis, D. C., Keene, J., Young, K., et al. 1997, *Icarus*, **130**, 355
- Magee-Sauer, K., Mumma, M. J., DiSanti, M. A., Dello Russo, N., & Rettig, T. W. 1999, *Icarus*, **142**, 498
- Manfroid, J., Hutsemékers, D., Jehin, E., et al. 2007, *Icarus*, **187**, 144
- Michałowski, T. 1988, *Acta Astron.*, **38**, 455
- Milam, S. N., Apponi, A. J., Ziurys, L. M., & Wyckoff, S. 2006, *IAU Circ.*, 8702
- Morris, C. S., Kronk, G. W., Garradd, G., et al. 1995, *IAU Circ.*, 6246
- Müller, H. S. P., Schlöder, F., Stutzki, J., & Winnewisser, G. 2005, *J. Mol. Struct.*, **742**, 215
- Newburn, R. L., & Spinrad, H. 1985, *Astron. J.*, **90**, 2591
- Newburn, R. L., & Spinrad, H. 1984, *Astron. J.*, **89**, 289
- Nolan, M. C., Harmon, J. K., Howell, E. S., et al. 2006, *Bull. Amer. Astron. Soc.*, **38**, 504
- Pety, J. 2009, *IRAM Memo 2009-1*
- Pickett, H. M., Poynter, R. L., Cohen, E. A., et al. 1998, *J. Quant. Spectrosc. & Rad. Transfer*, **60**, 883
- Press, W. H., Flannery, B. P., Teukolsky, S. A., Vetterling, W. T., *Numerical Recipes in C: The Art of Scientific Computing*, Cambridge Univ. Press 1992
- Prialnik, D., Benkhoff, J., & Podolak, M. 2004, Modeling the structure and activity of comet nuclei, in *Comets II*, ed. M. C. Festou, H. U. Keller & H. A. Weaver (Tucson: Univ. of Arizona press), 359
- Rothman, L. S., Jacquemart, D., Barbe, A., et al. 2005, *J. Quant. Spectrosc. & Rad. Transfer*, **96**, 139
- Samarasinha, N. H., A'Hearn, M. F., Hoban, S., & Klinglesmith, D.A. 1986, CN jets of comet P/Halley – rotational properties, in *ESA Proc. of the 20th ESLAB Symp. on the Exploration of Halley's Comet. Vol. 1.* ESA SP-250, 487
- Samarasinha, N. H., Mueller, B. E. A., Belton, M. J. S., & Jorda, L. 2004, Rotation of cometary nuclei, in *Comets II*, ed. M. C. Festou, H. U. Keller & H. A. Weaver (Tucson: Univ. of Arizona press), 281

- Schleicher, D. G. 2006, *Cent. Bureau Elect. Telegram*, 491
- Schleicher, D. G., & Osip, D. 2002, *Icarus*, **159**, 202
- Schleicher, D., & Woodney, L. *IAU Circ.*, 8906
- Schleicher, D. G., Millis, R. L., Osip, D. J., & Birch, P. V. 1991, *Icarus*, **94**, 511
- Schloerb, F. P., Kinzel, W. M., Swade, D. A., & Irvine, W. M. 1986, *Astrophys. J.*, **310**, L55
- Scotti, J. V., Galad, A., Boehnhardt, H., et al. 1996, *IAU Circ.*, 6301
- Sekanina, Z. 2005, *Int. Comet Quaterly*, **27**, 225
- Snodgrass, C., Lowry, S. C., & Fitzsimmons, A. 2006, *MNRAS*, **373**, 1590
- Snodgrass, C., Fitzsimmons, A., Boehnhardt, H., et al. 2007, *Cent. Bureau Elect. Telegram*, 1111
- Stellingwerf, R. F. 1978, *Astrophys. J.*, **224**, 953
- Storm, S., Samarasinha, N., Mueller, B., et al. 2006, *Bull. Amer. Astron. Soc.*, **38**, 504
- Tenishev, V., Combi, M., & Davidsson, B. 2008, *Astrophys. J.*, **685**, 659
- Toth, I., & Lisse, C. M. 2006, *Icarus*, **181**, 162
- Toth, I., Lamy, P., & Weaver, H. A. 2005, *Icarus*, **178**, 235
- Toth, I., Lamy, P., Weaver, H., et al. 2006, *Bull. Amer. Astron. Soc.*, **38**, 489
- Tubiana, C. 2008, *Characterization of physical parameters of the ROSETTA target comet 67P/Churyumov-Gerasimenko*, Ph.D. thesis, Technischen Universität Braunschweig
- Ulich, B. L., & Haas, R. W. 1976, *Astrophys. J. Suppl.*, **30**, 247
- Villanueva, G. L., Bonev, B. P., Mumma, M. J., et al. 2006, *Astrophys. J.*, **650**, L87
- Waniak, W., Borisov, G., Drahus, M., et al. 2009, *Earth, Moon, Planets* (accepted)
- Weaver, H. A., Feldman, P. D., Festou, M., A'Hearn, M. F., & Keller, H. U. 1981, *Icarus*, **47**, 449
- Weaver, H. A. 2006, *Bull. Amer. Astron. Soc.*, **38**, 484
- Wild, W. 1999, *The 30m Manual*, 2nd ed.
- Woodney, L. M., Owen, T. C., & Fernández, Y. R. 2003, *IAU Circ.*, 8239
- Woodney, Laura, Schleicher, D. G., & Bair, A. N. 2008, *Lun. Planet. Inst. Conf.*, **1405**, 8316
- Woodney, Laura, Schleicher, D. G., & Bair, A. N. 2008, *Bull. Amer. Astron. Soc.*, **40**, 415

Yang, B., Jewitt, D., & Bus, S. J. 2009, *Astron. J.*, **137**, 4538

Zakharov, V. V., Bockelée-Morvan, D., Biver, N., et al. 2008, *Lun. Planet. Inst. Conf.*, **1405**, 8144

Publications

Refereed publications

Waniak, W., Borisov, G., **Drahus, M.**, Bonev, T., Czart, K., & Küppers, M. 2009, Rotation of the nucleus, gas kinematics and emission pattern of comet 8P/Tuttle: preliminary results from optical imaging of the CN coma, *Earth, Moon, Planets* (accepted)

Drahus, M., Küppers, M., Jarchow, C., Paganini, L., Hartogh, P., & Villanueva, G. L. 2009, The HCN molecule as a tracer of the nucleus rotation of comet 73P-C/Schwassmann-Wachmann 3, *Astron. Astrophys.* (accepted)

Tubiana, C., Barrera, L., **Drahus, M.**, & Boehnhardt, H. 2008, Comet 67P/Churyumov-Gerasimenko at large heliocentric distance, *Astron. Astrophys.*, **490**, 377-386

Drahus, M., & Waniak, W. 2006, Non-constant rotation period of comet C/2001 K5 (LINEAR), *Icarus*, **185**, 544-557

Mikolajewski, M., Galan, C., Gazeas, K., Niarchos, P., Zola, S., Kurpinska-Winiarska, M., Winiarski, M., Majewska, A., Siwak, M., **Drahus, M.**, Waniak, W., Pigulski, A., Michalska, G., Kolaczowski, Z., Tomov, T., Gromadzki, M., Graczyk, D., Osiwala, J., Majcher, A., Hajduk, M., Cikala, M., Zajczyk, A., Kolev, D., Dimitrov, D., Semkov, E., Bilkina, B., Dapergolas, A., Bellas-Velidis, L., Csak, B., Gere, B., Nemeth, P., & Apostolovska, G. 2005, The preliminary photometric results of the 2003 eclipse of EE Cep, *Astrophys. & Space Sci.*, **296**, 445-449

Non-refereed publications

Drahus, M., Paganini, L., Ziurys, L. M., Peters, W., Jarchow, C., & Hartogh, P. 2008, The recent mega-outburst of comet 17P/Holmes at millimeter wavelengths, *Lun. Planet. Inst. Conf.*, **1405**, 8340

Drahus, M., Jarchow, C., Hartogh, P., Waniak, W., Bonev, T., Borisov, G., Czart, K., and Küppers, M. 2008, Millimeter-wavelength spectroscopy as a tool for studying the rotation of active comets: The case study of comet 8P/Tuttle, *Lun. Planet. Inst. Conf.*, **1405**, 8334

Tubiana, C., Boehnhardt, H., **Drahus, M.**, Barrera, L., Ortiz, J. L., Schwehm, G., Schulz, R., Stuewe, J., & Vincent, J. B. 2008, 67P/Churyumov-Gerasimenko: The Rosetta target comet in the aphelion arc, *Lun. Planet. Inst. Conf.*, **1405**, 8047

Drahus, M., Jarchow, C., Hartogh, P., Waniak, W., Bonev, T., Borisov, G., Czar, K., & Kueppers, M. 2008, Comet 8P/Tuttle, *Cent. Bureau Elect. Telegram*, 1294

Drahus, M., Paganini, L., Ziurys, L., & Peters, W. 2008, Comet 17P/Holmes, *Cent. Bureau Elect. Telegram*, 1289

Drahus, M., Paganini, L., Ziurys, L., Peters, W., Soukup, M., & Begam, M. 2007, Comet 17P/Holmes, *IAU Circ.*, 8891

Drahus, M., Kueppers, M., Jarchow, C., Paganini, L., Hartogh, P., and Villanueva, G. L. 2007, Submillimeter monitoring of the HCN molecule in fragment C of the split Comet 73P/Schwassmann-Wachmann 3, *Bull. Amer. Astron. Soc.*, **39**, 508

Belton, M. J., & **Drahus, M.** 2007, The accelerating spin of 9P/Tempel 1, *Bull. Amer. Astron. Soc.*, **39**, 498

Tubiana, C., **Drahus, M.**, Boehnhardt, H., Barrera, L., Ortiz, J., Schwehm, G., & Schulz, R. 2007, 67P/Churyumov-Gerasimenko: Photometry and spectroscopy of the Rosetta target comet at large heliocentric distance, *Bull. Amer. Astron. Soc.*, **39**, 498

Villanueva, G., Mumma, M. J., Bonev, B. P., **Drahus, M.**, Paganini, L., Kueppers, M., DiSanti, M. A., Magee-Sauer, K., Hartogh, P., Jarchow, C., Milam, S., & Ziurys, L. M. 2006, Submillimeter molecular observations of the split ecliptic comet 73P/Schwassman-Wachmann 3, *Bull. Amer. Astron. Soc.*, **38**, 485

Mikolajewski, M., Zola, S., Kurpinska-Winiarska, M., Galan, C., Gazeas, K., Niarchos, P., Stachowski, G., Winiarski, M., Siwak, M., Drozd, M., Ogloza, W., Majewska, A., Krzesinski, J., **Drahus, M.**, Waniak, W., Pigulski, A., Michalska, G., Kolaczowski, Z., Tomov, T., Graczyk, D., Gromadzki, M., Maciejewski, G., Majcher, A., Kolev, D., Dimitrov, D., Semkov, E., Bilkina, B., Dapergolas, A., Bellas-Velidis, I., Csak, B., Gere, B., Nemeth, P., & Apostolovska, G. 2004, Photometric observations of two very long period eclipsing binaries: AZ Cas and EE Cep, *Amer. Soc. Pac. Conf. Ser.*, **318**, 378-381

Acknowledgements

I would never be in a position for starting Ph.D. studies if not heroic efforts of my mother Cecylia over years. I am thoroughly thankful to her, and dedicate her this work. Over the years I have also experienced a continual support of my grandma Emilia – I am grateful to her for all the miracles.

I would like to thank my MPS supervisor Chris Jarchow, for showing me the bright side of microwave astronomy, and for letting me realize multitudes of my ideas. This made my Ph.D. research a wonderful scientific adventure! I also thank Paul Hartogh, the leader of the microwave group in Lindau, for providing me with everything I needed for carrying out the research. I am grateful to Waław Waniak, my M.Sc. supervisor, for introducing me to comets at a professional level years ago, and for continues enjoyable collaboration.

My research have been largely based on observations realized with the telescopes of the Arizona Radio Observatory (Steward Observatory, University of Arizona). I am grateful for the observing time I received, and I thank the telescope operators for their excellent work.

During these studies several individuals has provided me with valuable support. Let me hence thank Michael Belton, Dominique-Bockelée-Morvan, Yan Fernández, Klaus Jockers, Konrad Kossacki, Michael Küppers, Lucas Paganini, Bill Peters, Sławomira Szutowicz, Vladimir Zakharov, Lucy Ziurys, and others. I am also grateful to my first teachers of astronomy & comets: my aunt Danka, Henryk Brancewicz, Tomasz Ścieżor, Janusz Pleszka, Patryk Mach, and especially Bogdan Wszolek.

I am thoroughly grateful to Dave Jewitt for letting me further explore my scientific interests under his supervision at UCLA.

Living and studying in Lindau was a great fun, which would not be possible without all the IMPRS folks, including the school coordinator Dieter Schmitt; and especially Philippe and Sofiane, who have instantly became my older brothers.

Last but not least, I thank God for all the good people who influenced me at various stages of my life to become the person I am today. Let me recall here John Paul II, and Adam Gacek.

Curriculum Vitae

Persönliche Daten

Name: Michał Mateusz Drahus
Geburtsdatum: 1. Juli 1981
Geburtsort: Kraków, Polen
Eltern: Cecylia Drahus
Andrzej Klimczak
Staatsbürgerschaft: polnisch

Schulausbildung

1988 – 1996 Grundschole *Tadeusz Kościuszko* in Kraków, Polen
1996 – 2000 Gymnasium *August Witkowski* in Kraków, Polen

Studium

2000 – 2005 M. Sc. Astronomie (Honours), *Uniwersytet Jagielloński* in Kraków, Polen
2006 – 2009 Doktorand am *Georg-August-Universität* in Göttingen und *Max-Planck-Institut für Sonnensystemforschung* in Katlenburg-Lindau